國家原子能科技研究院

委託研究計畫研究報告

微電網三相多電源併聯與調頻之研究

Research on Grid-Connection of Multiple Three-Phase Power Sources and Frequency Regulation in Microgrid

計畫編號：112A015

受委託機關(構)：台灣氫能與燃料電池學會

計畫主持人：陳正一

共同主持人：談光雄

研究期程：中華民國 112 年 3 月至 112 年 12 月

研究經費：新臺幣　57　萬元

國原院聯絡人員：呂學玟

報告日期：112 年 12 月 15 日

目　錄

中文摘要

全球的能源危機和環境問題越來越嚴重，因此人們越來越關注分散式發電和微電網技術，這些技術有助於發展再生能源，推動社會邁向低碳化。未來的電力系統需要減少對化石燃料的依賴，並加大再生能源的使用比例。然而，當分散式電源容量增長到一定比例時，它們通過變流器等電力電子設備接入主電網，幾乎沒有慣性，這可能會對主電網的穩定性造成威脅。為了保證微電網的運轉安全和穩定性，需要有效地整合微電網電力控制策略和相關能源調度機制。如果成功實現這樣的整合，將大大提高微電網的運轉安全性和穩定性，並促進再生能源的發展。本計畫主要目標為(1)建立微電網孤島運轉架構模型；(2)開發三相功率調節系統、柴油機、與再生能源等 3 種電源之併聯技術，使再生能源併接點電壓變動率在 5%以內；(3)開發三相功率調節系統主動及被動孤島偵測、及模式切換技術，當柴油機關閉後，三相功率調節系統維持負載電壓變動率在 5%以內；(4)開發微電網孤島運轉模式下，三相功率調節系統之快速偵測電網頻率技術、及調頻演算法，並維持電池 SOC 在一合理範圍。此外，本計畫將依據國家原子能科技研究院提供之微電網系統為基礎，建立相關電網模型，並透過模擬軟體探討儲能系統、柴油機、與再生能源在不同運作模式與情境之調控策略以維護微電網系統之穩定性。

關鍵字：微電網、功率調節系統、電壓變動率、電網頻率偵測、調頻演算法

Abstract

Since the global energy crisis and environmental issues are becoming increasingly severe, the decentralized power generation and microgrid technologies have drawn much attention in recent years. These technologies are helpful for developing renewable energy and promoting society's transition to low-carbon environment. The future power system needs to reduce its reliance on fossil fuels and increase the proportion of renewable energy usage. However, when the capacity of distributed power sources grows to a certain proportion and connected to the main grid through power electronic equipment such as inverters, little inertia characteristics of these devices may lead to a threat to the stability of the main grid. To ensure the safe and stable operation of microgrids, it is necessary to effectively integrate microgrid power control strategies and related energy scheduling mechanisms. If this integration can be achieved successfully, it will greatly improve the operational safety and stability of microgrids and promote the development of renewable energy.

The main objectives of this project are to: (1) establish a microgrid islanding operation framework model; (2) develop parallel-connection control strategy for three-phase power conditioning systems, diesel generators, and renewable energy, to ensure that the voltage fluctuation rate at the connection point of renewable energy is within 5%; (3) develop active and passive islanding detection and mode switching technologies for the three-phase power conditioning system. When the diesel generator is turned off, the three-phase power conditioning system can maintain the load voltage fluctuation rate within 5%; (4) develop fast detection technology of grid frequency and frequency regulation algorithm for the three-phase power conditioning system in microgrid islanding operation mode, and maintain the SOC of battery within a

reasonable range.

In addition, this project would establish relevant grid models based on the microgrid system provided by National Atomic Research Institute and perform the simulation to explore the control strategies of energy storage systems, diesel generators, and renewable energy under different operating modes and scenarios to maintain the stability of the microgrid system.

Keywords: microgrid, power conditioning system, voltage fluctuation rate, grid frequency detection, frequency regulation algorithm

壹、計畫緣起與目的

近年來，微電網技術在全球得到了廣泛的應用和發展，特別是隨著再生能源的逐漸普及和電網智慧化的推進。微電網作為一種小型、獨立運行的電力系統，其發展趨勢受到了多方面的影響，其中包括分散式發電、儲能技術、能源管理系統以及用戶需量反應等方面的技術進展。

分散式發電是微電網的一個重要組成部分，其主要特點是將發電設施分布在電力使用點附近，實現近距離供電。太陽能、風能、小型燃氣發電機等分散式能源成為微電網的主要電源。隨著太陽能和風能技術的不斷進步，分散式發電系統的效率和可靠性逐漸提高。然而，分散式發電也面臨著不穩定的問題，例如太陽能和風能的時變性，這需要配套的儲能技術和智慧控制系統進行協同調節。

儲能技術在微電網中的應用對於平衡能源供需、提高系統穩定性具有關鍵作用。常見的儲能技術包括電池儲能、超級電容儲能等。這些技術可以對不穩定的分散式發電進行調頻輔助服務、平滑功率輸出、提高系統運行效率等。然而，儲能技術的高成本和有限的循環壽命是目前面臨的主要挑戰。新型儲能技術的研發和應用是未來的發展方向，以提高能源儲存效率並降低成本，同時對應儲能設備的特性，相關之控制技術將影響儲能系統所能發揮的效益。

在用戶負載端部分，用戶需量反應是通過智慧計量表分析用電情況、以智慧電器進行能源控制等手段，實現對用戶電力需求的即時監測和調節。在微電網中，用戶需量反應是實現電力平衡的重要手段之一。當電力供應過剩時，系統可以通過調整用戶負載實現能源的消納；反之，當電力不足時，系統可以通過啟動儲能設施或調

節分散式發電進行補充，電源調度不及時，則啟動需量反應進行降/卸載。

而能源管理系統與相關技術則是微電網最為核心的發展重點。能源管理最佳化技術通過對微電網中各個能源組成部分的監測、預測和調度，實現整個系統的最優運行。其中，人工智慧的應用和大數據分析技術的發展對於實現能源管理最佳化提供了強有力的支持。然而，由於微電網中存在多種能源形式和複雜的耦合關係，實現全面的能源管理最佳化仍然是一個具有挑戰性的課題。能源管理技術中的電網基頻偵測技術，是微電網中實現功率平滑化和頻率穩定的重要手段。通過即時監測電網的基頻變化，系統可以實現對功率輸出的精確調節，從而維持電網的穩定性。然而，電網基頻偵測技術需要高精度的儀器和先進的數據處理手段，實現對電網基頻的即時監測和調節，這也是技術研發的一個主要瓶頸。

微電網技術中的功率平滑化、儲能調頻輔助服務、需量反應、能源管理最佳化、電網基頻偵測等技術的發展，是實現微電網高效運行的重要保障。然而，這些技術在應對能源系統複雜性和即時性等方面仍然面臨一系列挑戰。本計畫則針對微電網運轉穩定性，希冀提供一套合適之控制機制，輔助微電網基頻偵測之準確度與反應速度提升、電力供需調節穩定、系統異常時仍能快速調節維持供電。

本計畫主要目標為(1)建立微電網孤島運轉架構模型；(2)開發三相功率調節系統、柴油機、與再生能源等三種電源之併聯技術，使再生能源併接點電壓變動率在 5%以內；(3)開發三相功率調節系統孤島偵測及模式切換技術，當柴油機關閉後，三相功率調節系統維持負載電壓變動率在 5%以內；(4)開發微電網孤島運轉模式下，三

相功率調節系統之快速偵測電網頻率技術、及調頻演算法，並維持電池 SOC 在一合理範圍。此外，本計畫將依據國家原子能科技研究院提供之微電網系統為基礎，建立相關電網模型，並透過模擬軟體探討儲能系統、柴油機、與再生能源在不同運作模式與情境之調控策略以維護微電網系統之穩定性。

在三相功率調節系統、柴油機、與再生能源等三種電源之併聯技術方面，需要考慮各種因素對系統穩定性和可靠性的影響，例如功率平衡、電壓穩定、頻率穩定等。故本計畫透過發展基於電池儲能系統(Battery Energy Storage System, BESS)之三相功率調節系統控制技術，達成微電網併聯輸出功率之平滑化。文獻中常見之平滑化技術主要應用於太陽能輸出，主要方法如下：

(a)低通濾波器(Low Pass Filter, LPF)

低通濾波器的目標是阻止高頻分量，同時允許低頻分量通過。文獻[1]中使用 SOC 回授控制來延長電池的使用壽命。如圖 1 的模型所示，P_{PV} 是未平滑的太陽能輸出功率，而 P_{PO} 是濾波器平滑後的輸出功率。BESS 的充放電功率訊號 P_{ref} 為平滑訊號 P_{PO} 與未平滑訊號 P_{PV} 的差。BESS 的輸出功率由 P_{BESS} 表示。

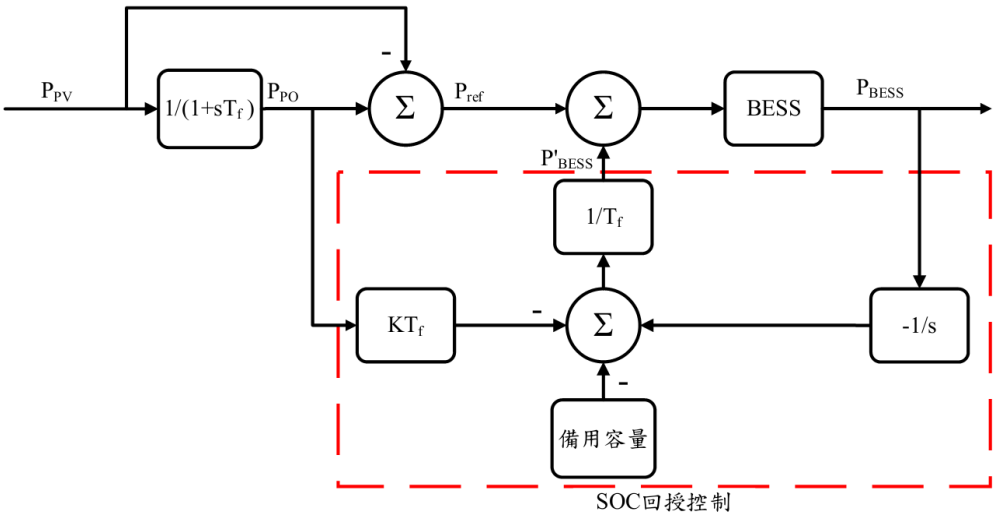

圖 1、具有 SOC 回授控制的平滑方法

(b)移動平均濾波器(Moving Average Filter, MAF)

通過 MAF 計算太陽能輸出功率的平均值，可以消除太陽能輸出功率的波動。MAF 的窗口大小與實際太陽能輸出功率有關，可以通過調整窗口大小的值來改變輸出功率的平坦度以改變太陽能發電的穩定程度。通過 MAF 平滑算法所估計的功率與實際太陽能輸出功率數據的差來決定電池的充電放電狀態，因此可以得到相當平滑的功率輸出。

(c)雙移動平均濾波器(Double Moving Average Filter, DMAF)

文獻[2]中提出並分析了用於太陽能輸出功率平滑的 DMAF。DMAF 通過依次合併兩個 MAF 來組成。每個 MAF 各自包含一個窗口。DMAF 主要透過功率數據的移動平均計算，然後使用第一個移動平均的平均值作為觀察值進行第二個移動平均計算。

(d)移動中值濾波器(Moving Median Filter, MMF) [3]

與前面描述的 MAF 和 DMAF 類似，MMF 也是使用固定長度的窗口進行平滑。然而，MMF 不是計算窗口的平均值，而是計算由窗口大小給定的長度向量的中值。MMF 優於平均算法，因為短期和快速的不穩定性被最小化。當封閉數據中存在額外的異常值時，MMF 非常有效。也就是說，如果指定窗口內的輸出太陽能數據集由許多外圍數據點組成，那麼與 MAF 和 DMAF 相比，MMF 將更有效的處理這些數據。

(e)高斯濾波器(Gaussian Filter, GF)

此種平滑濾波器，其脈衝響應為高斯函數的近似值。文獻[4]中利用 GF 平滑來穩定再生能源發電，能同時最小化上升和下降時間，從而具有最小的延遲，並解決平滑和功率追蹤的不足。GF 使用滑動窗口，但平滑的程度由高斯的標準偏差決定而不是平均算法決定。然而，濾波器有時候會過度平滑太陽能輸出功率數據，導致訊號的特性丟失。

上述濾波器的平滑性能隨著其窗口大小或時間常數的增加而提高，然而這會導致最終平滑功率的時間延遲。減少時間延遲可以降低電池充電、放電的功率，減少電池尺寸提高電池的使用壽命，以及降低對於電力品質的影響避免造成故障。然而低通濾波器的運算

方式是上述方法中最為簡易且容易實現的架構，因此本計畫透過針對低通濾波器的窗口大小或時間常數調整，使其平滑性能達成計畫目標。此外，不同於文獻中應用於太陽能系統輸出功率平滑化，本計畫將應用此概念透過電池儲能系統來平滑化三相功率調節系統、柴油機、與再生能源等三種電源之併聯調度時造成的功率擾動，穩定功率輸出。

微電網的控制模式是確保整個系統能夠有效運作、保持穩定性並優化能源利用的關鍵。以下是微電網控制的主要模式：

(a)中央控制模式(Centralized Control)：

中央控制模式是一種集中管理微電網運作的方式。在這種模式下，存在一個中央控制器或管理系統，負責監測、調度和協調微電網中各個元件，包括分散式發電、儲能系統、負載等。中央控制模式能夠提供整體性的系統優化，但可能面臨單點故障風險。

(b)分散式控制模式(Distributed Control)：

分散式控制模式將決策權下放到微電網中的各個元件，使得每個元件能夠自主做出運作決策。這種模式下，各個分散式發電設施、儲能系統和負載能夠根據局部信息和需求進行調節，提高系統的彈性和韌性。

(c)協同控制模式(Cooperative Control)：

協同控制模式結合了中央控制和分散式控制的優勢。在這種模式下，微電網中的各個元件可以根據中央控制的指導進行協作。這種方式既考慮了整體系統的最佳化，又保留了各元件的自治性。

(d)需求反應控制模式(Demand Response Control)：

需求反應控制模式依賴於負載端的主動參與。通過與用戶的通信，微電網可以根據需求反應的信號，調整發電和儲能系統的運作，以滿足用戶的實際需求。

(e)市場化控制模式(Market-Based Control)：

市場化控制模式引入市場機制，使得微電網中的各元件能夠參與市場交易。透過價格信號，各元件可以根據市場需求調整其運作，以實現經濟效益和資源優化。

每種控制模式都有其優勢和局限性，實際應用中的微電網控制通常會採用不同模式的組合，以達到最佳效果。系統操作者和工程師需要綜合考慮微電網的規模、結構、用途以及當地條件等因素，以選擇合適的控制策略。本計畫所探討之系統因規模不大，且主要調控重點在儲能系統，因此本計畫採用分散式控制模式來進行微電網之併網及孤島運轉切換。

頻率是電力系統穩定性、效率和安全性的重要運行指標。保持電力系統的頻率盡可能接近其額定值是必要的。在許多電力系統的保護和控制中，需要準確測量和偵測電力系統的基頻。在文獻[5]中指出頻率偵測應滿足三個目標。首先，為了及時發現基頻，偵測方法應具有計算效率。其次，保持估算方法的準確性。第三，由於在估算過程中存在許多干擾，偵測方法應該具有強健性，對雜訊具有免疫力。因此本計畫透過改良時域分析方法，以符合上述之開發重點。

貳、研究方法與過程

微電網的運轉模式通常可以分為三種情境：首先是與傳統集中式電網互相連接運轉，此時微電網的主要任務是為傳統電網提供支援，以應對大規模的能源波動和尖峰負載。在這種情境下，微電網可以通過調整自身的負載和電力輸出，為傳統電網提供穩定的電力供應。其次是在孤島模式下運轉的情境，此時微電網是獨立運行的，不與傳統電網互相連接。在這種情境下，微電網需要保證自身的穩定運行，並提供可靠的電力供應給區域內的用戶。為了實現這一目標，微電網需要整合多種電力資源，如太陽能、風能、儲能等，以及採用先進的控制技術和調度策略，實現對能源的高效利用。最後是在多微電網互聯模式下運轉，此時微電網中的各個電力資源和負載都可以互相通訊和交流，形成一個高度智慧化和自主調節的電力系統。在這種情境下，微電網可以實現能源的自由流動和共享，提高電力系統的可靠性和穩定性。此外，多微電網互聯模式還可以實現更多元精確的能源管理和促進綠色能源發展，有望成為未來電力系統的重要發展方向[6]-[8]。本計畫依據國家原子能科技研究院提供之微電網系統之資訊，主要操作與併網與孤島模式，以下則針對此兩種模式進行相關控制技術之說明。

一、建立微電網孤島運轉架構模型

微電網系統建模是設計、分析、優化及控制微電網運作的核心。這項工作的架構直接影響到微電網的可靠性、穩定性和效率。以下說明微電網系統建模的重要性以及建模的重點要素。

建模重要性：

1. 系統分析與設計： 微電網涉及多種元件，包括分散式能源資源、儲能系統、負載和控制系統等。透過建模，可以將複雜的系統分解成更容易理解和設計的部分，有助於系統的全面分析和設計。
2. 效能評估： 建模提供了評估微電網性能的手段。透過模擬不同操作條件和負載情境，可以預測系統的韌性、穩定性以及能源利用效率，從而指導系統的改進和優化。
3. 控制策略制定： 系統建模為制定有效的控制策略提供基礎。通過對系統動態響應的模擬，可以評估各種控制策略的效果，以實現最佳的能源管理和穩定性控制。
4. 問題排查： 在實際運行中，微電網可能會面臨各種問題，例如電壓不穩、頻率波動等。建模可以幫助識別潛在的問題源，有助於迅速解決和改進系統運作。
5. 未來擴建規劃： 建模也提供了規劃微電網未來擴建和升級的工具。通過對系統進行模擬，可以預測未來的需求和挑戰，以確保系統的擴展符合未來需求。

建模的重點要素：

1. 元件特性： 微電網中的各種元件，如太陽能電池、風力發電機、儲能系統等，需要準確的數學模型，包括其性能曲線、效率和動態響應。
2. 能源流動： 正確建模能源在微電網中的流動是至關重要的。這包括電力、熱能和儲能系統的充放電過程。
3. 負載特性： 各種負載對電網的影響不同，因此建模需考慮負載的特性，如動態變化、功率需求曲線等。

4. 控制系統： 穩定控制是微電網操作的一個關鍵方面。建模應考慮各種控制系統，例如頻率和電壓控制器。
5. 通信網路： 若微電網中有通信網路用於系統監控和控制，則需將通信的延遲、可靠性等因素納入建模。
6. 環境條件： 天氣和環境條件直接影響可再生能源的產生，因此建模需考慮氣象條件和季節變化。

綜上所述，微電網系統建模是實現穩定、高效運行的基礎。透過對系統各方面的準確描述，建模不僅提供了對當前系統狀態的理解，還有助於制定未來的發展策略和應對各種挑戰。本計畫主要著重在控制策略的開發，因此通信網路與環境條件之因素並無於模型中考慮。本計畫依據國家原子能科技研究院所提供之系統資訊，建立微電網孤島運轉架構模型，該系統之單線圖如圖 2 所示。此部分之工作內容可以分為以下幾個部分來執行：(a)系統資訊收集與分析-首先，透過國家原子能科技研究院所提供的系統資訊，例如柴油機和再生能源的技術規格、電網結構和相關設備等。接著，透過分析系統資訊，了解微電網孤島運轉模式下的電力供應情況、可能發生的問題及其原因，以及現有控制策略的不足之處。(b)協調柴油機與再生能源之控制策略開發-為了解決柴油機頻繁升降載和電網頻率波動的問題，需要開發具協調柴油機與再生能源之控制策略。透過該策略，可以讓柴油機和再生能源之間實現協同運行，平穩地調節電網的頻率和電壓。(c)微電網三相功率調節系統調頻策略開發-微電網孤島運轉模式下，需要開發微電網三相功率調節系統調頻策略，以實現電力平衡和頻率穩定。透過該策略，可以根據電網的實際情況，調節柴油機和再生能源的輸出功率，達到電力供需平衡和頻率

穩定的目的。(d)建立微電網孤島運轉架構模型-在完成上述工作後，可以根據系統資訊、控制策略和調節策略，建立微電網孤島運轉架構模型。該模型可以模擬微電網孤島運轉模式下的電力供應情況和控制策略效果，進行系統性能評估和優化設計，以實現微電網系統的高效、穩定和可靠運行。為達成上述目標，本計畫透過 Simulink 開發環境，建立圖 2 之微電網集總模型，如圖 3 所示。

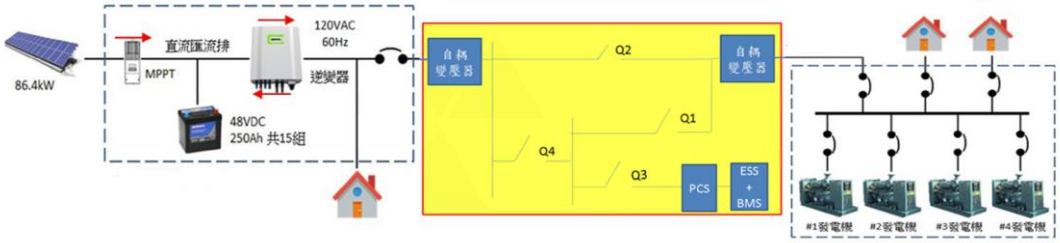

圖 2、微電網孤島運轉架構

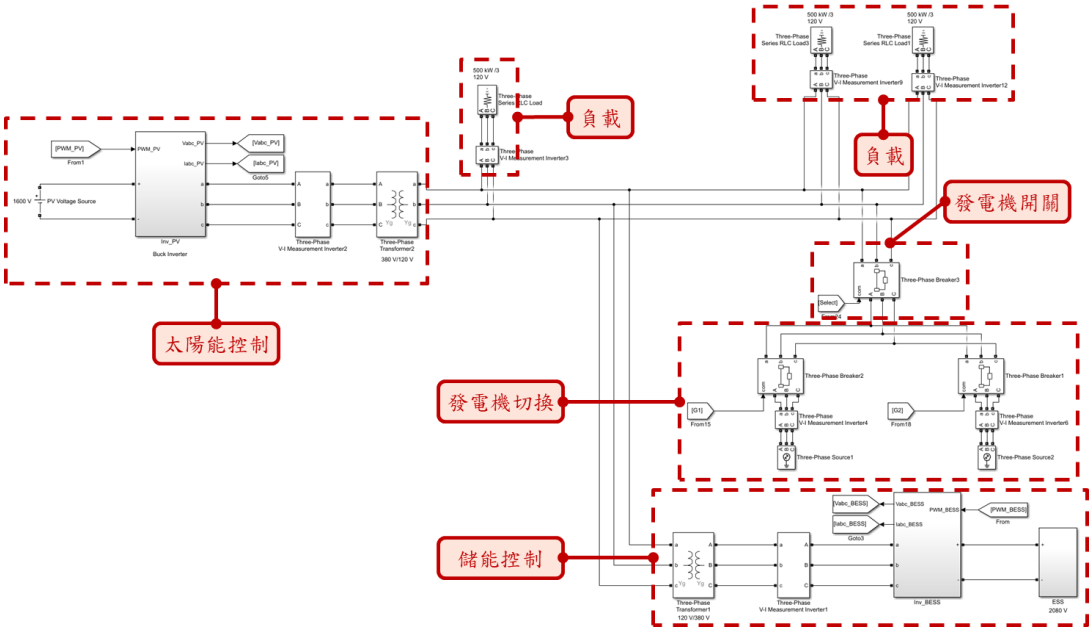

圖 3、Simulink 開發環境中之微電網模型

二、開發三相功率調節系統、柴油機、與再生能源等三種電源之併聯技術

在微電網系統中，柴油發電機、太陽能系統和電池儲能系統的

併聯運轉控制技術是實現穩定、高效能源供應的關鍵。其中，電池儲能系統在併聯運轉中扮演著關鍵的角色。儲能控制需要根據能源供應情況和系統負載進行自主調整。這包括對電池的充放電控制，以及確保儲能系統在需要時能夠有效地釋放儲存的能量。良好的控制算法可以提高儲能系統的效能，延長電池的壽命。

依據以儲能系統為主的微電網架構，系統主要包含兩種運轉模式。微電網可以在與主電網脫離的情況下運行，這種運行模式被稱為孤島模式。與此相對，併網模式則表示微電網重新與主電網連接。在這兩種模式下，微電網的功率變動會對系統產生不同的影響。

孤島模式下的功率變動影響

1. 獨立穩定運行：在孤島模式下，微電網必須自主維持穩定運行，因此對於負載的變動需求要有靈活的應對機制。當負載增加時，需要確保能夠提供足夠的發電量；反之，當負載減少時，需要調整發電量以避免能源浪費。
2. 儲能系統的重要性：孤島模式下，儲能系統扮演著關鍵的角色。它可以平滑處理可再生能源的波動，並在需要時提供額外的功率或吸收多餘的發電量。這有助於保持微電網的穩定性。
3. 頻率和電壓控制：由於與主電網脫離，孤島模式下，微電網需要自主控制頻率和電壓。功率變動可能導致頻率和電壓的波動，需要能有效地進行調節。

併網模式下的功率變動影響

1. 同步性和穩定性：併網模式下，微電網需要與主電網同步，確保頻率和相位一致。功率的快速變動可能導致不穩定，因此需要進行複雜的控制以確保平穩併網。
2. 頻率和電壓匹配：與孤島模式不同，併網模式下，微電網的頻率和電壓需要與主電網協同。功率變動可能引起這兩者的波動，需要進行細緻的調控。
3. 平滑併網過程：併網時，微電網需要平滑地接入主電網，避免因突然連接而引起的頻率和電壓震盪。這需要先進的控制策略和同步機制。
4. 通信和協同控制：併網需要微電網與主電網之間的即時通信，以實現協同控制。功率變動的快速調節需要有效的通信系統。

總的來說，孤島模式下的功率變動主要影響微電網的自主運行和穩定性，而併網模式下的功率變動則需要更複雜的控制策略，以確保微電網與主電網的協同運行。有效的能源管理和先進的控制技術是實現這兩種模式下功率變動影響最小化的關鍵。

根據第壹章之介紹，本計畫針對以儲能系統為基礎之微電網控制主要透過分散式控制方式進行，其中尤以主從控制法為主流機制。主從控制法中，主機單元的三相功率調節系統採用雙迴路控制架構，外部迴路控制器控制電壓幅值與頻率，而內部迴路控制器則控制電感電流且需具有較快的動態特性。如圖 4 所示，當主機單元的三相功率調節系統與市電併聯運轉時，採用定功率控制法(PQ Control)，使外部迴路維持輸出的實、虛功率，若是在孤島運轉時，採用電壓頻率控制法(VF Control)，用來產生固定的電壓與頻率。

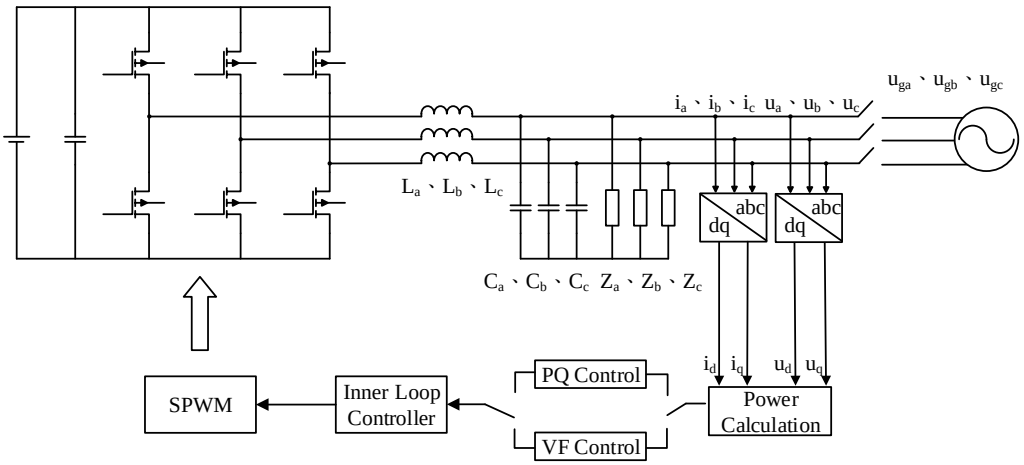

圖 4、主從控制法切換示意圖[9]

依據主從控制架構，三相功率調節系統與柴油發電機、太陽能系統併聯運轉時，主要將跟隨柴油發電機電壓與頻率，因此三相功率調節系統主要操作於併網控制模式，即定功率控制模式(PQ control)。故依據能量守恆定理，三相功率調節系統之儲能電池所提供之功率 P_{BESS} 則為

$$P_{BESS} = P_L - P_G - P_{PV} \quad (1)$$

其中，P_L 為負載消耗功率、P_G 為柴油發電機輸出功率、P_{PV} 為太陽能系統輸出功率。

柴油發電機因價格便宜，在某些情況下，微電網可能依賴柴油發電機作為主要或備用電源。儘管柴油發電機在一些環境下是有效的，但也存在一些缺點，這些缺點需要在微電網設計和管理中考慮。以下是柴油發電機在微電網中的缺點：

1. 環境影響與可持續性

柴油發電機的使用通常伴隨著環境影響和可持續性問題。柴油燃料的燃燒會釋放二氧化碳(CO_2)、氮氧化物(NOx)和顆粒物等大氣

污染物，這對於氣候變化和空氣品質形成威脅。由於全球對於可持續發展的需求增加，使用柴油發電機的微電網可能需要轉向更清潔、可再生的能源選擇。

2. 能源價格波動

柴油價格的波動對於柴油發電機的運行成本產生直接影響。因為柴油價格容易受到國際原油價格的波動影響，這使得微電網的運營者難以預測和穩定發電成本。這對於微電網的經濟可行性和長期運營形成挑戰。

3. 噪音和振動

柴油發電機運轉時會產生噪音和振動，這對周圍環境和社區可能構成困擾。在一些需要安靜環境的區域，如住宅區或學校附近的微電網，柴油發電機的噪音和振動可能會引起居民的反感，並有可能違反當地的環境法規。

4. 燃料供應風險

柴油發電機的運行依賴於燃料的供應，而這可能受到供應鏈中斷、運輸問題或燃料價格波動等多種風險的影響。如果燃料供應中斷，微電網可能無法正常運行，導致能源缺乏和停電問題。

5. 維護和管理成本

柴油發電機需要定期的維護和管理，包括燃料系統的清潔、機油更換、風扇皮帶檢查等。這些維護活動增加了微電網的運行成本，特別是在偏遠區域或人力資源匱乏的地區，維護變得更加困難。

根據以上說明，往往微電網場域中會裝設多台柴油發電機，以因應故障維修、運轉過熱停機等問題，因此以柴油發電機為主要電源的偏鄉微電網系統則會遭遇柴油發電機間之切換供電，故在三相功率調節系統與柴油發電機、太陽能系統併聯運轉時，亟需良好的功率輸出平滑化機制來維持負載端之供電穩定度。依據(1)式之觀察，當柴油發電機輸出功率 P_G 因設備切換發生擾動ΔP_G 時，需要由三相功率調節系統的儲能電池額外提供ΔP_{BESS} 來消弭擾動，使負載之功率維持穩定，如(2)式所示。

$$P_{BESS} + \Delta P_{BESS} = P_L - (P_G + \Delta P_G) - P_{PV} \qquad (2)$$

由(2)式可知，原本操作在定功率控制模式下之三相功率調節系統從輸出 P_{BESS} 功率，需額外調整輸出ΔP_{BESS} 的功率，該數值由原始負載功率經一設計良好之低通濾波器，可獲得平滑控制後之穩定負載功率當作參考訊號，經原始負載功率扣除該參考訊號後即可獲得調整輸出ΔP_{BESS} 的功率值，進而傳送命令控制儲能系統達成，其控制架構如圖 5 所示。

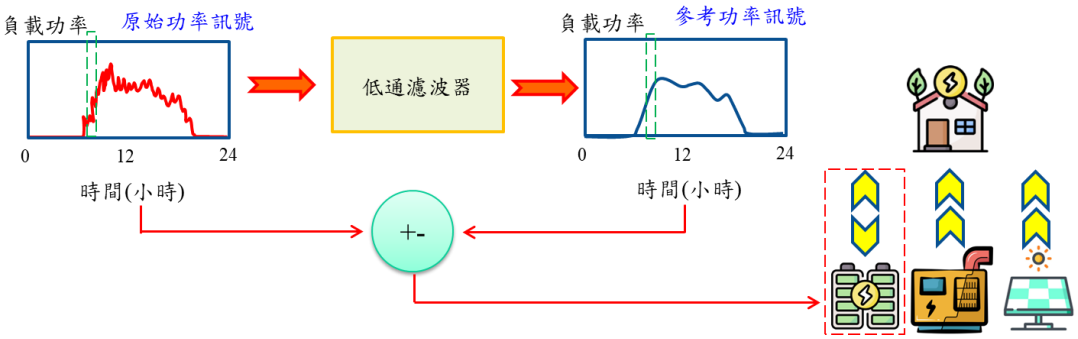

圖 5、負載功率平滑化控制架構

為了驗證本計畫所設計之負載功率平滑化控制來協調三相功率調節系統、柴油機、與再生能源等三種電源之併聯，以下規劃一個

情境進行模擬測試，如圖 6 所示。

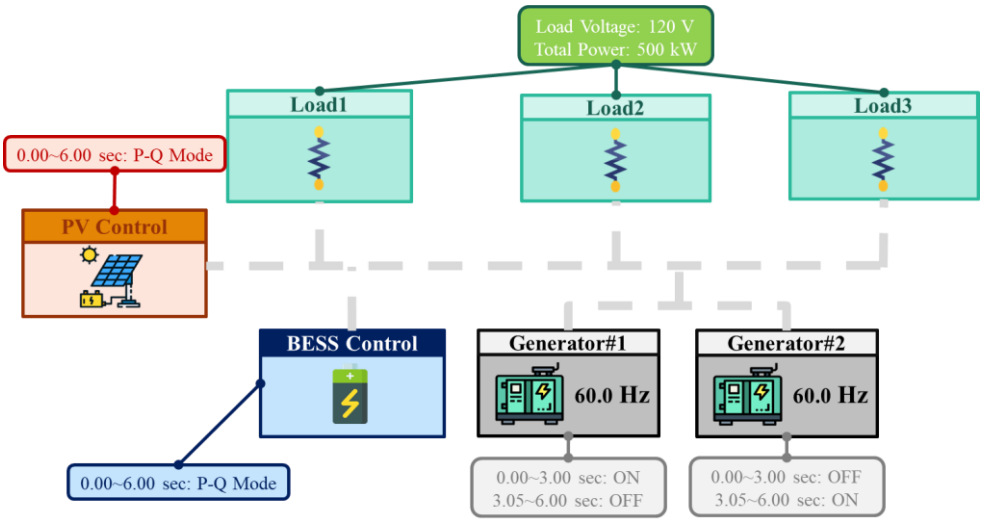

圖 6、柴油發電機擾動對負載影響之模擬情境

在本案例中太陽能系統穩定輸出 250 kW，負載需求 500 kW，因微電網系統有柴油發電機組提供穩定電壓與頻率參考值，故儲能系統運轉在定功率控制模式，穩定輸出 200 kW。在第 3 秒時第 1 台柴油發電機(輸出 50 kW)異常停止並切換至第 2 台柴油發電機持續供電 50 kW。負載之消耗功率與儲能系統輸出功率分別如圖 7 與 8 所示。

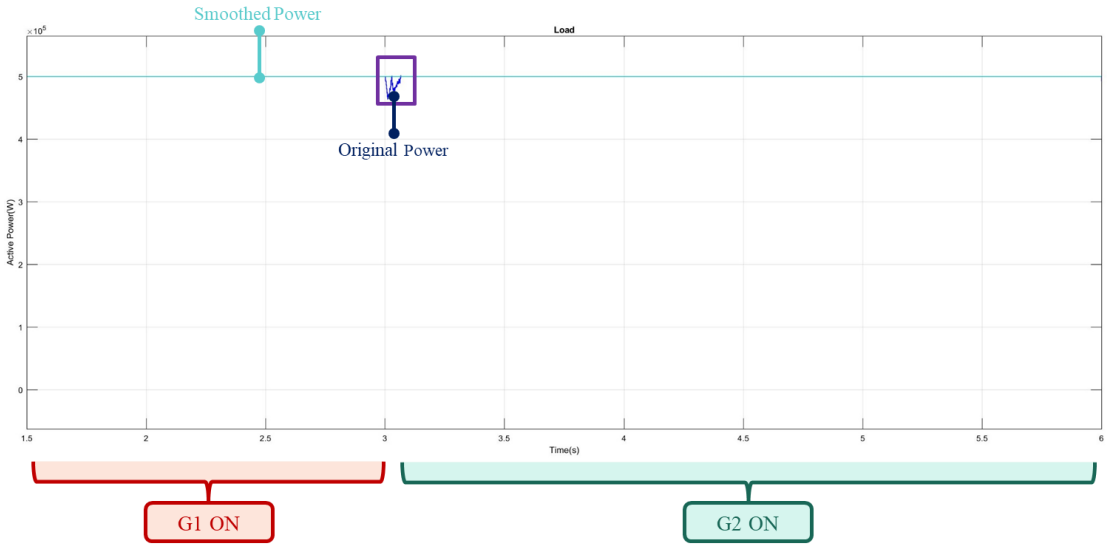

圖 7、負載之消耗功率

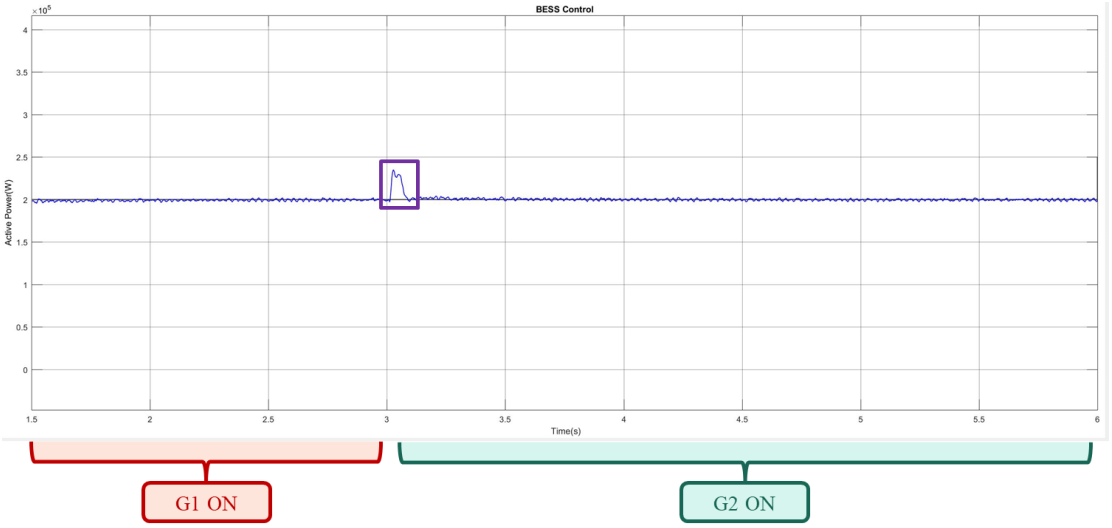

圖 8、儲能系統輸出功率

由圖 7 負載之消耗功率結果可以發現，若儲能系統僅以傳統定功率控制模式固定輸出 200 kW(如圖 8)，則在兩台柴油發電機切換時會有瞬間電源短缺情況，因此負載之消耗功率會突然間下降，此現象容易造成負載端降/卸載，甚至造成負載設備損壞。若儲能系統導入平滑化控制機制，在原本的定功率輸出準位上依據(2)式進行 ΔP_{BESS} 之擾動功率補償，則負載之消耗功率可以維持原本的 500 kW，沒有負載跳脫。而對應圖 8 儲能系統之輸出功率可以發現，在兩台柴油發電機切換時儲能系統額外提供輸出功率，協助穩定負載用電。如同本報告所提，功率平滑化機制需要一設計良好之低通濾波器，否則容易造成最終平滑功率的時間延遲。圖 7 之穩定平滑輸出結果，有賴於選用低通濾器之時間常數低於兩台柴油發電機切換時間即可達成。關於併接點之電壓部分，三相電壓近視結果如圖 9 所示，由結果可以發現其電壓變動率<5%以內，控制結果十分穩定。

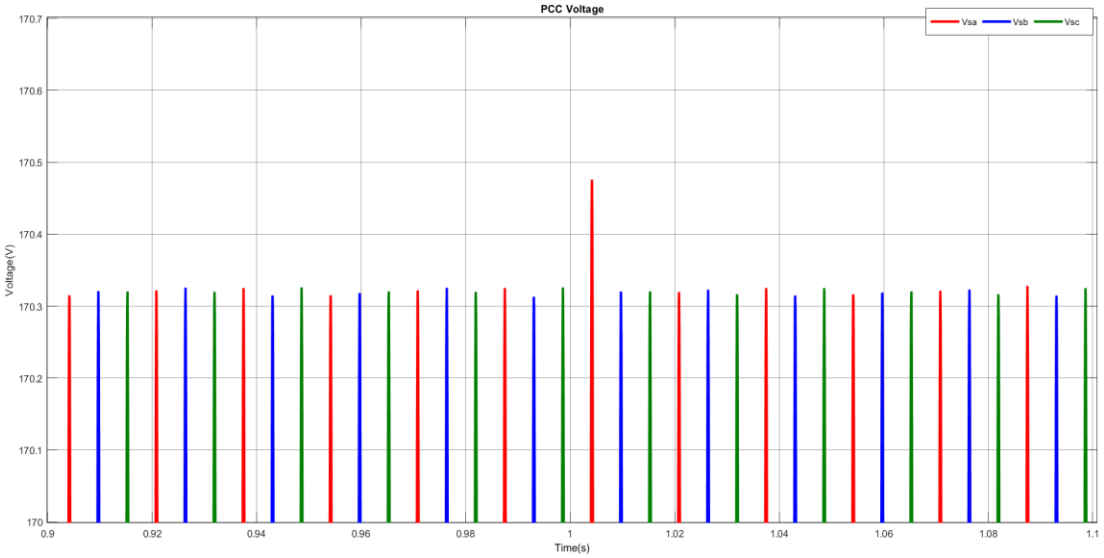

圖 9、併接點三相電壓近視結果

三、開發柴油機關閉時三相功率調節系統孤島偵測及模式切換技術

微電網之主從控制依據主參考電源存在與否可分為兩種控制模式，如下之詳細說明：

孤島控制模式

當微電網操作在孤島模式時，因為失去電網電壓做為參考訊號，會造成微電網的電壓與頻率不穩定。因此為了維持微電網輸出的電壓及頻率，採取電壓頻率控制法(VF control)，如圖 10 所示，將三相功率調節器輸出之三相電壓 V_{ia}、V_{ib}、V_{ic} 經由帕克轉換(Park's Transformation)得到 V_d、V_q 兩個分量，其中 θ 為一 60 Hz 之相位，以這兩個分量與目標參考電壓 V_{dref} 與 V_{qref} 比較後透過電壓控制器進行調整。將三相電感電流 I_a、I_b、I_c 經由帕克轉換得到 I_d、I_q 兩個分量，再與電壓控制器輸出的目標參考電流 I_{dref}、I_{qref} 比較後透過電流

控制器加上前饋訊號 V_d、V_q 作為電壓控制訊號，最後經由反帕克轉換轉回三相電壓控制訊號後產生弦式脈波寬度調變訊號(Sinusoidal Pulse-Width Modulation, SPWM)以控制三相功率調節器。其中電壓與電流控制器使用比例積分(Proportional Integral, PI)控制機制。

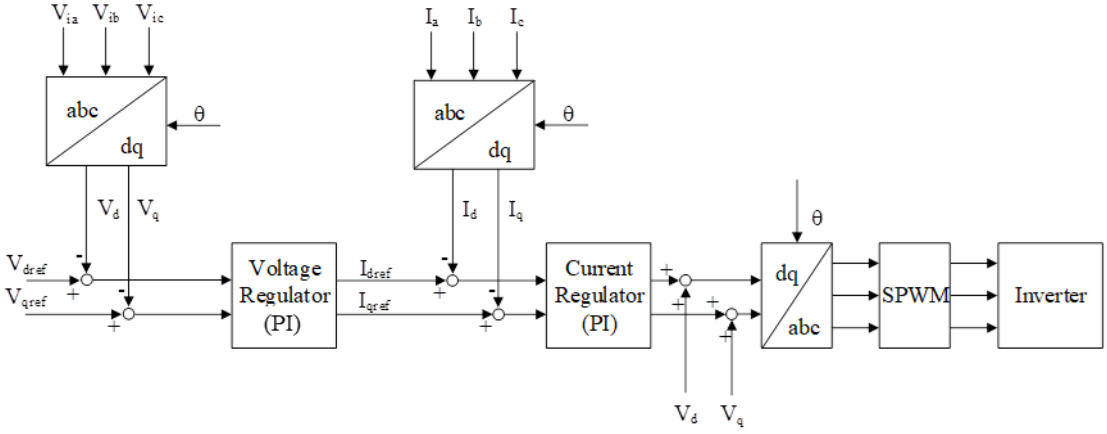

圖 10、孤島控制模式架構圖

併網控制模式

當微電網操作在併網模式時，採取定功率控制法(PQ control)，此控制法是藉由適當的控制電流將實、虛功穩在一個定值，架構圖如圖 11 所示，首先將微電網端輸出三相電流 I_a、I_b、I_c 經由帕克轉換得到 I_d、I_q 兩個分量，以這兩個分量與目標參考電流 I_{dref} 與 I_{qref} 比較後透過電流控制器進行調整。併網運轉時，微電網輸出電壓與市電同步，因此測量共同耦合點上之三相電壓 V_{ia}、V_{ib}、V_{ic}，並透過同步參考框鎖相迴路得到電網相位 θ_g 與電壓幅值等資訊。將電流控制器所得到的值加上前饋訊號 V_d、V_q，最後經由反帕克轉換轉回三相電壓控制訊號後產生弦式脈波寬度調變訊號以控制三相功率調節器。其中電壓與電流控制器使用比例積分控制機制。

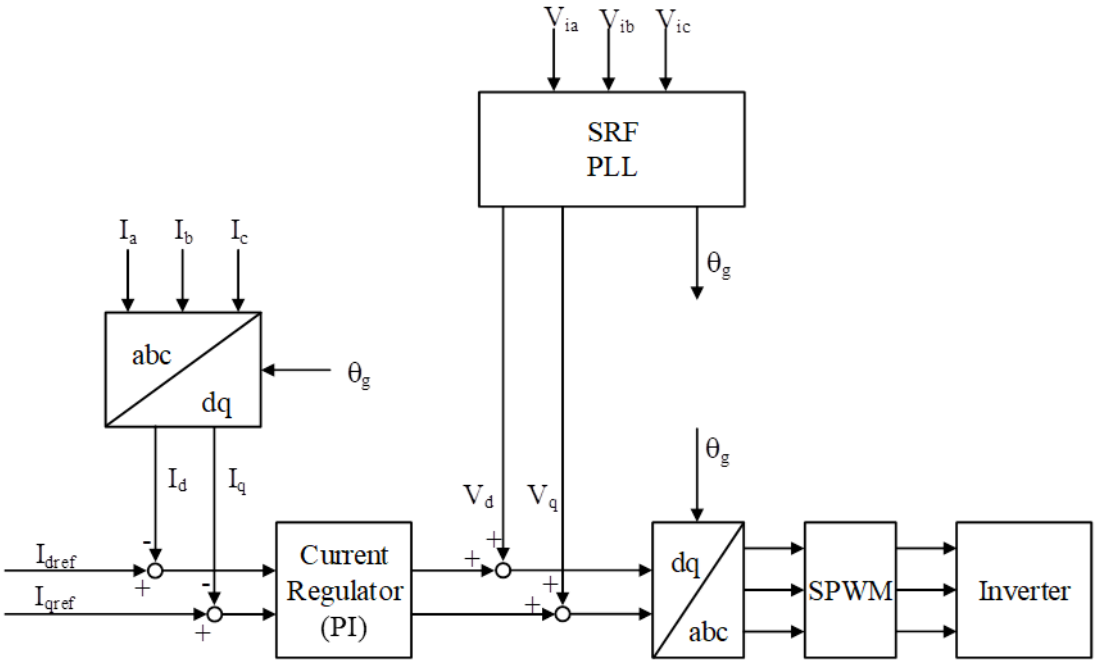

圖 11、併網控制模式架構圖

然而在併網轉換到孤島模式時，發電系統需依據併聯技術要點，於規定時間內跳脫分散式系統之斷路器，保護分散式系統及維持其供電穩定度。本計畫採用 IEEE Std. 1547 及台灣電力股份有限公司系統併聯技術要點，採用 2 秒作為跳脫規定時間[10], [11]。微電網之孤島偵測又可依據技術類型分為被動式孤島偵測法與主動式孤島偵測法。

被動式孤島偵測法

被動式孤島偵測方法與主動式偵測不同，它不主動向電網注入任何信號或改變操作參數來偵測孤島狀態。相反，被動式偵測依賴於監測電網的自然電氣參數，如電壓、頻率、相位等，以判斷孤島的存在。這種方法的優勢在於對微電網的干擾較小，且一般來說成

本較低。以下為常見的被動式孤島偵測方法：

1. **電壓變化偵測**：當微電網與主電網分離時，會影響到負載與發電平衡，進而導致電壓變化。通過監測電壓的波動或超出預定範圍的變化，可以偵測到孤島情況[12]。
2. **頻率變化偵測**：孤島形成後，微電網內的頻率可能會由於負載變化而偏離正常範圍。通過持續監控頻率，可以識別出非正常的頻率波動，這可能是孤島的跡象[13]。
3. **相位變化偵測**：微電網與主電網分離後，可能會出現相位不匹配的情況。監測相位的變化可以提供孤島存在的證據。
4. **諧波分析**：在孤島操作中，微電網中的諧波含量可能會發生變化。通過分析諧波的變化，可以間接判斷孤島的形成。
5. **功率不平衡偵測**：孤島情況下，微電網內的供需平衡可能會被打破。通過監控功率流的變化，可以判斷是否存在孤島情況。

主動式孤島偵測法

在主動式偵測中，偵測裝置或系統會對電網施加某種外部干擾，例如注入諧波、改變頻率或電壓等，然後監測電網的響應。如果電網的響應符合孤島形成時的特定模式，則判斷微電網已經形成孤島。以下為常見的主動式孤島偵測方法：

1. **諧波注入法**：通過向電網注入特定的諧波信號，然後監測這些諧

波的變化。在孤島狀態下，由於缺乏主電網的阻尼作用，這些諧波的行為會有明顯的不同。

2. **滑動模式頻率偏移法**：故意改變微電網的頻率，並觀察這種變化是否會被主電網抵消。如果微電網與主電網分離，頻率變化將不會被抵消，從而表明孤島的存在。
3. **負載撓度法**：透過改變微電網內的負載，觀察電網對這些變化的反應。在孤島狀態下，電網對負載變化的反應會有所不同。
4. **相位跳躍檢測法**：進行短暫的相位變化，然後監控電網的反應。如果微電網與主電網分離，電網的相位反應將顯示出不同的特性。
5. **電壓不平衡注入法**：人為造成微電網內部的電壓不平衡，並觀察這種不平衡如何影響整個系統。在孤島狀態下，這種影響會有顯著的不同。

主動式孤島偵測方法由於能夠更直接、更快速地識別孤島情況，因此在某些應用場景中非常有用。然而，這些方法由於對電網注入擾動量，不合適的擾動量可能會對電網造成一定程度的電力品質問題，並可能對電網的正常運行造成影響。此外，主動式偵測的成本通常高於被動式偵測。為了快速達到孤島檢測且減少對電網之電力品質干擾，本計畫採用被動式孤島偵測方式，透過同時偵測三相功率調節系統與柴油發電機間之共同耦合點電壓與頻率[12], [13]，來判

斷微電網是否進入孤島運轉狀態，其流程如圖 12 所示。

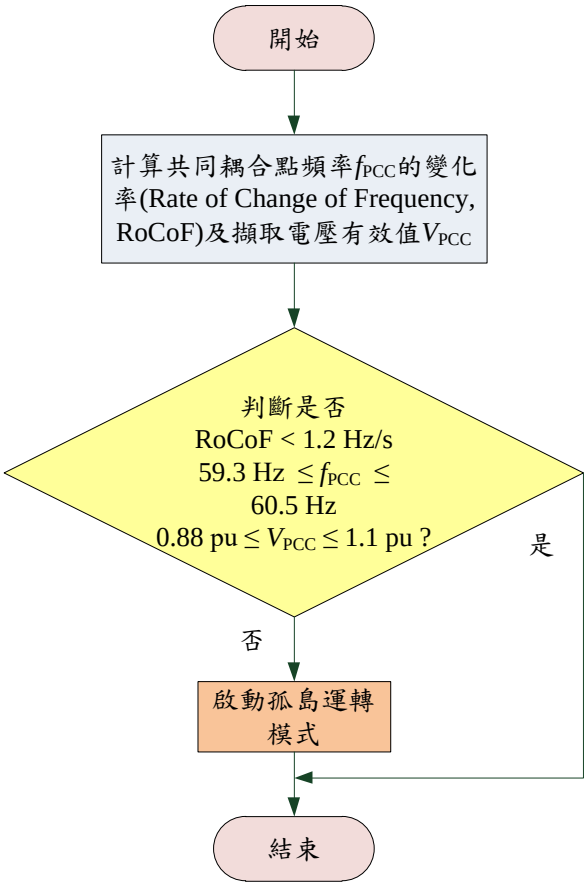

圖 12、本計畫所採用的孤島偵測流程

為了驗證柴油發電機關閉時，三相功率調節系統由併網運轉模式切換至孤島運轉模式之性能，本計畫在圖 6 之運轉情境下，於第 6 秒時關閉柴油發電機，如圖 13 所示。太陽能系統輸出實虛功、儲能輸出實虛功、柴油發電機輸出實虛功及負載消耗實虛功之模擬結果分別如圖 14-17 所示。

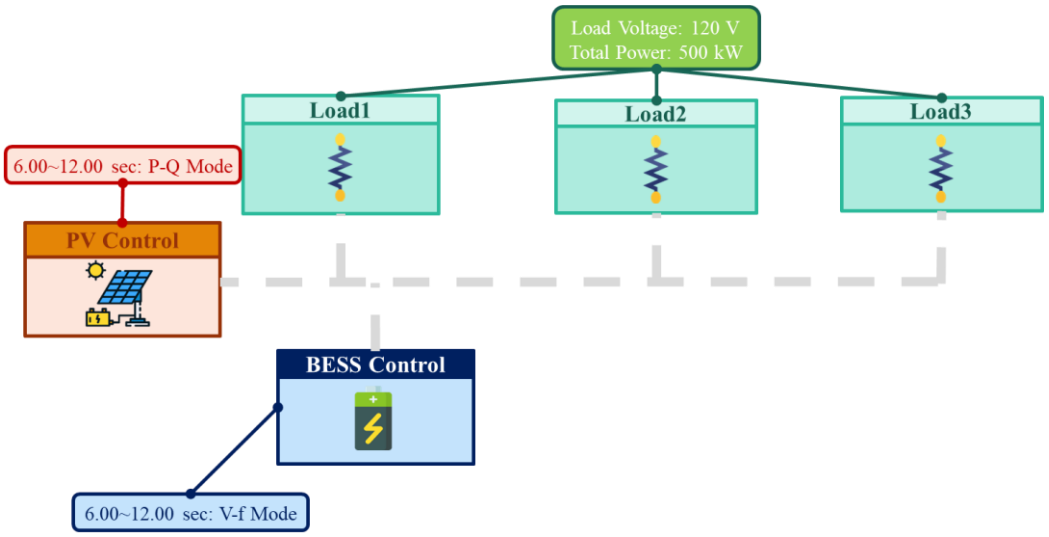

圖 13、柴油發電機關閉對微電網影響之模擬情境

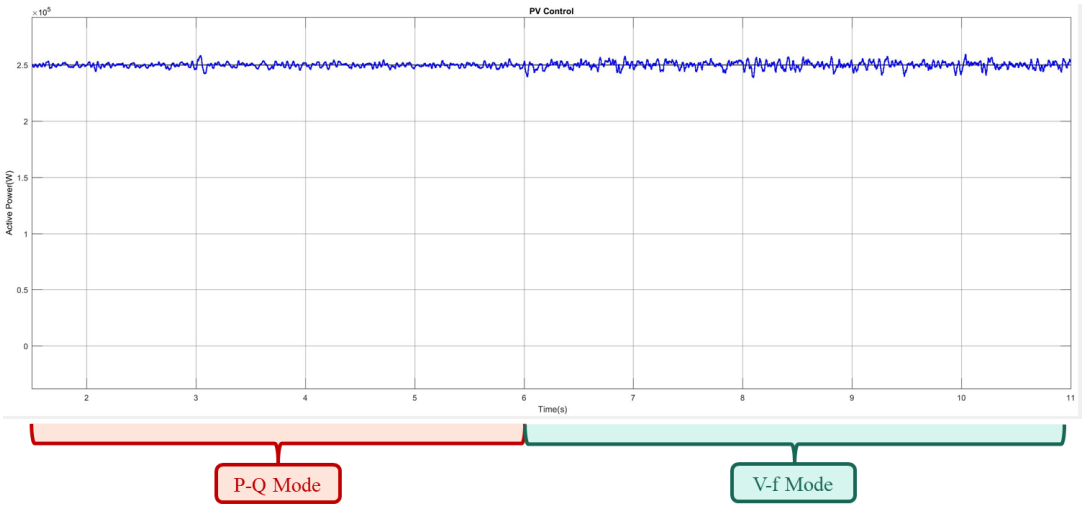

(a)

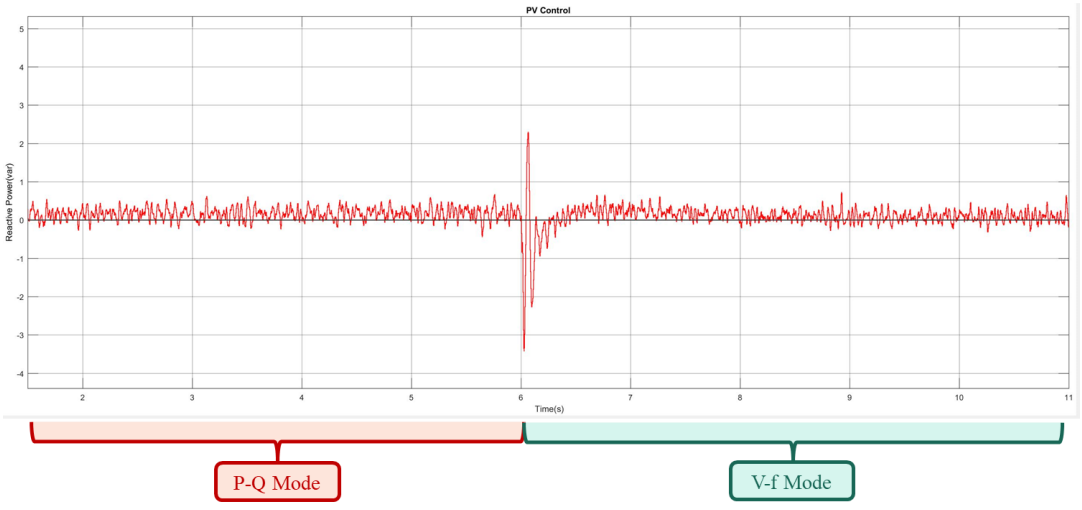

(b)

圖 14、太陽能系統輸出(a)實功 250 kW 與(b)虛功 0 Var

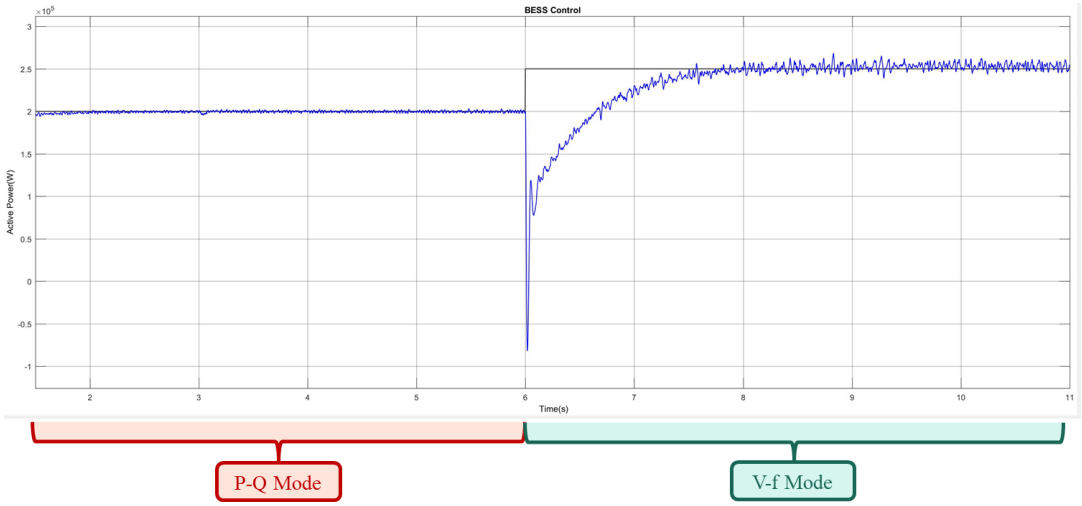

(a)

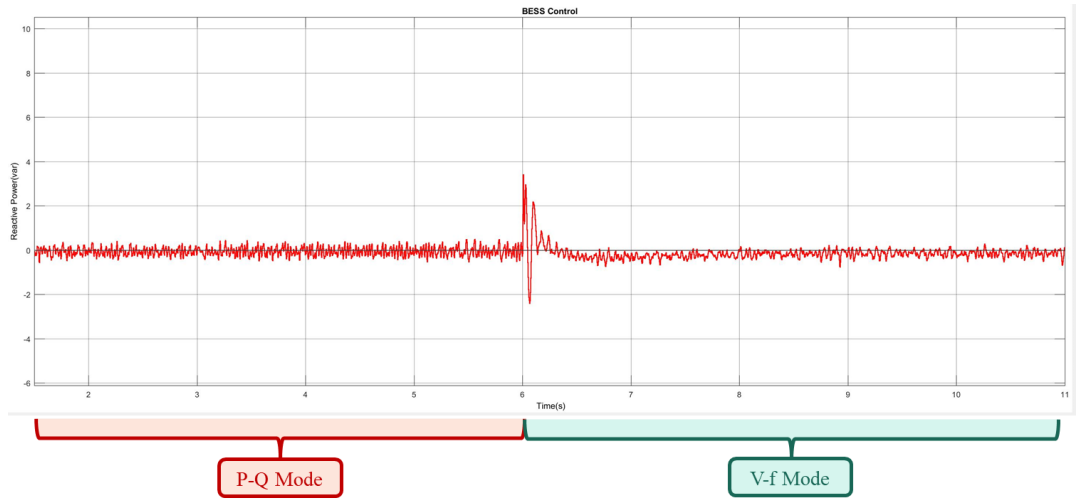

(b)

圖 15、儲能輸出(a)實功從 200 kW 增加至 250 kW 與(b)虛功 0 Var

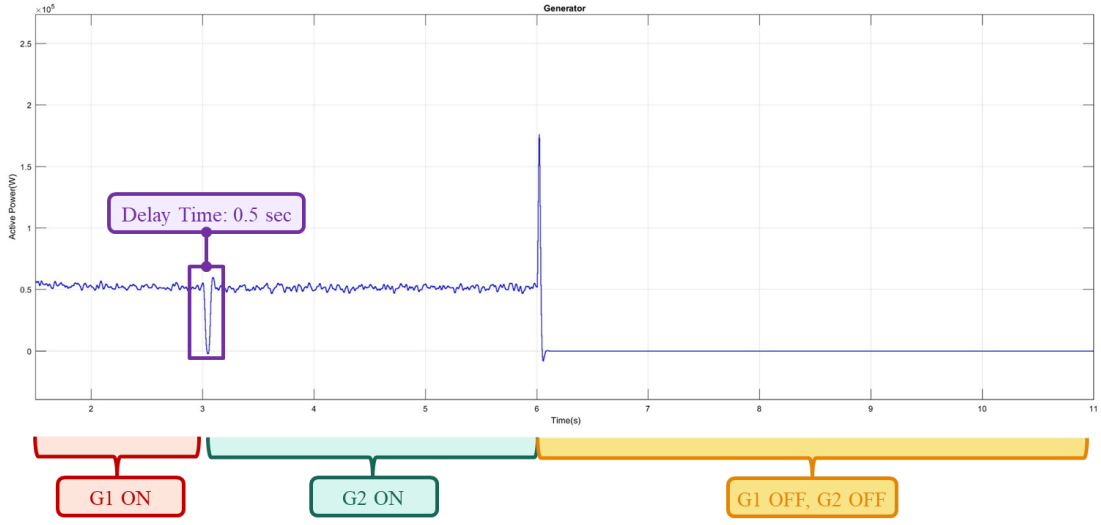

(a)

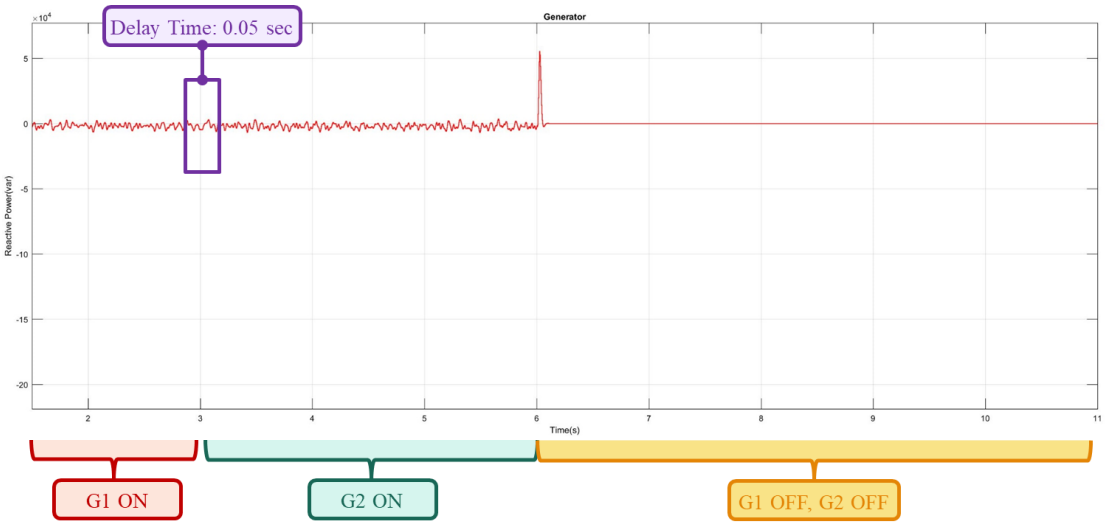

(b)

圖 16、柴油發電機輸出(a)實功從 50 kW 下降至 0 kW 與(b)虛功 0 Var

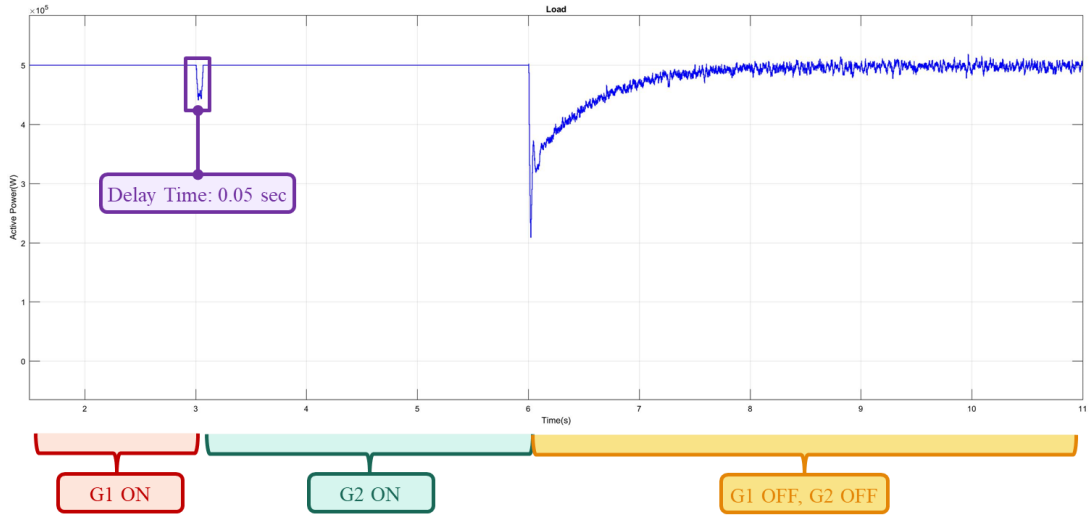

(a)

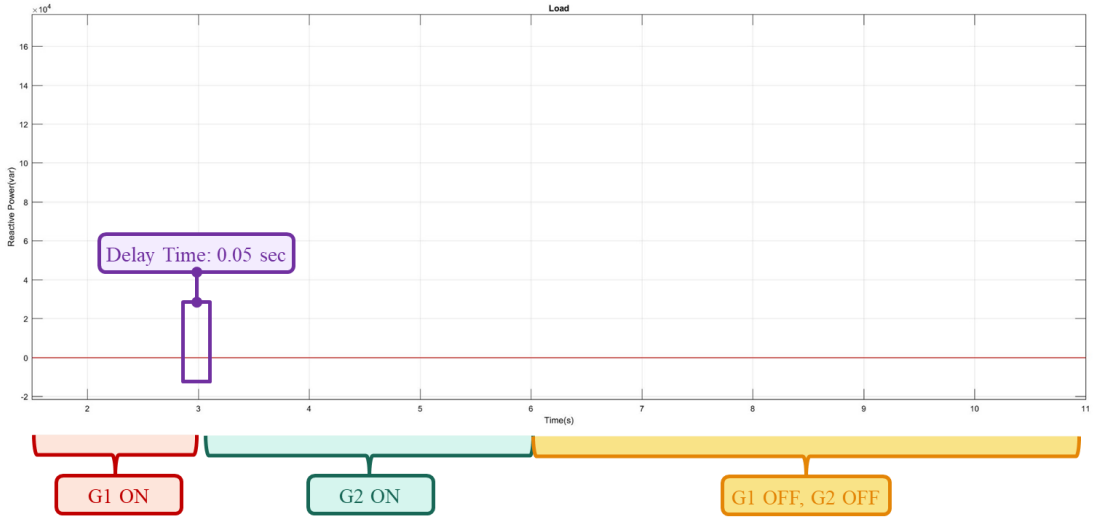

(b)

圖 17、負載消耗(a)實功從 500 kW 與(b)虛功 0 Var

由圖 17 負載之消耗功率結果與圖 15 儲能系統輸出結果可以發現，若儲能系統僅操作於傳統定功率控制模式固定輸出 200 kW，沒有負載功率平滑化控制機制，於兩台柴油發電機切換時，負載將瞬間缺乏電源供應，造成部分降/卸載情形。而在第 6 秒柴油發電機完全關閉後，儲能系統因偵測到主電源發生異常，便將微電網操作於孤島模式以電壓頻率控制機制運作，故撐起微電網之電壓與頻率以 250 kW 輸出，於 1.5 秒左右後維持負載之需求。關於孤島時負載之電壓部分，三相電壓近視結果如圖 18 所示，由結果可以發現其電壓變動率<5%以內，控制結果十分穩定。

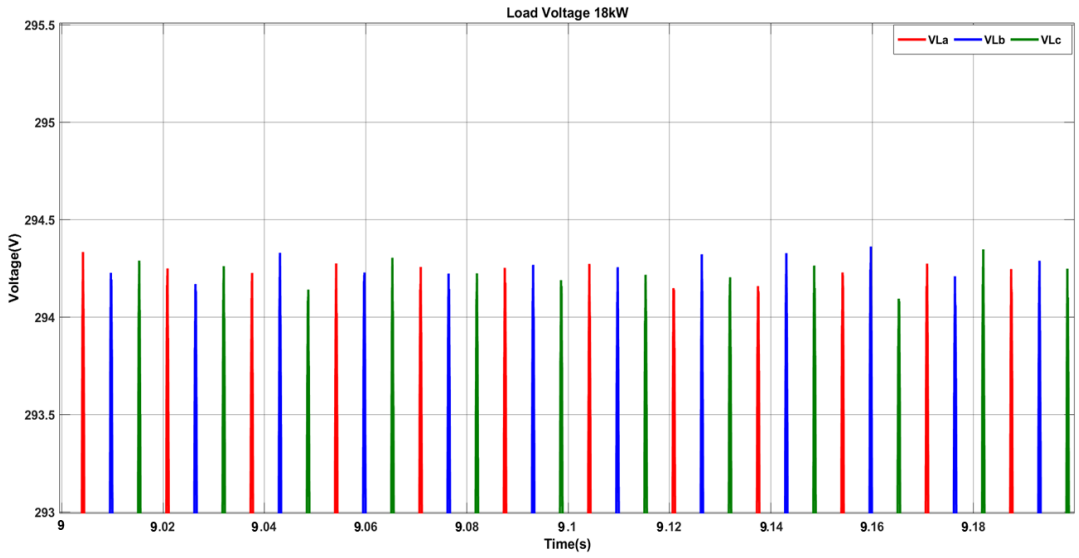

圖 18、孤島時負載三相電壓近視結果

四、開發三相功率調節系統之快速偵測電網頻率技術及調頻演算法

電網頻率偵測是微電網技術中的一個重要環節，用於確定電網

中的基頻成分。為了達成電網頻率快速偵測之目標，本計畫採用時域分析技術普羅尼法(Prony's method)來進行。普羅尼法是一種用於估計指數或正弦項的數學方法，最初用於信號處理和數學物理學領域。在基頻偵測中，普羅尼法被應用於解析複雜信號中的基頻成分，這對於分析電網中的電力波形和波動具有關鍵意義。其應用流程如下：

1. 數據蒐集與前處理(Data Preprocessing)

普羅尼法的應用通常始於數據的蒐集。首先，需要獲取電網中的電力信號數據，這可以通過感測器或測量設備實現。然後，對數據進行前處理，包括去趨勢化、去雜訊等，以確保數據品質。

2. 信號分解(Signal Decomposition)

在獲得合適的數據後，下一步是對信號進行分解。這涉及到將複雜的電力信號分解為不同的成分，其中包括基頻成分。這可以通過使用濾波器等方法實現，獲得較無干擾的基頻信號。

3. 模型擬合(Model Approximation)

一旦信號分解完成，接下來使用普羅尼法進行模型擬合。普羅尼法的核心思想是通過擬合指數或正弦函數，近似描述原信號。在這一步驟中，普羅尼法將信號表示為一系列指數或正弦項的線性組合，從而達到擬合原信號的目的。

4. 頻率提取(Frequency Extraction)

擬合完成後，通過分析擬合模型中的參數，特別是頻率項，可

以提取出信號中的基頻信息。這使得普羅尼法成為一種有效的基頻偵測工具。

採用普羅尼法偵測基頻需考量一些細節。在應用普羅尼法時，參數的選擇至關重要。這包括適當的信號分解方法、擬合模型的選擇以及相應的參數調整。不同的應用場景可能需要不同的參數配置。此外，在基頻偵測中，普羅尼法的應用需要在精度和即時性之間取得平衡。增加擬合模型的複雜度可以提高擬合的精度，但同時會增加計算成本。因此，在實際應用中，需要權衡這兩方面的因素。隨著即時監測的需求增加，未來的研究應試圖優化普羅尼法的計算效率，以應對更為複雜的實際應用場景。而普羅尼法對雜訊敏感，當信號中存在較大的雜訊時，可能影響基頻偵測的準確性。未來的發展方向之一即是提高對雜訊的強健性。為符合上述之重要細節，本計畫在普羅尼法演算架構中，首先利用一濾波器方程式得到訊號基波成分，然後再以複數型式表示，如(3)與(4)式所示，其中 M 為計算所需的取樣點數，A 為基波振幅，ω 為系統角頻率，ϕ 為基波相角[14]。

$$y_m = A\cos\left(m\omega\omega\Delta + \varphi\right)\text{，}m\text{=1、2、…、}M \tag{3}$$

$$y_m = b\,z_1^m + b^*\,z_1^{*m} \tag{4}$$

其中，$b = \frac{A}{2}e^{j\varphi}$，$z_1 = e^{j\omega\Delta t}$。使用普羅尼法的關鍵即是藉由找出適當的線性方程式，讓總誤差之平方和 E 能達到最小值：

$$F(z) = a_0\left(z - z_1\right)\left(z - z_1^*\right) = \sum_{k=0}^{2} z^{2-k}\,a_k \tag{5}$$

$$E=\sum_{m=p}^{M\text{-}1}(\varepsilon_m)^2 \Rightarrow \varepsilon_m=\sum_{k=0}^{p}a_k\delta(k+m\text{-}1) \tag{6}$$

其中 g 代表真實訊號，p 代表指數函數數目。參數 a_k 和信號頻率有關，為我們所要求解之未知數。(4)式共有兩個未知指數函數，令 p=2，定義多項式 $F(z)$為

$$F(z)=a_0(z\text{-}z_1)(z\text{-}z_1^*)=\sum_{k=0}^{2}z^{2\text{-}k}a_k \tag{7}$$

其中，z_1 及 z_1^* 為多項式的根，故根據(4)式，我們將可得到(8)式：

$$\sum_{k=0}^{2}a_k y(k+m\text{-}1)=a_0\,y(m\text{-}1)+a_1\,y_m+a_2\,y(m+1)=0 \tag{8}$$

再根據(5)、(6)以及(8)式整理可得：

$$\varepsilon_m=\sum_{k=0}^{2}a_k[g(k+m\text{-}1)\text{-}y(k+m\text{-}1)]=a_0\,g(m\text{-}1)+a_1\,g_m+a_2\,g(m+1) \tag{9}$$

一般應用上，$a_0=a_2$ ，a_1=1，故(9)式可改寫成：

$$\varepsilon_m=g_m+a_0[g(m\text{-}1)+g(m+1)] \tag{10}$$

為了將以 a_0 有關之誤差 E 之最小化，則令：

$$\frac{\partial E}{\partial a_0}=\sum_{m=2}^{M\text{-}1}2\{g_m+a_0[g(m\text{-}1)+g(m+1)]\}[g(m\text{-}1)+g(m+1)]=0 \tag{11}$$

重新整理(11)式後求得 a_0 為

$$a_0 = -\frac{\sum_{m=2}^{M\text{-}1} g_m\left[g(m\text{-}1)+g(m+1)\right]}{\sum_{m=2}^{M\text{-}1}\left[g(m\text{-}1)+g(m+1)\right]^2} \tag{12}$$

將多項式(7)式改寫成(13)式，則(13)式的根如(14)式所示。

$$z^2+\frac{1}{a_0}z+1=0 \tag{13}$$

$$z_{1,2}=-\frac{1}{2a_0}\pm j\sqrt{1-\frac{1}{4a_0^2}} \tag{14}$$

對照(4)、(14)及(15)式之實部根並將(12)式代入(14)式後，可由(15)式求出角頻率 ω 。

$$z_{1,2}=e^{\pm j\omega\Delta t}=\cos(\omega\Delta t)\pm j\sin(\omega\Delta t) \tag{15}$$

$$\omega=\frac{1}{\Delta t}\cos^{\text{-}1}\left\{\frac{\sum_{m=2}^{M\text{-}1}\left[g(m\text{-}1)+g(m+1)\right]^2}{2\sum_{m=2}^{M\text{-}1} g_m\left[g(m\text{-}1)+g(m+1)\right]}\right\} \tag{16}$$

最後根據(17)式，將 ω 轉換成實際頻率 f 即可得知所估測的頻率大小：

$$f=\frac{\omega}{2\pi} \tag{17}$$

三相功率調節系統若要進行電網調頻功能，則必定操作於併網定功率控制模式。為了驗證本研究所開發之頻率偵測技術之性能，

本研究依據台灣電力公司之調頻備轉輔助服務 dReg 0.25 進行儲能自動頻率控制(Automatic Frequency Control, AFC)[15]，其控制調度曲線如圖 19 所示。

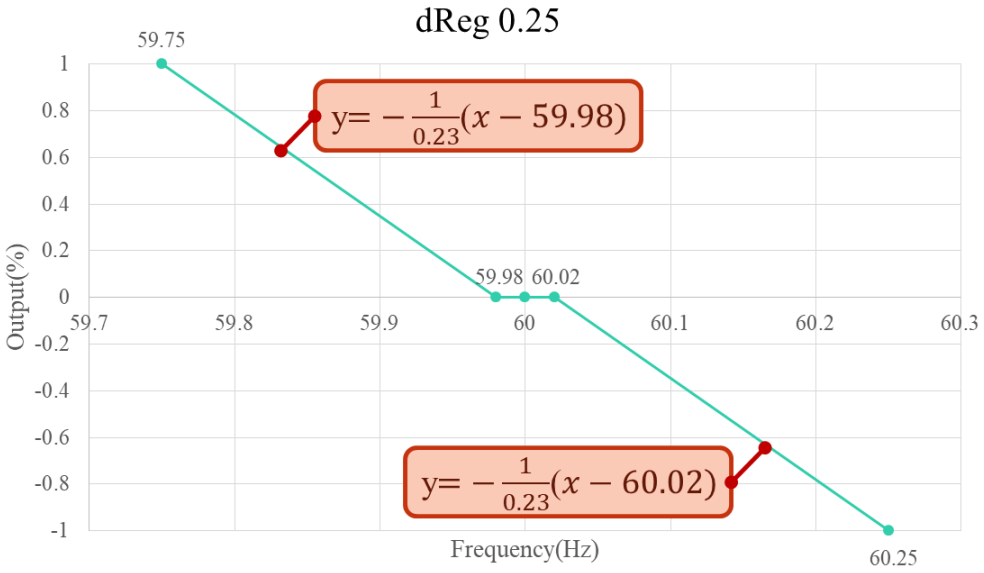

圖 19、dReg 0.25 調頻備轉輔助服務控制調度曲線

為了驗證系統頻率變動時，三相功率調節系統進行 dReg 0.25 調頻備轉輔助服務控制之性能，本模擬情境在第 3.5 秒時系統頻率由 60 Hz 變動至 59.8 Hz、於第 6 秒回復 60 Hz、於第 8.5 秒由 60 Hz 變動至 60.2 Hz，架構如圖 20 所示。本案例 Simulink 開發環境中之微電網模型如圖 21 所示。以普羅尼法偵測系統頻率及儲能系統 dReg 0.25 調頻備轉輔助服務控制之模擬結果分別如圖 22 與 23 所示。

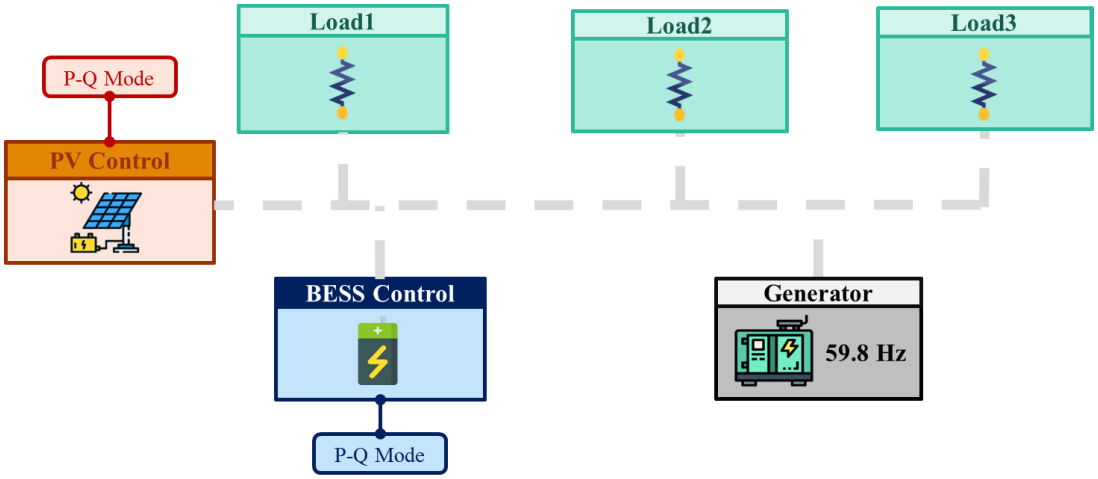

圖 20、系統頻率變動對微電網影響之模擬情境

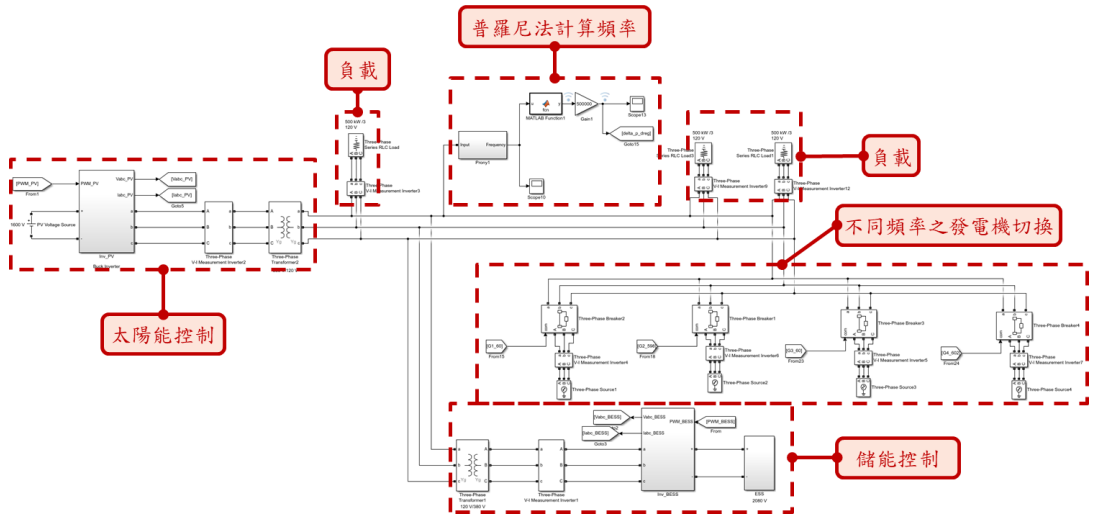

圖 21、Simulink 開發環境中之微電網模型以測試調頻功能

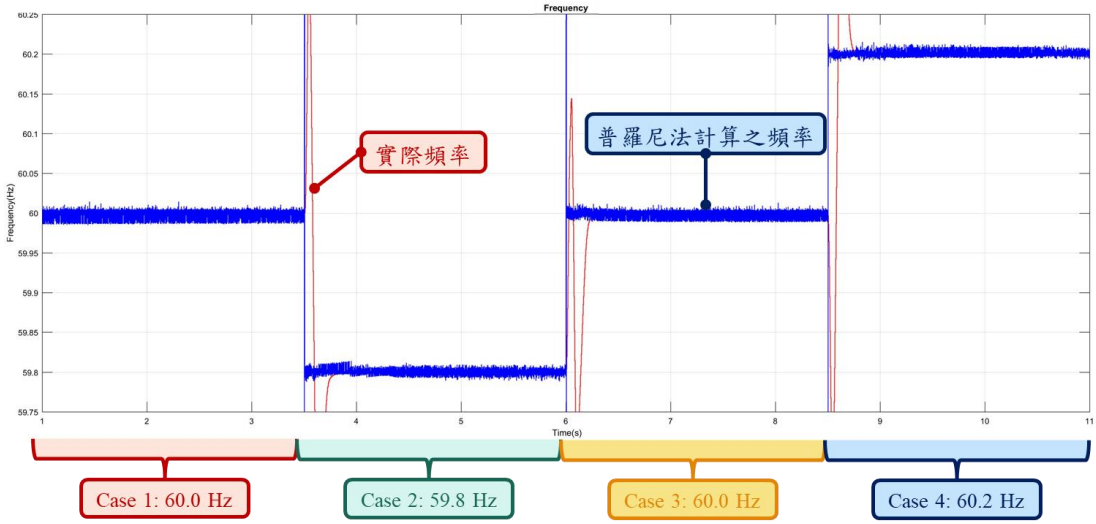

圖 22、以普羅尼法偵測系統頻率之結果

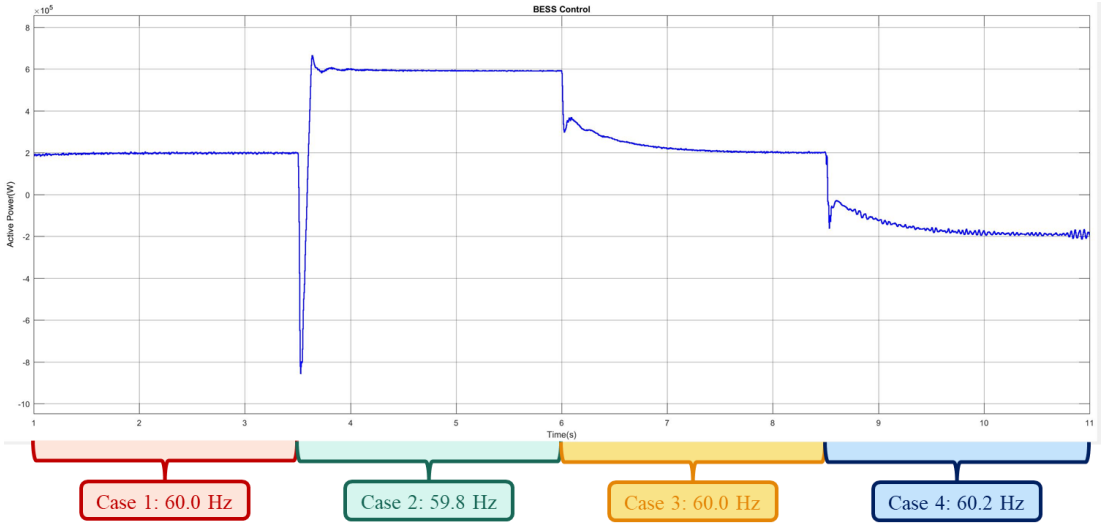

圖 23、儲能系統調頻輔助服務控制結果

由圖 22 系統頻率偵測結果與圖 23 儲能系統調頻輔助服務控制結果可以發現，普羅尼法可以有效完成系統頻率偵測，在此基礎上儲能系統的功率控制則依據圖 19 之調度曲線進行系統頻率調節。在 Case 1 期間，由於系統頻率為 60 Hz，因此儲能系統輸出固定 200 kW 供應負載需求；在 Case 2 期間，系統頻率降至 59.8 Hz，儲能系統則輸出 600 kW 進行調頻；在 Case 3 期間，系統頻率回復至 60 Hz，儲能系統則逐漸減少輸出至原本之 200 kW；最後在 Case 4 期間，系統頻率上升至 60.2 Hz，儲能系統則進行 200 kW 之充電來調頻。由於儲能系統原本已固定輸出 200 kW，因此在此基礎上再根據 dReg 0.25 要求進行調頻備轉輔助服務，因此此情境則為電能移轉複合動態調節備轉服務 E-dReg。

參、主要發現與結論

微電網系統的核心之一是對多種電源的整合與管理，特別是在偏遠地區，柴油發電機作為主要電源，在確保穩定供電方面扮演著關鍵角色。為了應對設備故障、運轉過熱停機等問題，微電網場域中常會裝設多台柴油發電機。在這種情況下，當一台發電機出現故障或需要維修時，系統會自動切換到另一台發電機，以確保供電不中斷。這種切換過程中，為了減少對負載端供電穩定度的影響，需要一個良好的功率輸出平滑化機制。本報告透過三相功率調節系統的儲能電池額外提供功率來消弭因設備切換所產生的擾動，從而維持負載端的功率穩定。

而為了驗證功率平滑化控制的效果，本報告進行了一系列的模擬測試。這些測試模擬了太陽能系統、柴油發電機組以及儲能系統之間的交互作用，特別是在發電機之間的切換過程中。模擬結果顯示，當儲能系統採用功率平滑化控制，即使在發電機切換過程中，負載的消耗功率也能保持在一個穩定的水平，從而避免了負載跳脫或設備損壞的風險。

本研究還特別強調了在微電網運行於孤島模式時的控制策略。孤島模式是指微電網因某些原因與主電網分離，獨立運行的狀態。在這種情況下，由於失去了電網電壓作為參考信號，微電網的電壓和頻率可能會變得不穩定。因此，維持微電網輸出的電壓及頻率成為了一個重要的課題。本報告中介紹了常見的孤島偵測方法，包括被動式和主動式兩種方式。被動式偵測方法依賴於監測電網的自然電氣參數，如電壓、頻率、相位等，而主動式偵測則是通過對電網施加外部干擾並監測其響應來識別孤島情況。

除此之外，本報告還重點介紹了三相功率調節系統的頻率偵測技術，特別是普羅尼法的應用。普羅尼法是一種用於估計指數或正弦項的數學方法，最初用於信號處理和數學物理學領域。在微電網技術中，普羅尼法被應用於解析複雜信號中的基頻成分，這對於分析電網中的電力成分和擾動具有關鍵意義。由本報告中的模擬結果顯示，普羅尼法可以有效完成系統頻率偵測，並使儲能系統依據需求進行電網調頻功能。

綜上所述，本報告的研究成果對於微電網系統的可靠性和效率有著重要的意義。特別是在偏遠地區或緊急情況下，這些技術和策略可以有效地確保電力供應的穩定性和安全性。未來的發展方向應著重於進一步提高這些系統的自適應能力和對環境變化的靈敏度，從而更好地應對複雜和多變的運轉條件。

目前研究成果，已投稿國際期刊論文及國際研討會論文各一篇。

1. Kuang-Hsiung Tan, Jun-Hao Chen, and Yih-Der Lee, “Intelligent Controlled Dynamic Voltage Restorer for Improving Transient Voltage Quality,” *IEEE Access*, vol. 11, pp. 74686-74701, 2023.
2. Cheng-I Chen, Chung-Hsien Chen, and Yih-Der Lee, “Optimal Energy Management System Based on Particle Swarm Optimization for Microgrid,” *The 6th International Symposium on Computer, Consumer and Control (IS3C)*, June 30 – July 3, 2023, Taichung, Taiwan.

肆、參考文獻

[1] H. Liu, J. Peng, Q. Zang, and K. Yang, ‘‘Control Strategy of Energy Storage for Smoothing Photovoltaic Power Fluctuations,’’ *IFAC-PapersOnLine*, Vol. 48, No. 28, pp. 162–165, 2015.

[2] V. Kumar, ‘‘Application of Moving Averages for PV Power Smoothing Using Battery Energy Storage System,’’ *Int. J. Man-age., Technol. Eng.*, Vol. 8, No. 766, pp. 766–772, 2018.

[3] Yuichi YOSHIDA, Akiko TAKAHASHI, Jun IMAI, and Shigeyuki FUNABIKI, “Power Smoothing Control Methods Using Moving Average and FIR Filters in Distributed Generation Systems,” *Journal of the Japan Institute of Energy*, Vol. 94, No. 9, pp. 1051-1056, 2015.

[4] Alemayehu Addisu, Laurent George, Pierre Courbina, and Vincent Sciandra “Smoothing of Renewable Energy Generation Using Gaussian-Based Method with Power Constraints,” *9th International Conference on Sustainability in Energy and Buildings*, SEB-17, 5-7 July 2017, Chania, Crete, Greece.

[5] M. Akke, "Frequency estimation by demodulation of two complex signals," *IEEE Trans. on Power Delivery*, Vol. 12, No. 1, Jan. 1997, pp. 157-163.

[6] C. Bai, Q. Li, X. Zheng, X. Yin, and Y. Tan, “Dynamic Weighted-Gradient Descent Method with Smoothing Momentum for Distributed Energy Management of Multi-Microgirds Systems,” *IEEE Transactions on Smart Grid*, Vol. 14, No. 6, pp. 4152-4168, Nov. 2023.

[7] X. Yang, Z. Song, J. Wen, L. Ding, M. Zhang, Q. Wu, and S. Cheng, “Network-Constrained Transactive Control

for Multi-Microgrids-based Distribution Networks with Soft Open Points," *IEEE Transactions on Sustainable Energy*, Vol. 14, No. 3, pp. 1769-1783, July 2023.

[8] Y. Wang, D. Qiu, Y. Wang, M. Sun, and G. Strbac, "Graph Learning-Based Voltage Regulation in Distribution Networks with Multi-Microgrids," *IEEE Transactions on Power Systems*, Early Access, Feb. 2023, pp. 1-15.

[9] X. Chen, Y. H. Wang and Y. C. Wang, "A novel seamless transferring control method for microgrid based on master-slave configuration," *2013 IEEE ECCE Asia Downunder*, Melbourne, VIC, pp. 351-357, 2013.

[10] "IEEE Guide for Using IEEE Std 1547 for Interconnection of Energy Storage Distributed Energy Resources with Electric Power Systems," *IEEE Std 1547.9-2022*, Vol., No., pp.1-87, 5 Aug. 2022.

[11] 台灣電力股份有限公司再生能源發電系統併聯技術要點，中華民國 112 年 8 月 2 日。

[12] H. H. Zeineldin and J. L. Kirtley, "Performance of the OVP/UVP and OFP/UFP Method With Voltage and Frequency Dependent Loads," *IEEE Transactions on Power Delivery*, vol. 24, no. 2, pp. 772-778, April 2009.

[13] W. Freitas, Wilsun Xu, C. M. Affonso and Zhenyu Huang, "Comparative Analysis between RoCoF and Vector Surge Relays for Distributed Generation Applications," *IEEE Transactions on Power Delivery*, vol. 20, no. 2, pp. 1315-1324, April 2005.

[14] C. I Chen, S. S. Berutu, Y. C. Chen, H. C. Yang, and C. H. Chen, "Regulated Two-Dimensional Deep Convolutional Neural

Network-Based Power Quality Classifier for Microgrid," *Energies*, 15, 2532, 2022, pp. 1-16.

[15] 電力交易平台參考資料-日前輔助服務市場之交易商品規格，台灣電力公司電力調度處，112 年 08 月 23 日。

IEEE Access
Multidisciplinary | Rapid Review | Open Access Journal

Received 20 June 2023, accepted 6 July 2023, date of publication 11 July 2023, date of current version 26 July 2023.

Digital Object Identifier 10.1109/ACCESS.2023.3293823

RESEARCH ARTICLE

Intelligent Controlled Dynamic Voltage Restorer for Improving Transient Voltage Quality

KUANG-HSIUNG TAN[1], (Member, IEEE), JUN-HAO CHEN[1], AND YIH-DER LEE[2], (Member, IEEE)
[1]Department of Electrical and Electronic Engineering, Chung Cheng Institute of Technology, National Defense University, Taoyuan 335, Taiwan
[2]Nuclear Instrumentation Division, Institute of Nuclear Energy Research, Taoyuan 325, Taiwan

Corresponding author: Kuang-Hsiung Tan (s913115@gmail.com)

This work was supported by the Institute of Nuclear Energy Research of Taiwan under Grant 112A015.

ABSTRACT A dynamic voltage restorer (DVR) is developed to stabilize the three-phase load voltage under the sudden grid voltage distortion conditions, including the voltage sag, swell and unbalance. The DVR is composed of a DC\AC inverter and a DC-link capacitor regarded as the energy storage element. When the sudden grid voltage distortion occurs, the instant power to compensate or absorb is realized by the DC-link capacitor of the DVR resulted in the degenerate stabilization performance and the poor transient voltage quality of the load. Hence, the DC-link voltage control of the DVR for maintaining the constant DC voltage plays an important role in stabilizing the three-phase load voltage. In this study, to improve the transient responses of the three-phase load voltage and the DC-link voltage under the sudden grid voltage distortion conditions, a novel recurrent compensation petri fuzzy neural network (RCPFNN) controller is firstly proposed to replace the conventional proportional-integral (PI) and fuzzy neural network (FNN) controllers for the DC-link voltage control of the DVR. The detailed network structure and the online learning algorithm of the proposed RCPFNN controller are derived. Moreover, some experimental results are given to verify the feasibility and effectiveness of the DVR using the proposed RCPFNN controller for improving the transient voltage quality of the load.

INDEX TERMS Dynamic voltage restorer, voltage quality, voltage sag, intelligent control, recurrent compensation petri fuzzy neural network (RCPFNN).

NOMENCLATURE AND ABBREVIATION

v_{Sa}, v_{Sb}, v_{Sc}	Three-phase grid voltages.
L_s, R_s	Grid impedance.
C_{dc}	DC-link capacitor.
L_{sf}, C_{sf}	LC filter.
T_{sf}	Series transformer.
V_{dc}	DC-link voltage.
v_{Ca}, v_{Cb}, v_{Cc}	Three-phase compensating voltages of DVR.
v_{La}, v_{Lb}, v_{Lc}	Three-phase load voltages.
$v_{S\alpha}, v_{S\beta}$	$\alpha\beta$-axis grid voltages.
$v_{S\alpha}', v_{S\beta}'$	$\alpha\beta$-axis filtered voltages.
$v_{S\alpha}^+, v_{S\beta}^+$	$\alpha\beta$-axis positive-sequence components of grid voltages.
v_{Sd}^+	d-axis positive-sequence voltage.
ω_e	Angular frequency.
θ_e	Electrical angle.
v_{Sd}, v_{Sq}	dq-axis grid voltages.
$\bar{v}_{Sd}, \bar{v}_{Sq}$	dq-axis DC voltage components.
V_m	Actual amplitude of load voltage.
V_m^*	Load voltage command.
v_{Ed}	Reactive component of voltage.
V_{dc}^*	DC-link voltage command.
v_{Eq}	DC-link control voltage.
$v_{La}^*, v_{Lb}^*, v_{Lc}^*$	Three-phase voltage commands.
v_a, v_b, v_c	Three-phase control signals of PWM.
x_i^1	Input variables of RCPFNN.
e	DC-link voltage error.
$\dot{e}$	Derivative of DC-link voltage error.
N	Nth iteration.
y_i^1	Input variable of membership layer.
σ_j^2	Standard deviation of Gaussian function.

The associate editor coordinating the review of this manuscript and approving it for publication was Zhilei Yao.

m_j^2	Mean of Gaussian function.
y_j^2	Output of membership layer.
w_{jk}^3	Connected weight between membership layer and rule layer.
y_k^3	Output of rule layer.
d_{th}	Dynamic threshold value.
t_d^4	Transition of PN.
α, β	Positive parameters of PN.
$y_{d_o}^4$	Output of petri layer.
w_{rc}^5	Recurrent weight.
μ_c^I	Input of recurrent and compensation layer.
y_c^5	Output of recurrent and compensation layer.
γ_1	Compensatory degree.
c_1, d_1	Compensatory degree parameters.
w_c^6	Connected weight between consequent layer and output layer.
y_o^6	Output of RCPFNN.
E	Error function.
δ_o^6	Error term of output layer.
δ_c^5	Error term of recurrent and compensation layer.
δ_d^4	Error term of petri layer.
δ_k^3	Error term of rule layer.
δ_j^2	Error term of membership layer.
η_1	Learning rate of connected weight between recurrent and consequent layer and output layer.
η_2, η_3	Learning rates of compensatory degree parameters.
η_4	Learning rate of recurrent weight.
η_5	Learning rate of mean of Gaussian function.
η_6	Learning rate of standard deviation of Gaussian function.
DVR	Dynamic voltage restorer.
PI	Proportional-integral.
DG	Distributed generator.
PV	Photovoltaic.
FNN	Fuzzy neural network.
CFNN	Compensatory fuzzy neural network.
RNN	Recurrent neural network.
PN	Petri net.
RCPFNN	Recurrent compensation petri fuzzy neural network.
SRF-PLL	Synchronous reference frame phase locked loop.
SOGI-PLL	Second-order generalized integrator phase locked loop.
LP	Low pass.
PWM	Pulse width modulation.
DSP	Digital signal processor.

I. INTRODUCTION

Nowadays, in consequence of the global warming, greenhouse gas emission problem and energy crisis, the penetration rate of the renewable energy-based distributed generator (DG) such as wind turbine generator and photovoltaic (PV) system has been increasing in the utility grid [1], [2], [3], [4]. Moreover, with the increasing critical and sensitive loads, including the adjustable speed drives, computing equipment, switched mode power supplies, communication system, and so on, the power quality issue has been gotten noteworthy attention [5], [6]. However, owing to the high intermittency of the renewable energy resources, unexpected load changes, short circuits and direct-off-line power electronic system, the power quality will be reduced to cause the overload, failure and equipment downtime leading to lost revenue [7], [8]. In other words, the voltage distortion problems, including the grid voltage sag, swell and unbalance, arise and seriously affect the sensitive loads in the power system [9], [10]. According to IEEE 1159-2019 standard [11], the grid voltage sag is defined that the temporary drop of the RMS voltage decreases from 0.1 per unit (pu) to 0.9 pu over a time longer than 0.5 cycles of system frequency but less than 60 seconds. On the other hand, the grid voltage swell is indicated that the RMS voltage is temporarily increased and the start threshold is 1.1 pu [11], [12]. Hence, it is an important issue for the utility grid to stabilize the three-phase load voltage under the sudden grid voltage sag, swell and unbalance conditions.

The dynamic voltage restorer (DVR) is one of the widespread solutions to mitigate the abnormal grid voltage. The main function of the DVR is to instantly inject a voltage compensation with the exact phase and magnitude in series with the source grid. Thus, the three-phase load voltage can be maintained the constant and normal voltage level under the grid voltage sag, swell and unbalance conditions [13], [14], [15]. In terms of the structure, the DVR can be classified into two categories: 1) DVR without energy storage; 2) DVR with energy storage such as the flywheel, capacitor and battery [16]. The power energy for the voltage compensation or absorption of the DVR without energy storage is achieved by the faulted source grid. Hence, the DVR without energy storage can compensate or absorb for longer sag, swell and unbalance. However, the main demerit is the use of the AC\DC converter to connect with the faulted source grid. Consequently, the power losses and cost of the DVR without energy storage will be increased [17]. And the DVR without energy storage may be broken down due to the connection with faulted source grid. On the other hand, the DVR with energy storage isn't equipped with the AC\DC converter to connect with the source grid. The power energy for the voltage compensation or absorption of the DVR with energy storage is realized by the DC-link capacitor or battery. Thus, owing to the simple structure, the DVR with energy storage is a cost-effective solution [18]. Some researches using the DVR for improving the voltage distortion have been proposed [19], [20], [21], [22]. A hybrid energy storage system using robust control algorithm was proposed in [19] to provide superior power supply for multilevel inverter part of the DVR. In [20], an innovative AC voltage synthesizer based on two novelties for the

DVR to compensate the voltage disturbances and ride-through the faults during the voltage disturbance conditions. A photovoltaic system with half-cascaded multilevel inverter is proposed for the DVR to improve the power quality [21]. In [22], two PI-particle swarm optimization controllers were provided to stimulate a DVR for enhancing the on-grid hybrid system under misfire and fire-through faults. In general, the DVR with the DC-link capacitor is widely adopted. However, when the sudden grid voltage distortion conditions occur, the instant power follows into or out of the DC-link capacitor of the DVR resulted in the degenerate stabilization performance and the poor transient voltage quality of the load [18]. Hence, the DC-link voltage control of the DVR for maintaining the constant DC-link voltage plays an important role in stabilizing the three-phase load voltage under the sudden grid voltage sag, swell and unbalance conditions. However, the sluggish regulation of the DC-link voltage of the DVR was obtained by the traditional PI controller in the literature [9], [10], [12], [16].

Though the traditional fuzzy neural network (FNN) has been widely adopted in industrial applications, the fixed fuzzy operator cannot optimize the fuzzy logic reasoning. Moreover, there are not enough free variables to modify the fuzzy operator [23]. Consequently, the compensatory fuzzy neural network (CFNN) has been proposed to solve the demerits of the conventional FNN. The CFNN integrates the compensatory operation with the FNN to adaptively adjust fuzzy membership function and dynamically optimize the adaptive fuzzy operation [24], [25]. Furthermore, the pessimistic fuzzy neuron, optimistic fuzzy neuron, and compensatory fuzzy neuron are implemented by the CFNN to make a superior decision for the situation between the worst and the best cases [26]. Thus, the CFNN is superior to the traditional FNN. The researches using the CFNN for different applications have been proposed [25], [26]. In [25], a photovoltaic system using CFNN controller is proposed to compensate the three-phase unbalanced grid currents under the unbalanced loads. A CFNN with an asymmetric membership function controller is investigated for the distribution static compensator to improve the power quality [26]. Lately, the recurrent neural network (RNN) is developed by using the feedback connections to memorize the temporal characteristics of the input data set [27]. Hence, the RNN is more powerful than the traditional feedforward networks [28]. In other words, since the recurrent connections of the RNN endow the network with memory to obtain more system information, the RNN possesses the ability to deal with the time-varying inputs or outputs and the capability to process the complicated spatiotemporal patterns [29]. In addition, petri net (PN) is a mathematical and graphical tool and is suitable for deadlock analysis, scheduling and control in the automated manufacturing system [30], [31]. Accordingly, the PN possesses the abilities in analysis, modeling and simulation, and the capability to control the various discrete event systems [32]. Hence, in accordance with the merits of the CFNN, RNN and PN, a novel recurrent compensation petri fuzzy neural network (RCPFNN) controller is firstly proposed in this study.

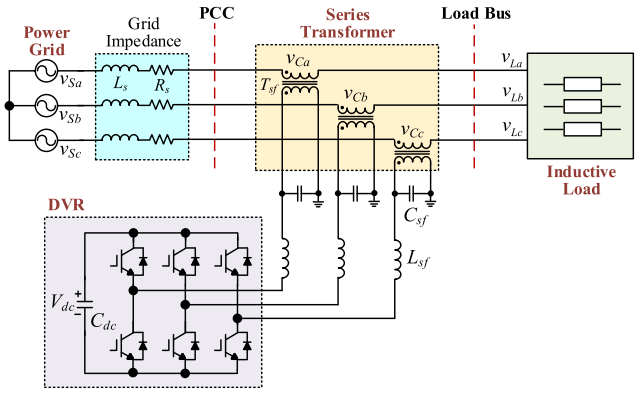

FIGURE 1. Configuration of DVR connected in series with power grid and load.

In this study, a DVR with the DC-link capacitor is developed to stabilize the three-phase load voltage. To improve the transient responses of the three-phase load voltage and the DC-link voltage of the DVR under the sudden grid voltage distortion conditions, including the voltage sag, swell and unbalance, a novel RCPFNN controller is firstly proposed as the DC-link voltage controller to replace the conventional PI and FNN controllers for maintaining the constant DC-link voltage of the DVR. The main contributions of this study are aggregated in the following:

- The successful development of a DVR.
- The successful development of a novel online trained RCPFNN controller for the compensation strategy and the DC-link voltage control of the DVR.
- The successful implementation of the DVR using the proposed RCPFNN controller for the improvements of the three-phase load voltage and DC-link voltage under the sudden grid voltage distortion conditions, including the voltage sag, swell and unbalance.

The operation theories of the DVR will be described in Section II. The detailed network structure and online learning algorithm of the proposed RCPFNN controller are derived in Section III. Then, the feasibility and effectiveness of the DVR using the proposed RCPFNN controller for stabilizing the three-phase load voltage and the DC-link voltage under the sudden grid voltage sag, swell and unbalance conditions are verified by the experimental results compared with the PI and FNN controlled DVRs in Section IV. Finally, some conclusions are provided in Section V.

II. OPERATION THEORIES OF DVR

The configuration of the DVR with the DC-link capacitor C_{dc} is given in Fig. 1. The DVR is connected to the primary winding of the series transformer with the turn ratio 1 through the LC filter (L_{sf}, C_{sf}) and connected in series with the power grid before the inductive load via the secondary winding of the transformer [15], [16]. In this study, the line to line voltage

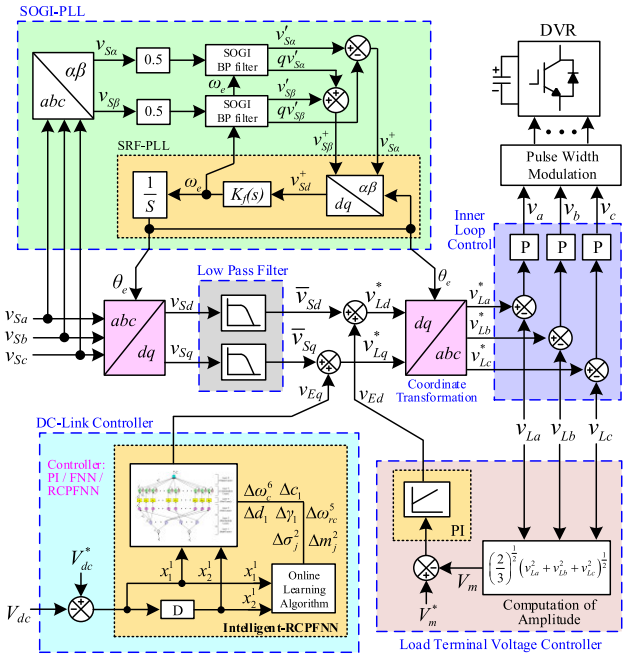

FIGURE 2. Block diagram of DVR using proposed RCPFNN controller for compensation strategy and DC-link voltage control.

and frequency of the power grid are 220 Vrms and 60 Hz, respectively.

A. SYNCHRONIZATION ALGORITHM

The block diagram of the DVR using the proposed RCPFNN controller for the compensation strategy and DC-link voltage control is illustrated in Fig. 2. In order to effectively synchronize with the power grid, a dual second-order generalized integrator phase locked loop (SOGI-PLL) is adopted for the grid synchronization. The dual SOGI-PLL is developed based on the traditional synchronous reference frame PLL (SRF-PLL). The purpose of the dual SOGI-PLL is to overcome the demerit of the SRF-PLL such as the inaccuracy in faulty grid [33]. The SOGI-PLL can obtain the accurate electric angle θ_e by using the positive-sequence components of the grid voltages during the distorted conditions [33]. According to the algorithm of the SOGI-PLL, the three-phase grid voltages v_{Sa}, v_{Sb}, v_{Sc} are detected and the $\alpha\beta$ -axis voltages $v_{S\alpha}, v_{S\beta}$ are calculated by using the $abc/\alpha\beta$ coordinate transformation as follows:

$$\begin{bmatrix} v_{S\alpha} \\ v_{S\beta} \end{bmatrix} = \frac{2}{3}\begin{bmatrix} 1 & -\frac{1}{2} & -\frac{1}{2} \\ 0 & -\frac{\sqrt{3}}{2} & -\frac{\sqrt{3}}{2} \end{bmatrix}\begin{bmatrix} v_{Sa} \\ v_{Sb} \\ v_{Sc} \end{bmatrix} \tag{1}$$

The filtered voltages $v_{S\alpha}^{'}, v_{S\beta}^{'}$ are extracted by using the $\alpha\beta$ axis voltages $v_{S\alpha}, v_{S\beta}$ through the band-pass (BP) filters. Then, the positive-sequence components of the grid voltages $v_{S\alpha}^{+}, v_{S\beta}^{+}$ are obtained as follows:

$$\begin{bmatrix} v_{S\alpha}^{+} \\ v_{S\beta}^{+} \end{bmatrix} = \frac{1}{2}\begin{bmatrix} 1 & -q \\ q & 1 \end{bmatrix}\begin{bmatrix} v_{S\alpha}^{'} \\ v_{S\beta}^{'} \end{bmatrix}, q = e^{j\frac{\pi}{2}} \tag{2}$$

where q is a phase-shift operator in the time domain. The positive-sequence components $v_{S\alpha}^{+}$, $v_{S\beta}^{+}$ are sent to the traditional SRF-PLL and transformed to the dq-axis positive-sequence components via the $\alpha\beta/dq$ coordinate transformation. The d-axis positive-sequence voltage v_{Sd}^{+} is computed as:

$$v_{Sd}^{+} = v_{S\alpha}^{+}\cos\theta_e - v_{S\beta}^{+}\sin\theta_e \tag{3}$$

The angular frequency ω_e is calculated by using the d-axis positive-sequence voltage v_{Sd}^{+} via a proportional controller $K_f(s)$. Then, the electric angle θ_e can be obtained for grid synchronization by using the integral operation.

B. CONTROL ALGORITHM OF DVR

In Fig. 2, the three-phase grid voltages v_{Sa}, v_{Sb}, v_{Sc} are transformed to the dq-axis grid voltages v_{Sd}, v_{Sq} by using the $abc/\alpha\beta$ coordinate transformation. The dq -axis grid voltages v_{Sd}, v_{Sq} consist of the DC component and oscillatory component [10]. The dq-axis DC voltage components $\bar{v}_{Sd}$, $\bar{v}_{Sq}$ are extracted by the low pass (LP) filters. Then, the three-phase load voltages v_{La}, v_{Lb}, v_{Lc} are detected to obtain the actual amplitude V_m of the load voltage by using the following equation:

$$V_m = \sqrt{\frac{2}{3}(v_{La}^2 + v_{Lb}^2 + v_{Lc}^2)} \tag{4}$$

The difference between the load voltage command V_m^* and the actual amplitude V_m of the load voltage is sent to the PI controller to generate the reactive component of voltage v_{Ed} for the regulation of the voltage at the load terminal [10]. The d-axis voltage command$v_{Ld}^*$is acquired by adding the reactive component of voltage v_{Ed} to the d-axis DC voltage component $\bar{v}_{Sd}$. Moreover, in this study, to effectively maintain the constant DC-link voltage of the DVR under the sudden grid voltage sag, swell and unbalance, the DC-link voltage command V_{dc}^* is compared with the actual DC-link voltage V_{dc} to acquire the DC-link voltage error $V_{dc}^* - V_{dc}$. Then, the DC-link voltage error is sent to the traditional PI, FNN or the proposed RCPFNN controller to generate the voltage component v_{Eq} for compensating the power loss and the DC-link voltage control. Thereupon, the voltage component v_{Eq} is added to the q-axis DC voltage component $\bar{v}_{Sq}$ to generate the q-axis voltage command v_{Lq}^*. Then, the three-phase voltage commands $v_{La}^*, v_{Lb}^*, v_{Lc}^*$ are computed by using the dq/abc coordinate transformation as follows to generate the control signals v_a, v_b, v_c via P controllers for the generation of the pulse width modulation (PWM) switching signals of the DVR with the DC-link capacitor.

$$\begin{bmatrix} v_{La}^* \\ v_{Lb}^* \\ v_{Lc}^* \end{bmatrix} = \begin{bmatrix} 1 & 0 \\ -\frac{1}{2} & -\frac{\sqrt{3}}{2} \\ -\frac{1}{2} & \frac{\sqrt{3}}{2} \end{bmatrix}\begin{bmatrix} \cos\theta_e & -sin\theta_e \\ \sin\theta_e & \cos\theta_e \end{bmatrix}\begin{bmatrix} v_{Ld}^* \\ v_{Lq}^* \end{bmatrix} \tag{5}$$

Consequently, according to the above compensation strategy of the DVR, since the q-axis voltage command v_{Lq}^* is composed of the voltage component v_{Eq} generated by the DC-link voltage error $V_{dc}^* - V_{dc}$ through the proposed RCPFNN

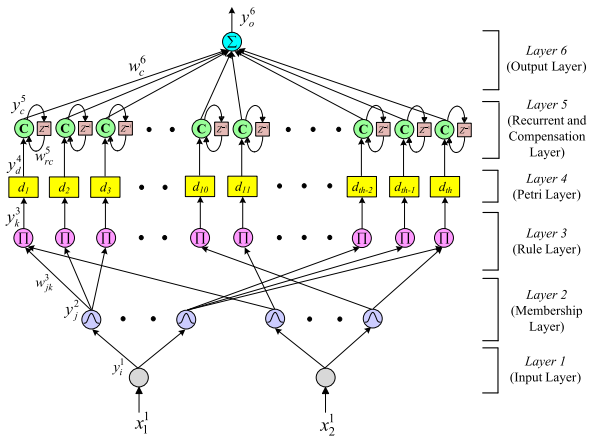

FIGURE 3. Network structure of proposed RCPFNN controller.

controller for compensating the power loss and the DC-link voltage control, the proposed RCPFNN controller for the DVR can improve the three-phase load voltages and DC-link voltage under the grid voltage distortion conditions.

III. INTELLIGENT RCPFNN CONTROLLER

Though the PI controller is popularly employed in different applications on account of its simple structure and easy implementation, some disadvantages of the PI controller, including the poor disturbance rejection, degenerate the control performance [3], [4]. Moreover, since the fixed parameters of the PI controller are designed only for the hypothetical scenarios, the performance of the PI controller will be decreased in the case of the external disturbance and interference such as the sudden grid voltage sag, swell and unbalance. On the other hand, owing to the power following into or out of the DC-link capacitor of the DVR resulted in the degenerate stabilization performance and the poor transient responses under the sudden grid voltage distortion conditions, a novel RCPFNN controller is firstly proposed as the DC-link voltage controller to replace the traditional PI and FNN controllers for improving the transient responses of the three-phase load voltage and the DC-link voltage of the DVR under the sudden grid voltage distortion conditions. The proposed six-layer RCPFNN controller comprises the input layer, membership layer, rule layer, petri layer, recurrent and compensation layer, and the output layer. Furthermore, the network structure of the proposed RCPFNN controller is represented in Fig. 3. The network structure and online learning algorithm of the six-layer RCPFNN controller are detailedly derived as follows:

A. NETWORK STRUCTURE

1) INPUT LAYER

The relationship between the inputs and the outputs of the node in this layer is given as:

$$net_i^1(N) = x_i^1 \tag{6}$$

$$y_i^1(N) = f_i^1\left(net_i^1(N)\right) = net_i^1(N), i = 1, 2 \tag{7}$$

The input variables of the proposed RCPFNN are $x_1^1 = e(t) = V_{dc}^* - V_{dc}$ for the DC-link voltage control of the DVR, and its derivative $x_2^1 = \dot{e}(t)$. N expresses the Nth iteration.

2) MEMBERSHIP LAYER

In membership layer, the fuzzification operation is carried out by each node employing a Gaussian function. The signal propagation of this layer is described in the following:

$$net_j^2(N) = -\frac{\left(y_i^1(N) - m_j^2(N)\right)^2}{\left(\sigma_j^2(N)\right)^2}; i = 1, 2; j = 1, \ldots, h \tag{8}$$

$$y_j^2(N) = f_j^2\left(net_j^1(N)\right) = \exp(net_j^2(N)) \tag{9}$$

where $h = 6$ represents the total number of the linguistic variables. σ_j^2 and m_j^2 denote the standard deviation and the mean of the Gaussian function, respectively.

3) RULE LAYER

In this layer, the multiplication operation denoted by $\prod$ is implemented to multiply the input signals and output the result of product.

$$net_k^3(N) = \prod_j w_{jk}^3 y_j^2(N) \tag{10}$$

$$y_k^3(N) = f_k^3\left(net_k^3(N)\right) = net_k^3(N); \quad k = 1, 2, \ldots, m \tag{11}$$

where $m = 25$ is the total number of the linguistic variables. $w_{jk}^3 = 1$ is the connected weight between the membership layer and the rule layer.

4) PETRI LAYER

In accordance with the PN theory, the competition law is utilized to select the suitable fired nodes for generating the tokens in the petri layer [3], [4]. The PN is composed of two types of nodes: transition and place. When the token is created in input place, the transition is in enable state. Consequently, the condition of the fired or unfired transition can be described as:

$$t_d^4 = \begin{cases} 1, y_k^3 > d_{th} \\ 0, y_k^3 < d_{th}, \end{cases} \quad th = 1, 2, \ldots, m \tag{12}$$

$$d_{th} = \frac{\alpha \exp(-\beta V)}{1 + \exp(-\beta V)} \tag{13}$$

where $t_d^4(N)$ is the transition; α and β are positive constants. The dynamic threshold value d_{th} is varied by the function Vin the following [3]:

$$V = \frac{1}{2}(x_1^1(N) + x_2^1(N)) \tag{14}$$

When the transitions are fired, the required tokens are removed from its input places and new tokens are generated at each output place. On the other hand, when the transitions are

unfired, the token will stay in original input place. Thereupon, the output and input of this layer are given as:

$$net_d^4(N) = \begin{cases} y_k^3(N), t_d^4(N) = 1 \\ 0, t_d^4(N) = 0 \end{cases} \tag{15}$$

$$y_d^4(N) = f_d^4\left(net_d^4(N)\right) = net_d^4(N), \quad d = 1, 2, \ldots, m \tag{16}$$

5) RECURRENT AND COMPENSATION LAYER

The precondition part of the fuzzy logic rules is realized by the nodes in this layer. The compensatory parameters are integrated with this layer to execute IF-condition matching of fuzzy rules. Consequently, the relationship between the input and output of the recurrent and compensation layer is derived in the following:

$$\mu_c^I = \prod_c [y_d^4(N) w_{rc}^5 y_c^5(N-1)] \tag{17}$$

$$net_c^5(N) = (\mu_c^I)^{1-\gamma_l+\frac{\gamma_l}{n}}, \quad \gamma_l = [0, 1], n = 2 \tag{18}$$

$$y_c^5(N) = f_c^5\left(net_c^5(N)\right) = net_c^5(N), \quad c = 1, 2, \ldots, m \tag{19}$$

where $\mu_c^I(N)$ and $y_c^5(N)$ are the input and output of this layer, respectively; w_{rc}^5 is the recurrent weight to memorize the temporal characteristics of the input signals; γ_1 expresses the compensatory degree. If γ_l is trained online, the compensatory operation becomes more adaptive. Moreover, in order to guarantee $\gamma_l \in [0, 1]$, the compensatory degree γ_l is defined as [24], [25]:

$$\gamma_1 = \frac{c_l^2}{c_l^2 + d_l^2} \tag{20}$$

where parameters c_l and d_l will be trained real-time.

6) OUTPUT LAYER

The defuzzification is performed by using the summation operation Σ and depicted as follows:

$$net_o^6(N) = \sum_l w_c^6 y_c^5(N) \tag{21}$$

$$y_o^6(N) = f_o^6(net_0^6(N)) = net_0^6(N), \quad o = 1 \tag{22}$$

where w_c^6 is the connected weight between the output layer and the recurrent and compensation layer; $y_o^6(N)$ is the output of the proposed RCPFNN and is also equal to the voltage component v_{Eq} as shown in Fig. 2 for the DC-link voltage control of the DVR.

B. ONLINE LEARNING

In the proposed RCPFNN, the online learning using a supervised gradient decent method to minimize a given error function E is utilized in this study. The principle of the online learning algorithm is to online tune the parameters of the proposed RCPFNN. In this study, the error function E is given in the following [3]:

$$E = \frac{1}{2}(V_{dc}^* - V_{dc})^2 = \frac{1}{2}e^2 \tag{23}$$

Thereupon, the procedure of the learning algorithm of proposed RCPFNN is detailedly derived as follows:

1) OUTPUT LAYER

In this layer, the error term to be propagated is derived as:

$$\delta_o^6 = -\frac{\partial E}{\partial y_o^6(N)} = -\frac{\partial E}{\partial V_{dc}} \frac{\partial V_{dc}}{\partial y_o^6(N)} \tag{24}$$

In accordance with the chain rule, the connected weight is computed and updated by the following amount.

$$\Delta w_c^6 = -\eta_1 \frac{\partial E}{\partial w_c^6(N)} = -\eta_1 \frac{\partial E}{\partial y_o^6(N)} \frac{\partial y_o^6(N)}{\partial w_c^6(N)} = \eta_1 \delta_o^6 y_c^5 \tag{25}$$

where η_1 is the learning rate. Then, the connected weight w_c^6 is updated as:

$$w_c^6(N+1) = w_c^6(N) + \Delta w_c^6 \tag{26}$$

2) RECURRENT AND COMPENSATION LAYER

The error term to be propagated and computed is described in the following:

$$\delta_c^5 = -\frac{\partial E}{\partial y_c^5(N)} = -\frac{\partial E}{\partial y_o^6} \frac{\partial y_o^6}{\partial y_c^5(N)} = \delta_o^6 w_c^6 \tag{27}$$

Since the compensatory degree γ_l is composed of the parameters c_l and d_l, the updates of the compensatory degree γ_l and the parameters c_l and d_l are calculated by the following amounts:

$$\begin{aligned} \Delta c_l &= -\eta_2 \frac{\partial E}{\partial c_l(N)} = -\eta_2 \frac{\partial E}{\partial \gamma_l(N)} \frac{\partial \gamma_l(N)}{\partial c_l(N)} \\ &= -\eta_2 \frac{\partial E}{\partial \gamma_l(N)} \frac{2c_l(N) d_l(N)^2}{\left(c_l(N)^2 + d_l(N)^2\right)^2} \\ &= \eta_2 \Delta\gamma_l \frac{2c_l(N) d_l(N)^2}{\left(c_l(N)^2 + d_l(N)^2\right)^2} \end{aligned} \tag{28}$$

$$\begin{aligned} \Delta d_l &= -\eta_3 \frac{\partial E}{\partial d_l(N)} = -\eta_3 \frac{\partial E}{\partial \gamma_l(N)} \frac{\partial \gamma_l(N)}{\partial d_l(N)} \\ &= -\eta_3 \frac{\partial E}{\partial \gamma_l(N)} \frac{-2c_l(N)^2 d_l(N)}{\left(c_l(N)^2 + d_l(N)^2\right)^2} \\ &= \eta_3 \Delta\gamma_l \frac{-2c_l(N)^2 d_l(N)}{\left(c_l(N)^2 + d_l(N)^2\right)^2} \end{aligned} \tag{29}$$

$$\begin{aligned} \Delta\gamma_l &= \frac{\partial E}{\partial \gamma_l(N)} = -\frac{\partial E}{\partial y_c^5(N)} \frac{\partial y_c^5(N)}{\partial \gamma_l(N)} \\ &= \delta_c^5 \left(\frac{1}{n} - 1\right) \left(\mu_c^I\right)^{1-\gamma_l+\frac{\gamma_l}{n}} \ln(\mu_c^I)^{1-\gamma_l+\frac{\gamma_l}{n}} \end{aligned} \tag{30}$$

$$\begin{aligned} \Delta w_{rc}^5 &= -\eta_4 \frac{\partial E}{\partial w_{rc}^5(N)} = -\eta_4 \frac{\partial E}{\partial y_o^6(N)} \frac{\partial y_o^6(N)}{\partial y_c^5(N)} \frac{\partial y_c^5(N)}{\partial w_{rc}^5(N)} \\ &= \eta_4 \delta_c^5 (1 - \gamma_l + \frac{\gamma_l}{n}) \left(\mu_c^I\right)^{-\gamma_l+\frac{\gamma_l}{n}} \prod_c [y_d^4(N) y_c^5(N-1)] \end{aligned} \tag{31}$$

where η_2, η_3 and η_4 are the learning rates. The updated values of the parameters c_l and d_l, the compensatory degree γ_l, and the recurrent weight w_{rc}^5 are acquired as:

$$\begin{aligned} c_l(N+1) &= c_l(N) + \Delta c_l \\ &= c_l(N) + \eta_2 \left\{ \frac{2c_l(N)\, d_l^2(N)}{\left[c_l^2(N) + d_l^2(N)\right]^2} \right\} \Delta\gamma_l \end{aligned} \tag{32}$$

$$\begin{aligned} d_l(N+1) &= d_l(N) + \Delta d_l \\ &= d_l(N) + \eta_3 \left\{ \frac{2c_l^2(N)\, d_l(N)}{\left[c_l^2(N) + d_l^2(N)\right]^2} \right\} \Delta\gamma_l \end{aligned} \tag{33}$$

$$\gamma_l(N+1) = \frac{c_l^2(N+1)}{c_l^2(N+1) + d_l^2(N+1)} \tag{34}$$

$$w_{rc}^5(N+1) = w_{rc}^5(N) + \Delta w_{rc}^5 \tag{35}$$

3) PETRI LAYER

The error term of the petri layer is obtained as follows:

$$\begin{aligned} \delta_d^4 &= -\frac{\partial E}{\partial y_d^4(N)} = -\frac{\partial E}{\partial y_c^5(N)} \frac{\partial y_c^5(N)}{\partial y_d^4(N)} \\ &= \delta_c^5 (1 - \gamma_l + \frac{\gamma_l}{n}) \left(\mu_c^l\right)^{-\gamma_l + \frac{\gamma_l}{n}} \prod_c \left[w_{rc}^5 y_c^5(N-1)\right] \end{aligned} \tag{36}$$

4) RULE LAYER

In rule layer, the term of the propagated error can be derived as:

$$\delta_k^3 = -\frac{\partial E}{\partial y_k^3(N)} = -\frac{\partial E}{\partial y_d^4(N)} \frac{\partial y_d^4(N)}{\partial y_k^3(N)} = \delta_d^4 t_d^4 \tag{37}$$

5) MEMBERSHIP LAYER

In this layer, the propagated error term is depicted as:

$$\begin{aligned} \delta_j^2 &= -\frac{\partial E}{\partial net_j^2(N)} \\ &= -\frac{\partial E}{\partial y_k^3(N)} \frac{\partial y_k^3(N)}{\partial y_j^2(N)} \frac{\partial y_{j(N)}^2}{\partial net_j^2(N)} = \sum_k \delta_k^3 y_k^3 \end{aligned} \tag{38}$$

Hence, the updates of the mean Δm_j^2 and standard deviation $\Delta\sigma_j^2$ of the membership functions are represented in the following:

$$\begin{aligned} \Delta m_j^2 &= -\eta_5 \frac{\partial E}{\partial m_j^2(N)} \\ &= -\eta_5 \frac{\partial E}{\partial y_k^3(N)} \frac{\partial y_k^3(N)}{\partial y_j^2(N)} \frac{\partial y_j^2(N)}{\partial net_j^2(N)} \frac{\partial net_j^2(N)}{\partial m_j^2(N)} \\ &= \eta_5 \delta_j^2 \frac{2(y_i^1 - m_j^2)}{(\sigma_j^2)^2} \end{aligned} \tag{39}$$

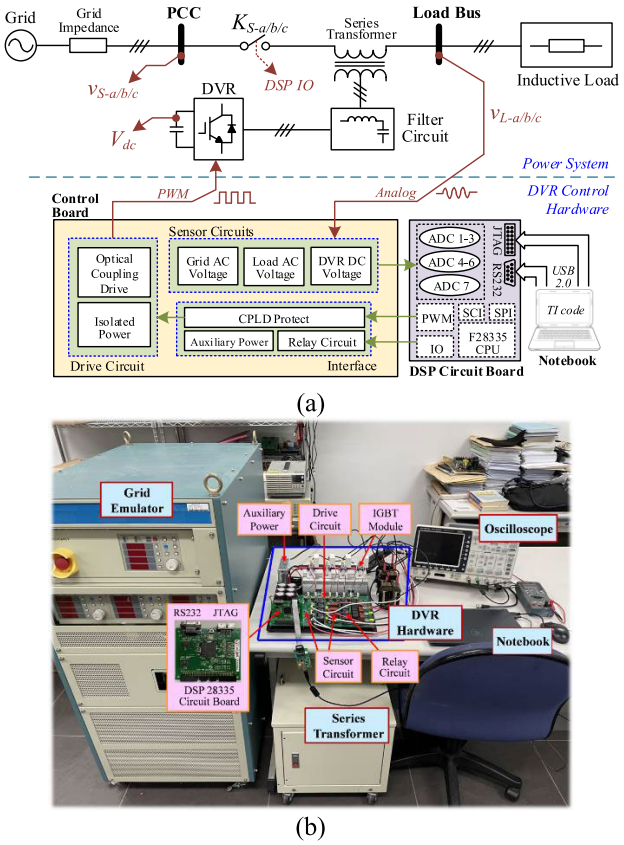

FIGURE 4. Designed DVR control platform. (a) Block diagram of DSP-based DVR. (b) Photo of experimental setup.

$$\begin{aligned} \Delta\sigma_j^2 &= -\eta_6 \frac{\partial E}{\partial \sigma_j^2(N)} \\ &= -\eta_6 \frac{\partial E}{\partial y_k^3(N)} \frac{\partial y_k^3(N)}{\partial y_j^2(N)} \frac{\partial y_j^2(N)}{\partial net_j^2(N)} \frac{\partial net_j^2(N)}{\partial \sigma_j^2(N)} \\ &= \eta_6 \delta_j^2 \frac{2(y_i^1 - m_j^2)^2}{(\sigma_j^2)^2} \end{aligned} \tag{40}$$

where η_5 and η_6 are the learning rates of the mean and standard deviation respectively. Consequently, the updated mean m_j^2 and standard deviation σ_j^2 of the membership functions are given in the following:

$$m_j^2(N+1) = m_j^2(N) + \Delta m_j^2 \tag{41}$$

$$\sigma_j^2(N+1) = \sigma_j^2(N) + \Delta\sigma_j^2 \tag{42}$$

Because of the uncertainties such as external interference, disturbance and parameter variations in the dynamic DVR, the exact calculation of the Jacobian of the DVR, $\partial V_{dc}/\partial y_o^6(N)$, cannot be achieved. Hence, the delta adaptation law is employed to overcome the above problem and to improve the online learning rate of the parameters in the proposed RCPFNN [3], [4].

$$\delta_o^6 \cong e + \dot{e} \tag{43}$$

TABLE 1. Specification of Designed DVR Connected in Series with Power Grid and Load.

Parameters	Values
Grid Voltage : v_S	220 Vrms(L-L), 60 Hz
Grid Impedance : R_s, L_s	1.5m Ω, 0.15 μH
DC-Link Voltage : V_{dc}	450 V
DC-Link Capacitor : C_{dc}	2820 uF
Interfacing Inductor : L_{sf}	3 mH
Ripple Filter : C_{sf}	10 uF
Switching Frequency : f_{sw}	18 kHz
Sampling Frequency : f_s	10 kHz
Series Transformer : T_{sf}	1:1 ratio, 5 kVA
Inductive Load : R_L, L_L	20 Ω, 30 mH

IV. EXPERIMENTAL RESULTS

The DVR to stabilize the three-phase load voltage is developed and provided in Fig. 4. The block diagram of the digital signal processor (DSP)-based DVR is given in Fig. 4(a). The control algorithms of the DVR, including the dual SOGI-PLL and the proposed RCPFNN for the DC-link voltage control are carried out by the DSP TMS320F28335. The control board of the DVR comprises the drive, sensor and the interface circuits. Moreover, the photo of the experimental setup is provided in Fig. 4(b). In this study, an IDRC programmable AC power supply CIF-1530EP9P is adopted to emulate the three-phase faulted grid such as the sudden grid voltage sag, swell and unbalance conditions. Furthermore, the detailed specification of the designed DVR connected in series with the power grid and load is provided in Table 1. Furthermore, the parameters of the PI controller for the DC-link voltage control of the DVR are obtained by trial and error to achieve the best transient and steady-state responses of the DC-link voltage. The proportional gain is 1.3 and the integral gain is 0.38. The proportional gain of the inner loop control is 2.7. The DC-link voltage command V_{dc}^* of the DVR is set to be 450 V. In this study, since the line to line voltage of the power grid is 220 Vrms, the amplitude command V_m^* of the phase voltage is set to be 179 V as shown in Fig. 2. On account of the transient deterioration in the three-phase load voltage and the DC-link voltage of the DVR under the sudden grid voltage distortion conditions, the novel RCPFNN controller is proposed for the DC-link voltage control to improve the transient responses of the load voltage and the DC-link voltage of the DVR in this study. Thus, to verify the effectiveness of the DVR using the proposed RCPFNN for the DC-link voltage control, three test cases are designed in the following: (1) sudden grid voltage sag of 40 % normal value, (2) sudden grid voltage swell of 30 % normal value, and (3) sudden grid voltage unbalance. In addition, the experimental results of the DVR using the PI and FNN controllers are also provided for the comparison.

Firstly, the performance of the DVR under the sudden grid voltage sag is demonstrated. At this scenario, the amplitudes of the three-phase grid voltages decrease from its normal value by 40 % at 0.4 s. The experimental result of the DVR

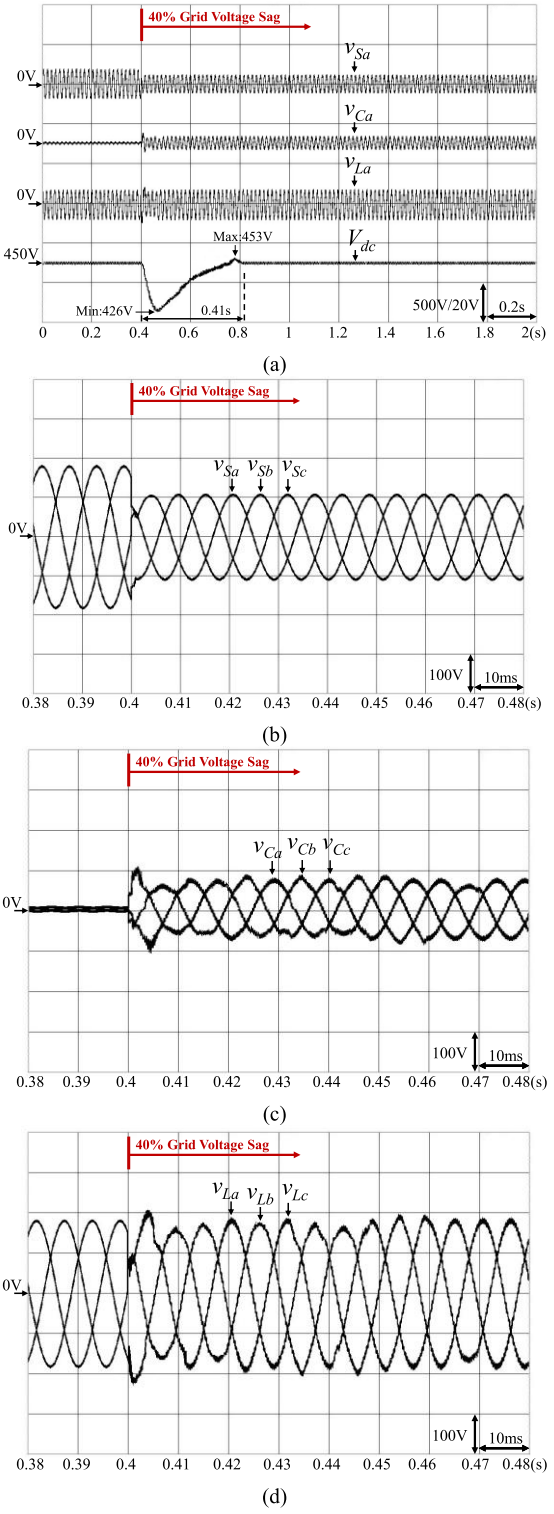

FIGURE 5. Experimental results of DVR using PI controller under voltage sag. (a) Responses of grid voltage, compensating voltage of DVR, load voltage and DC-link voltage of DVR. (b) Responses of three-phase grid voltages for 0.38-0.48 s. (c) Responses of three-phase compensating voltages of DVR for 0.38-0.48 s. (d) Responses of three-phase load voltages for 0.38-0.48 s.

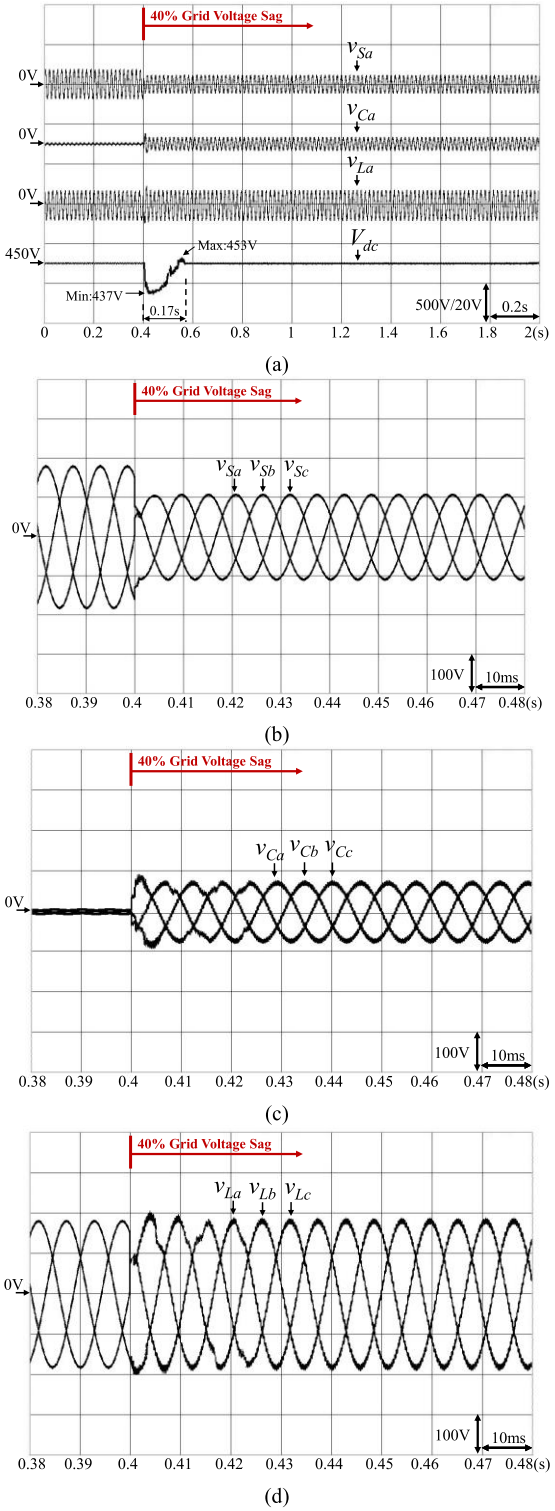

FIGURE 6. Experimental results of DVR using FNN controller under voltage sag. (a) Responses of grid voltage, compensating voltage of DVR, load voltage and DC-link voltage of DVR. (b) Responses of three-phase grid voltages for 0.38-0.48 s. (c) Responses of three-phase compensating voltages of DVR for 0.38-0.48 s. (d) Responses of three-phase load voltages for 0.38-0.48 s.

using PI controller for the DC-link voltage control is provided in Fig. 5. The responses of the grid voltage v_{Sa}, compensating voltage v_{Ca} of the DVR, load voltage v_{La} and the DC-link voltage V_{dc} of the DVR are represented in Fig. 5(a). The responses of the three-phase grid voltages v_{Sa}, v_{Sb}, v_{Sc} in the interval 0.38-0.48 s are provided in Fig. 5(b). The responses of the three-phase compensating voltages v_{Ca}, v_{Cb}, v_{Cc} of the DVR in the interval 0.38-0.48 s are shown in Fig. 5(c). The responses of the three-phase load voltages v_{La}, v_{Lb}, v_{Lc} in the interval 0.38-0.48 s are illustrated in Fig. 5(d). In accordance with the experimental results as shown in Fig. 5, when the power grid is in the normal operation before 0.4 s, the DVR doesn't deliver the compensating voltages v_{Ca}, v_{Cb}, v_{Cc} and the load voltages are equal to the grid voltages v_{Sa}, v_{Sb}, v_{Sc} as shown in Figs. 5(b), 5(c) and 5(d). However, when a sudden voltage sag of 40% normal value occurs at 0.4 s, the DVR dispatches the three-phase compensating voltages v_{Ca}, v_{Cb}, v_{Cc} to maintain the three-phase load voltages v_{La}, v_{Lb}, v_{Lc} as shown in Figs. 5(b), 5(c) and 5(d). Though the effectiveness of the DVR to stabilize the three-phase load voltages is verified, the transient deteriorations in the DC-link voltage V_{dc} of the DVR and the three-phase load voltages v_{La}, v_{Lb}, v_{Lc} are very serious at 0.4 s as shown in Figs. 5(a) and 5(d) due to the disadvantage of the traditional PI controller such as the poor disturbance rejection. The maximum and the minimum fluctuated values of the DC-link voltage V_{dc} of the DVR are 453 V and 426 V respectively. The settling time of the DC-link voltage is 0.41 s as shown in Fig. 5(a). Since the DC-link voltage is fluctuated seriously, the performance of the DVR to stabilize the load voltages is affected resulted in the poor compensating voltages v_{Ca}, v_{Cb}, v_{Cc} and load voltages v_{La}, v_{Lb}, v_{Lc} as shown in Figs. 5(c) and 5(d). Moreover, the transient responses of the three-phase load voltages v_{La}, v_{Lb}, v_{Lc} are still sluggish owing to the poor property of traditional PI controller. In other words, the fixed parameters of the PI controller are unsuitable for different scenarios as shown in Fig. 5(d). Furthermore, the experimental result of the DVR using FNN controller for the DC-link voltage control is represented in Fig. 6. From the experimental results, the transient responses of the DC-link voltage V_{dc} of the DVR and the three-phase load voltages v_{La}, v_{Lb}, v_{Lc} are improved at 0.4 s as shown in Figs. 6(a) and 6(d). The maximum and the minimum fluctuated values of the DC-link voltage V_{dc} of the DVR are 453 V and 437 V respectively. And the settling time of the DC-link voltage is reduced to be 0.17 s as shown in Fig. 6(a). In addition, the experimental result of the DVR using the proposed RCPFNN controller for the DC-link voltage control is provided in Fig. 7. On account of the merits of the proposed RCPFNN controller such as the online learning ability, the abilities to memorize and deal with the time-varying inputs or outputs and the capability to process the complicated spatiotemporal patterns, the transient responses of the DC-link voltage V_{dc} of the DVR and the three-phase load voltages v_{La}, v_{Lb}, v_{Lc} are much improved at 0.4 s as shown in Figs. 7(a) and 7(d). The maximum and the minimum fluctuated values of the DC-link voltage V_{dc} of the DVR are 451 V and 442 V respectively. The settling time of the DC-link voltage is much reduced

to be 0.07 s as shown in Fig. 7(a). Comparing with the experimental results as shown in Figs. 5(d), 6(d) and 7(d), the three-phase load voltages v_{La}, v_{Lb}, v_{Lc} of the DVR using the proposed RCPFNN controller can be effectively stabilized to the normal voltage level at the moment of the voltage sag. In other words, the responses of the three-phase load voltages v_{La}, v_{Lb}, v_{Lc} are smoother than the PI and FNN controllers during the sudden grid voltage sag. Additionally, to verify the online learning ability of the proposed RCPFNN controller, the waveforms of w_1^6, γ_1, m_1^2, σ_1^2, w_1^5 and t_1 of the proposed RCPFNN for the DC-link voltage control under the grid voltage sag as shown in Fig. 7 are represented in Figs. 8(a) and 8(b), respectively. From the responses shown in Fig. 8, the effectiveness of the online learning algorithm and the developed recurrent, petri properties and the compensatory operation in the proposed RCPFNN control are achieved. In other words, since the connected weights, recurrent weights, compensatory degree, mean and standard deviation of the membership functions are trained online, the proposed RCPFNN controller possesses the fast convergence capability to deal with the uncertainties for stabilizing the three-phase load voltages at the moment of the voltage sag.

The performance of the DVR under the sudden grid voltage swell is discussed. At this case, the amplitudes of the three-phase grid voltages v_{Sa}, v_{Sb}, v_{Sc} increase from its normal value by 30 % at 0.4 s. The experimental result of the DVR using PI controller for the DC-link voltage control is shown in Fig. 9. The responses of the grid voltage v_{Sa}, compensating voltage v_{Ca} of the DVR, load voltage v_{La} and the DC-link voltage V_{dc} of the DVR are provided in Fig. 9(a). The responses of the three-phase grid voltages v_{Sa}, v_{Sb}, v_{Sc} in the interval 0.38-0.48 s are illustrated in Fig. 9(b). The responses of the three-phase compensating voltages v_{Ca}, v_{Cb}, v_{Cc} of the DVR in the interval 0.38-0.48 s are represented in Fig. 9(c). The responses of the three-phase load voltages v_{La}, v_{Lb}, v_{Lc} in the interval 0.38-0.48 s are provided in Fig. 9(d). According to the experimental results, when a sudden grid voltage swell of 30 % normal value occurs at 0.4 s, the DVR can dispatch the three-phase compensating voltages v_{Ca}, v_{Cb}, v_{Cc} to stabilize the three-phase load voltages v_{La}, v_{Lb}, v_{Lc} as shown in Figs. 9(c) and 9(d). However, the transient deteriorations in the DC-link voltage V_{dc} of the DVR and the three-phase load voltages v_{La}, v_{Lb}, v_{Lc} are very serious at 0.4 s as shown in Figs. 9(a) and 9(d) on account of the poor disturbance rejection of the traditional PI controller. The maximum and the minimum fluctuated values of the DC-link voltage V_{dc} of the DVR using PI controller are 473 V and 446 V respectively. The settling time of the DC-link voltage is 0.39 s as shown in Fig. 9(a). In other words, the transient responses of the three-phase load voltages v_{La}, v_{Lb}, v_{Lc} are still sluggish and instable as shown in Fig. 9(d). Moreover, the experimental results of the DVR using the FNN and the proposed RCPFNN controllers for the DC-link voltage control under the sudden grid voltage swell are illustrated in Figs. 10 and 11, respectively. Comparing with the experimental results of the DVR using the PI and FNN controllers for the DC-link voltage control, the

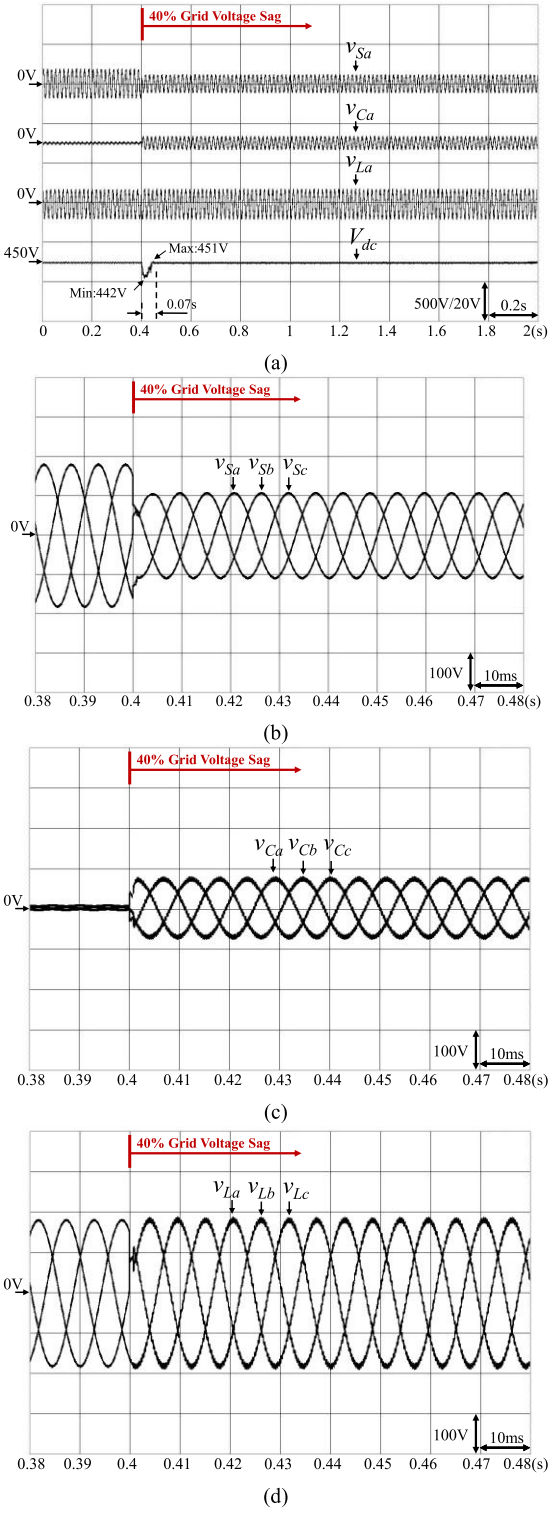

FIGURE 7. Experimental results of DVR using proposed RCPFNN controller under voltage sag. (a) Responses of grid voltage, compensating voltage of DVR, load voltage and DC-link voltage of DVR. (b) Responses of three-phase grid voltages for 0.38-0.48 s. (c) Responses of three-phase compensating voltages of DVR for 0.38-0.48 s. (d) Responses of three-phase load voltages for 0.38-0.48 s.

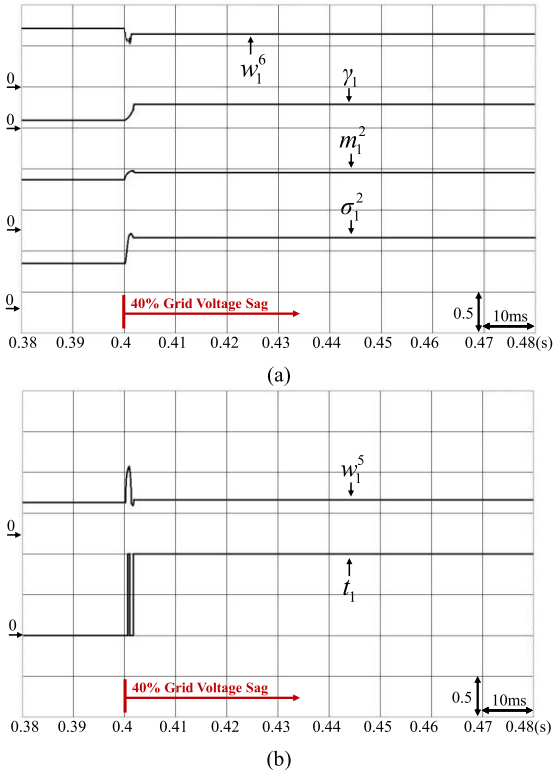

FIGURE 8. Responses of network parameters of proposed RCPFNN controller under grid voltage sag. (a) Waveforms of w_1^6, γ_1, m_1^2 and σ_1^2. (b) Waveforms of w_1^5 and t_1.

three-phase load voltages v_{La}, v_{Lb}, v_{Lc} of the DVR using the proposed RCPFNN controller can be effectively stabilized to the normal voltage level at the moment of the voltage swell as shown in Figs. 9(d), 10(d) and 11(d). The responses of the three-phase load voltages v_{La}, v_{Lb}, v_{Lc} are smoother than the PI and FNN controllers during the sudden grid voltage swell. In addition, the settling time, the overshoot to undershoot of the DC-link voltage error of the DVR using the PI, FNN and the proposed RCPFNN controllers under the grid voltage sag and swell conditions are represented in Figs. 12(a) and 12(b), respectively. According to the experimental results as shown in Figs. 5-12, the transient and steady-state responses of the three-phase load voltages v_{La}, v_{Lb}, v_{Lc} and the DC-link voltage V_{dc} of the DVR using the proposed RCPFNN controller are effectively improved and stabilized under the sudden grid voltage sag and swell conditions in consequence of the online learning ability and the powerful robust ability of the proposed RCPFNN controller.

Finally, in order to verify the feasibility and effectiveness of the DVR using the proposed RCPFNN controller for improving the transient voltage quality of the load under the sudden grid voltage unbalance, the test scenario that the amplitude of the phase-a grid voltage suddenly increases from its normal value by 30 % at 0.4 s is discussed. The experimental result of the DVR using the PI controller for the DC-link voltage control is shown in Fig. 13. The responses

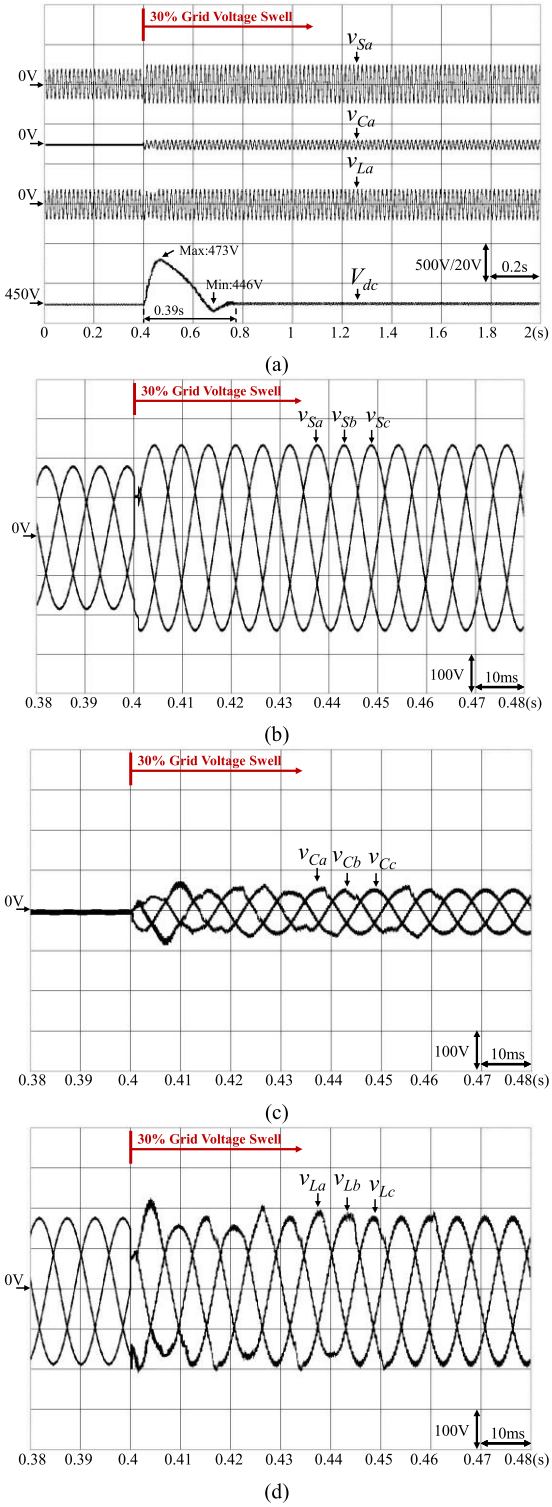

FIGURE 9. Experimental results of DVR using PI controller under voltage swell. (a) Responses of grid voltage, compensating voltage of DVR, load voltage and DC-link voltage of DVR. (b) Responses of three-phase grid voltages for 0.38-0.48 s. (c) Responses of three-phase compensating voltages of DVR for 0.38-0.48 s. (d) Responses of three-phase load voltages for 0.38-0.48 s.

of the grid voltage v_{Sa}, compensating voltage v_{Ca} of the DVR, load voltage v_{La} and the DC-link voltage V_{dc} of the

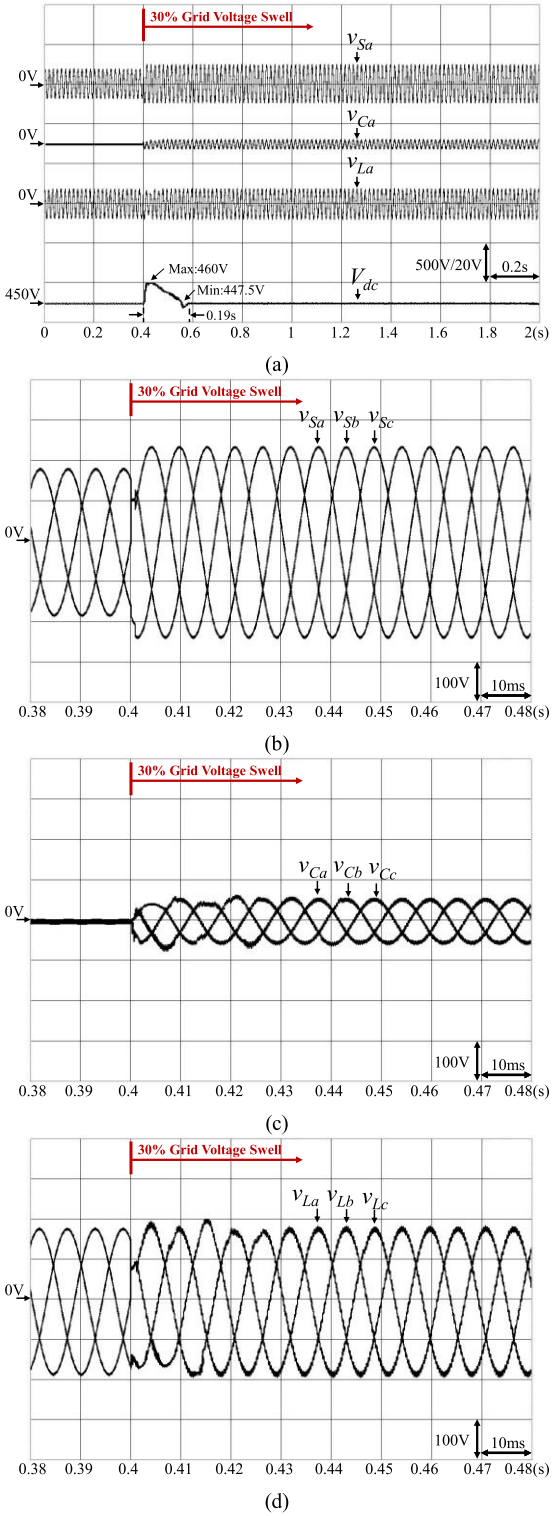

FIGURE 10. Experimental results of DVR using FNN controller under voltage swell. (a) Responses of grid voltage, compensating voltage of DVR, load voltage and DC-link voltage of DVR. (b) Responses of three-phase grid voltages for 0.38-0.48 s. (c) Responses of three-phase compensating voltages of DVR for 0.38-0.48 s. (d) Responses of three-phase load voltages for 0.38-0.48 s.

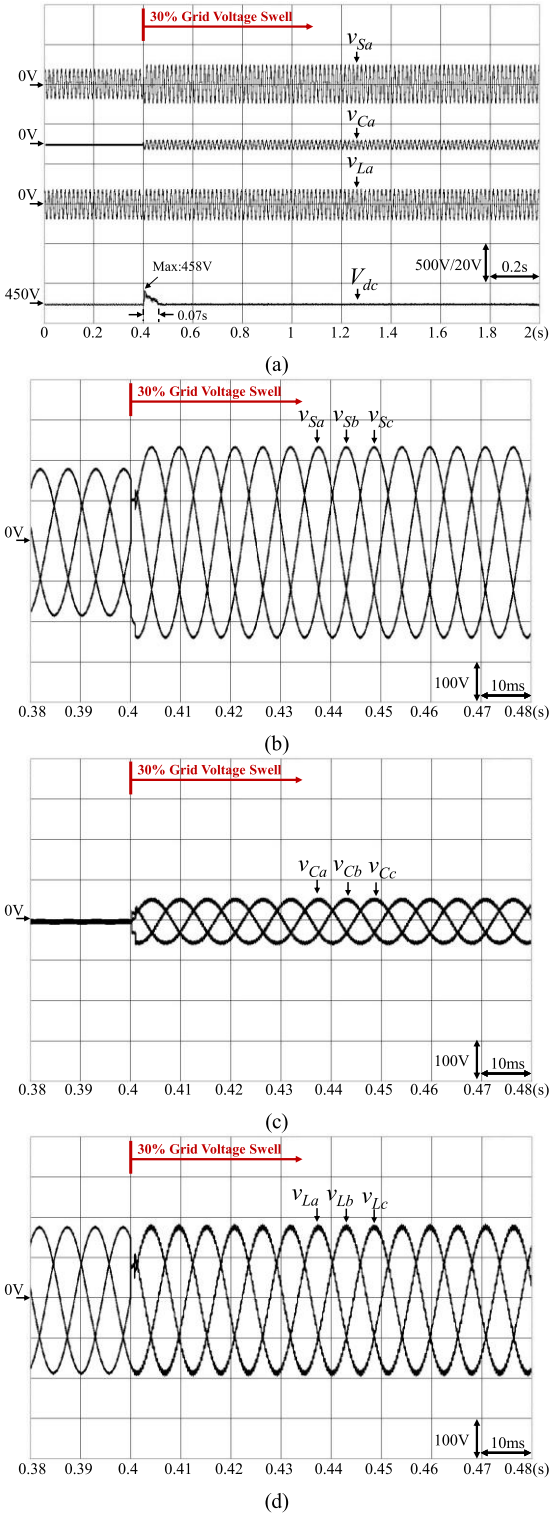

FIGURE 11. Experimental results of DVR using proposed RCPFNN controller under voltage swell. (a) Responses of grid voltage, compensating voltage of DVR, load voltage and DC-link voltage of DVR. (b) Responses of three-phase grid voltages for 0.38-0.48 s. (c) Responses of three-phase compensating voltages of DVR for 0.38-0.48 s. (d) Responses of three-phase load voltages for 0.38-0.48 s.

DVR are provided in Fig. 13(a). The responses of the three-phase unbalanced grid voltages v_{Sa}, v_{Sb}, v_{Sc} in the interval 0.38-0.48 s are given in Fig. 13(b). The responses of the three-phase compensating voltages v_{Ca}, v_{Cb}, v_{Cc} of the DVR

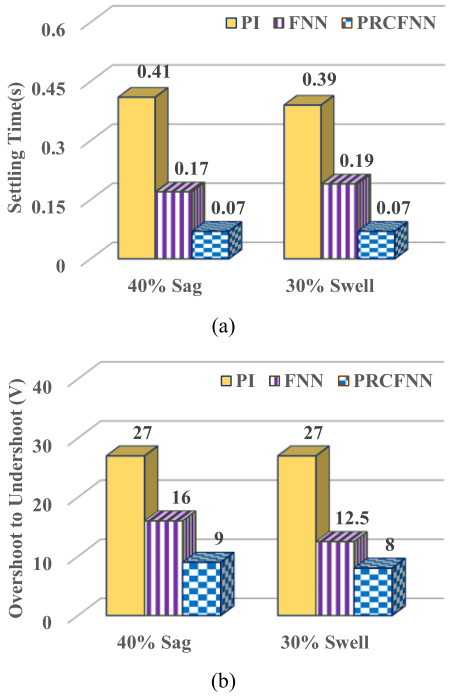

FIGURE 12. Comparison of DVR using different controllers under grid voltage sag and swell conditions. (a) Settling time of DC-link voltage. (b) Overshoot to undershoot of DC-link voltage error.

in the interval 0.38-0.48 s are provided in Fig. 13(c). The responses of the three-phase load voltages v_{La}, v_{Lb}, v_{Lc} in the interval 0.38-0.48 s are represented in Fig. 13(d). According to the experimental results, when the phase-a grid voltage suddenly increases from its normal value by 30 % at 0.4 s, the DVR can dispatch the compensating voltages v_{Ca}, v_{Cb}, v_{Cc} to stabilize the three-phase load voltages v_{La}, v_{Lb}, v_{Lc} as shown in Figs. 13(c) and 13(d). However, the maximum and the minimum fluctuated values of the DC-link voltage V_{dc} of the DVR using the PI controller are 471 V and 446 V, respectively, resulted in the transient deteriorations in the DC-link voltage V_{dc} of the DVR and the three-phase load voltages v_{La}, v_{Lb}, v_{Lc} on account of the poor disturbance rejection of the traditional PI controller as shown in Figs. 13(a) and 13(d). The settling time of the DC-link voltage is 0.36 s. Moreover, the experimental results of the DVR using the FNN and the proposed RCPFNN controllers for the DC-link voltage control under the sudden voltage unbalance are represented in Figs. 14 and 15, respectively. According to the experimental result using the proposed RCPFNN controller under the sudden voltage unbalance, the stability and the transient response of the three-phase load voltages v_{La}, v_{Lb}, v_{Lc} and the DC-link voltage V_{dc} of the DVR are better than the PI and FNN controllers at the moment of the voltage unbalance as shown in Figs. 13-15. The maximum and the minimum fluctuated values of the DC-link voltage V_{dc} of the DVR using the proposed RCPFNN controller are much reduced to be 457.5 V and 450 V, respectively. The settling time of the DC-link voltage is also much reduced to be

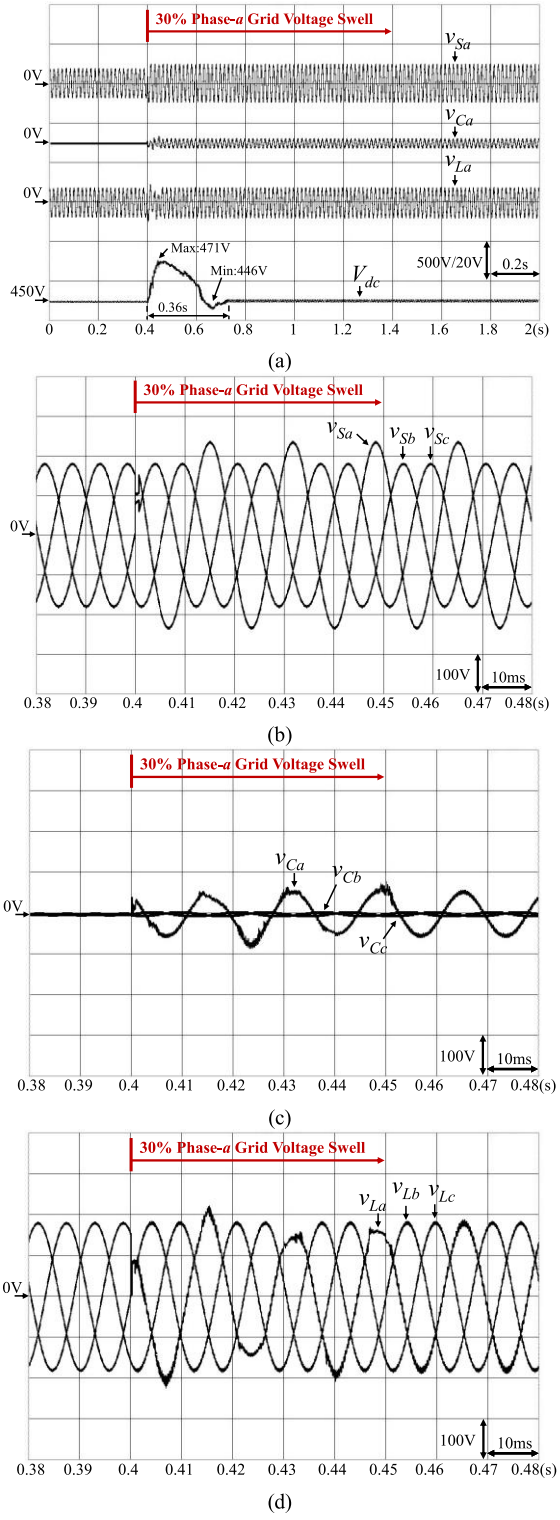

FIGURE 13. Experimental results of DVR using PI controller under voltage unbalance. (a) Responses of grid voltage, compensating voltage of DVR, load voltage and DC-link voltage of DVR. (b) Responses of three-phase unbalanced grid voltages for 0.38-0.48 s. (c) Responses of three-phase compensating voltages of DVR for 0.38-0.48 s. (d) Responses of three-phase load voltages for 0.38-0.48 s.

0.07 s as shown in Fig. 15(a). Therefore, the transient voltage quality of the load is guaranteed by using the proposed

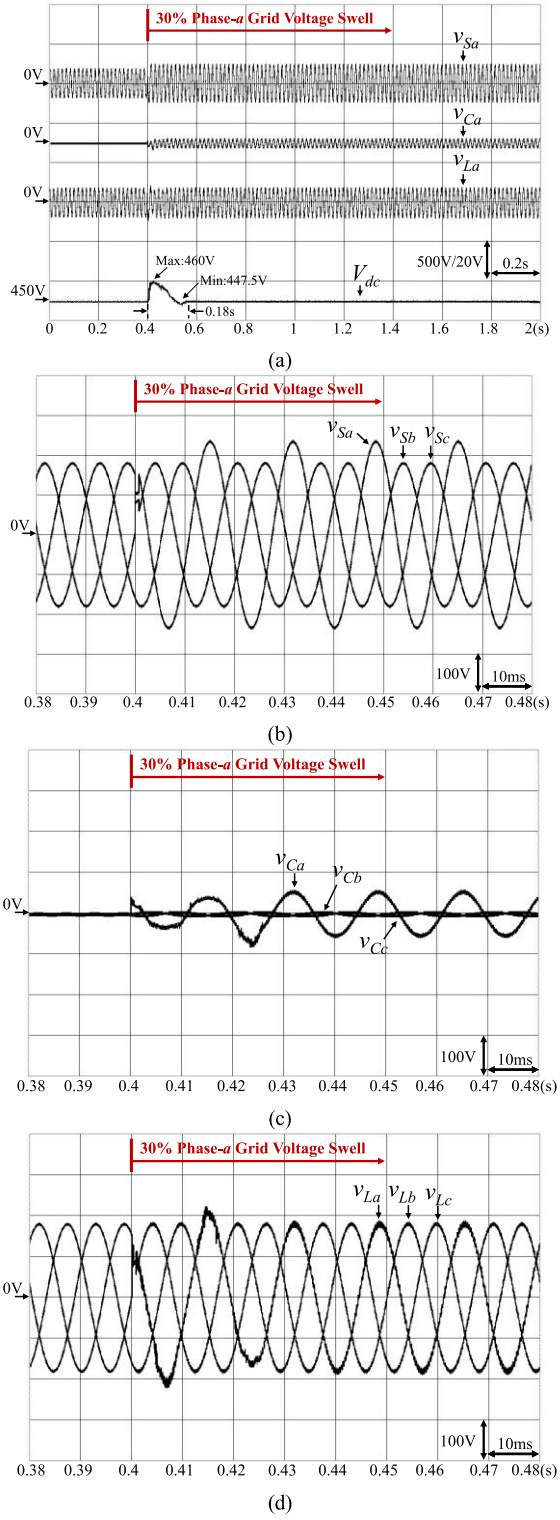

FIGURE 14. Experimental results of DVR using FNN controller under voltage unbalance. (a) Responses of grid voltage, compensating voltage of DVR, load voltage and DC-link voltage of DVR. (b) Responses of three-phase unbalanced grid voltages for 0.38-0.48 s. (c) Responses of three-phase compensating voltages of DVR for 0.38-0.48 s. (d) Responses of three-phase load voltages for 0.38-0.48 s.

RCPFNN controller for the DVR under the sudden grid voltage unbalance condition.

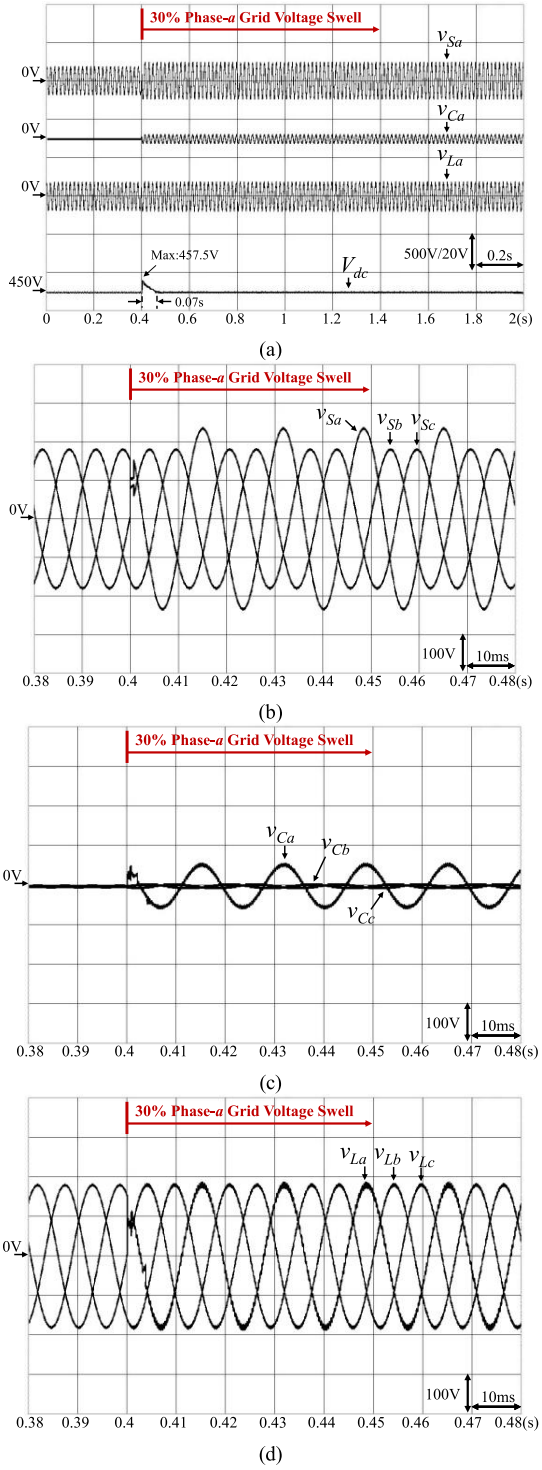

FIGURE 15. Experimental results of DVR using proposed RCPFNN controller under voltage unbalance. (a) Responses of grid voltage, compensating voltage of DVR, load voltage and DC-link voltage of DVR. (b) Responses of three-phase unbalanced grid voltages for 0.38-0.48 s. (c) Responses of three-phase compensating voltages of DVR for 0.38-0.48 s. (d) Responses of three-phase load voltages for 0.38-0.48 s.

V. CONCLUSION

In this study, a DVR has been successfully developed and implemented to stabilize the three-phase load voltages

under the grid voltage sag, swell and unbalance conditions. Since the power energy follows into or out of the DC-link capacitor of the DVR resulted in the degenerate stabilization performance and the poor transient response under the sudden grid voltage distortion conditions, a novel RCPFNN controller is firstly proposed to replace the traditional PI and FNN controllers for the DC-link voltage control and the compensation strategy. Moreover, the effectiveness and the feasibility of the DVR using the proposed RCPFNN controller as the DC-link voltage controller are verified by the experimental results. According to the experimental results, owing to the online learning ability and powerful robust ability of the proposed RCPFNN controller, the transient responses of the three-phase load voltages v_{La}, v_{Lb}, v_{Lc} and the DC-link voltage V_{dc} of the DVR using the proposed RCPFNN controller are effectively improved and stabilized comparing with the PI and FNN controllers under the sudden grid voltage distortion conditions.

The major contributions of this study are: (i) the successful development of a DVR; (ii) the successful development of a novel online trained RCPFNN controller for the compensation strategy and the DC-link voltage control of the DVR; (iii) the successful implementation of the DVR using the proposed RCPFNN controller for the improvements of the three-phase load voltages and DC-link voltage under the sudden grid voltage distortion conditions, including the voltage sag, swell and unbalance.

REFERENCES

[1] E. M. Molla and C.-C. Kuo, "Voltage sag enhancement of grid connected hybrid PV-wind power system using battery and SMES based dynamic voltage restorer," *IEEE Access*, vol. 8, pp. 130003–130013, 2020.

[2] A. Benali, M. Khiat, T. Allaoui, and M. Denaï, "Power quality improvement and low voltage ride through capability in hybrid wind-PV farms grid-connected using dynamic voltage restorer," *IEEE Access*, vol. 6, pp. 68634–68648, 2018.

[3] K.-H. Tan and T.-Y. Tseng, "Seamless switching and grid reconnection of microgrid using Petri recurrent wavelet fuzzy neural network," *IEEE Trans. Power Electron.*, vol. 36, no. 10, pp. 11847–11861, Oct. 2021.

[4] F.-J. Lin, K.-H. Tan, C.-F. Chang, M.-Y. Li, and T.-Y. Tseng, "Development of intelligent controlled microgrid for power sharing and load shedding," *IEEE Trans. Power Electron.*, vol. 37, no. 7, pp. 7928–7940, Jul. 2022.

[5] S. Biricik, H. Komurcugil, N. D. Tuyen, and M. Basu, "Protection of sensitive loads using sliding mode controlled three-phase DVR with adaptive notch filter," *IEEE Trans. Ind. Electron.*, vol. 66, no. 7, pp. 5465–5475, Jul. 2019.

[6] A. Moghassemi, S. Padmanaban, V. K. Ramachandaramurthy, M. Mitolo, and M. Benbouzid, "A novel solar photovoltaic fed TransZSI-DVR for power quality improvement of grid-connected PV systems," *IEEE Access*, vol. 9, pp. 7263–7279, 2021.

[7] A. M. Gee, F. Robinson, and W. Yuan, "A superconducting magnetic energy storage-emulator/battery supported dynamic voltage restorer," *IEEE Trans. Energy Convers.*, vol. 32, no. 1, pp. 55–64, Mar. 2017.

[8] S. F. Al-Gahtani, A. B. Barnawi, H. Z. Azazi, S. M. Irshad, J. K. Bhutto, and E. Z. M. Salem, "A new technique implemented in synchronous reference frame for DVR control under severe sag and swell conditions," *IEEE Access*, vol. 10, pp. 25565–25579, 2022.

[9] P. Kanjiya, B. Singh, A. Chandra, and K. Al-Haddad, "'SRF theory revisited' to control self-supported dynamic voltage restorer (DVR) for unbalanced and nonlinear loads," *IEEE Trans. Ind. Appl.*, vol. 49, no. 5, pp. 2330–2340, Sep. 2013.

[10] P. Jayaprakash, B. Singh, D. P. Kothari, A. Chandra, and K. Al-Haddad, "Control of reduced-rating dynamic voltage restorer with a battery energy storage system," *IEEE Trans. Ind. Appl.*, vol. 50, no. 2, pp. 1295–1303, Mar. 2014.

[11] *IEEE Recommended Practice for Monitoring Electric Power Quality*, Standard IEEE 1159–2019, 1969.

[12] P. Li, L. Xie, J. Han, S. Pang, and P. Li, "New decentralized control scheme for a dynamic voltage restorer based on the elliptical trajectory compensation," *IEEE Trans. Ind. Electron.*, vol. 64, no. 8, pp. 6484–6495, Aug. 2017.

[13] A. P. Torres, P. Roncero-Sánchez, and V. F. Batlle, "A two degrees of freedom resonant control scheme for voltage-sag compensation in dynamic voltage restorers," *IEEE Trans. Power Electron.*, vol. 33, no. 6, pp. 4852–4867, Jun. 2018.

[14] P. Li, L. Xie, J. Han, S. Pang, and P. Li, "A new voltage compensation philosophy for dynamic voltage restorer to mitigate voltage sags using three-phase voltage ellipse parameters," *IEEE Trans. Power Electron.*, vol. 33, no. 2, pp. 1154–1166, Feb. 2018.

[15] M. Pradhan and M. K. Mishra, "Dual *P-Q* theory based energy-optimized dynamic voltage restorer for power quality improvement in a distribution system," *IEEE Trans. Ind. Electron.*, vol. 66, no. 4, pp. 2946–2955, Apr. 2019.

[16] P. Li, Y. Wang, M. Savaghebi, J. Lu, X. Pan, and F. Blaabjerg, "Identification design for dynamic voltage restorer to mitigate voltage sag based on the elliptical transformation," *IEEE J. Emerg. Sel. Topics Power Electron.*, vol. 9, no. 5, pp. 5672–5686, Oct. 2021.

[17] S. Kim, H.-G. Kim, and H. Cha, "Dynamic voltage restorer using switching cell structured multilevel AC–AC converter," *IEEE Trans. Power Electron.*, vol. 32, no. 11, pp. 8406–8418, Nov. 2017.

[18] J. Wang, Y. Xing, H. Wu, and T. Yang, "A novel dual-DC-port dynamic voltage restorer with reduced-rating integrated DC–DC converter for wide-range voltage sag compensation," *IEEE Trans. Power Electron.*, vol. 34, no. 8, pp. 7437–7449, Aug. 2019.

[19] A. D. Falehi and H. Torkaman, "Robust fractional-order super-twisting sliding mode control to accurately regulate lithium-battery/super-capacitor hybrid energy storage system," *Int. J. Energy Res.*, vol. 45, no. 13, pp. 18590–18612, Oct. 2021.

[20] A. D. Falehi and H. Torkaman, "Promoted supercapacitor control scheme based on robust fractional-order super-twisting sliding mode control for dynamic voltage restorer to enhance FRT and PQ capabilities of DFIG-based wind turbine," *J. Energy Storage*, vol. 42, pp. 1–23, Oct. 2021.

[21] A. D. Falehi, "Half-cascaded multilevel inverter coupled to photovoltaic power source for AC-voltage synthesizer of dynamic voltage restorer to enhance voltage quality," *Int. J. Numer. Modelling, Electron. Netw., Devices Fields*, vol. 34, no. 5, pp. 1–21, Aug. 2021.

[22] M. Osama abed elraouf, M. Aljohani, M. I. Mosaad, and T. A. AbdulFattah, "Mitigating misfire and fire-through faults in hybrid renewable energy systems utilizing dynamic voltage restorer," *Energies*, vol. 15, no. 16, pp. 1–16, Aug. 2022.

[23] Y.-Y. Lin, J.-Y. Chang, and C.-T. Lin, "A TSK-type-based self-evolving compensatory interval type-2 fuzzy neural network (TSCIT2FNN) and its applications," *IEEE Trans. Ind. Electron.*, vol. 61, no. 1, pp. 447–459, Jan. 2014.

[24] C.-J. Lin and C.-H. Chen, "Identification and prediction using recurrent compensatory neuro-fuzzy systems," *Fuzzy Sets Syst.*, vol. 150, no. 2, pp. 307–330, Mar. 2005.

[25] F.-J. Lin, K.-H. Tan, Y.-K. Lai, and W.-C. Luo, "Intelligent PV power system with unbalanced current compensation using CFNN-AMF," *IEEE Trans. Power Electron.*, vol. 34, no. 9, pp. 8588–8598, Sep. 2019.

[26] K. H. Tan, F. J. Lin, C. Y. Tsai, and Y. R. Chang, "A distribution static compensator using a CFNN-AMF controller for power quality improvement and DC-link voltage regulation," *Energies*, vol. 11, no. 8, pp. 1–17, Aug. 2018.

[27] Y.-T. Liu, Y.-Y. Lin, S.-L. Wu, C.-H. Chuang, and C.-T. Lin, "Brain dynamics in predicting driving fatigue using a recurrent self-evolving fuzzy neural network," *IEEE Trans. Neural Netw. Learn. Syst.*, vol. 27, no. 2, pp. 347–360, Feb. 2016.

[28] Y. Chu, J. Fei, and S. Hou, "Adaptive global sliding-mode control for dynamic systems using double hidden layer recurrent neural network structure," *IEEE Trans. Neural Netw. Learn. Syst.*, vol. 31, no. 4, pp. 1297–1309, Apr. 2020.

[29] K.-H. Tan, F.-J. Lin, C.-M. Shih, and C.-N. Kuo, "Intelligent control of microgrid with virtual inertia using recurrent probabilistic wavelet fuzzy neural network," *IEEE Trans. Power Electron.*, vol. 35, no. 7, pp. 7451–7464, Jul. 2020.
[30] R. J. Rodríguez, S. Bernardi, and A. Zimmermann, "An evaluation framework for comparative analysis of generalized stochastic Petri net simulation techniques," *IEEE Trans. Syst. Man, Cybern. Syst.*, vol. 50, no. 8, pp. 2834–2844, Aug. 2020.
[31] J. Li, X. Yu, and M. Zhou, "Analysis of unbounded Petri net with lean reachability trees," *IEEE Trans. Syst. Man, Cybern. Syst.*, vol. 50, no. 6, pp. 2007–2016, Jun. 2020.
[32] H. Kaid, A. Al-Ahmari, E. A. Nasr, A. Al-Shayea, A. K. Kamrani, M. A. Noman, and H. A. Mahmoud, "Petri net model based on neural network for deadlock control and fault detection and treatment in automated manufacturing systems," *IEEE Access*, vol. 8, pp. 103219–103235, 2020.
[33] F.-J. Lin, K.-C. Lu, and B.-H. Yang, "Recurrent fuzzy cerebellar model articulation neural network based power control of a single-stage three-phase grid-connected photovoltaic system during grid faults," *IEEE Trans. Ind. Electron.*, vol. 64, no. 2, pp. 1258–1268, Feb. 2017.

KUANG-HSIUNG TAN (Member, IEEE) received the B.S., M.S., and Ph.D. degrees in electrical and electronic engineering from the Chung Cheng Institute of Technology (CCIT), National Defense University, Taiwan, in 2002, 2007, and 2013, respectively. He has been a Faculty Member at CCIT, where he is currently an Associate Professor with the Department of Electrical and Electronic Engineering. His teaching and research interests include power electronics, power quality, microgrid systems, and intelligent control.

JUN-HAO CHEN received the M.S. degree in electrical engineering from National Central University, Taiwan, in 2017. He is currently pursuing the Ph.D. degree in electrical engineering with the Chung Cheng Institute of Technology (CCIT), National Defense University, Taiwan. His research interests include active power filters, intelligent control, and power electronics.

YIH-DER LEE (Member, IEEE) received the B.S. and M.S. degrees in electrical engineering from the National Taiwan University of Science and Technology, Taipei, Taiwan, in 1997 and 1999, respectively, and the Ph.D. degree in electrical engineering from National Sun Yat-Sen University (NSYSU), in 2009. From 1998 to 2010, he was an Associate Technical Specialist at Southern District Waste Management Plant, Environment Protection Bureau, Kaohsiung City Government, Taiwan. Since 2010, he has been with the Institute of Nuclear Energy Research (INER), Atomic Energy Council, and currently, he is a Researcher and the Nuclear Instrumentation Division Depute Director, which is responsible for developing microgrid and smart grid technology. His research interests include renewable energy, microgrid, power electronics, power system control, and stability.

Optimal Energy Management System Based on Particle Swarm Optimization for Microgrid

Cheng-I Chen
*Department of Electrical Engineri*ng,
National Central University
Taoyuan, Taiwan
cichen@ee.ncu.edu.tw

Chung-Hsien Chen
Metal Industries Research and Development Centre
Taichung, Taiwan
jacky@mail.mirdc.org.tw

Yih-Der Lee
Nuclear Instrumentation Division
Institute of Nuclear Energy Research
Taoyuan, Taiwan
ydlee@iner.org.tw

***Abstract*—Due to the severe global warming and the shortage of fossil fuels such as crude oil and coal in recent years, the government is also actively promoting the integration of renewable energy with microgrids. However, the instability of renewable energy would result in scheduling doubts of energy. It needs to be equipped with a battery energy storage system to effectively solve this problem and make energy storage for renewable energy. At the same time, it means that the microgrid needs to cope with various operating scenarios, weather, power events and other emergency capabilities, making the control strategy particularly important, thereby increasing the efficiency of energy use and stably outputting to the load. This article integrates solar power generation, energy storage system and fuel cell in microgrid, based on the remaining battery power and solar power generation as the benchmark for energy dispatch, and controls the power dispatch of generators and energy storage systems through the energy management proposed in this article. In response to different renewable energy power generation, power generation cost and demand are optimized for power allocation, which effectively improves the efficiency of energy use and achieves the goal of minimizing electricity costs.**

Keywords—microgrid, optimal energy management, renewable energy, battery energy storage system, fuel cell

I. INTRODUCTION

In recent years, with the rapid advancement of technology, global energy demand has been increasing. However, this growing demand for energy has led to issues such as rising fuel prices and climate change. To address the uneven distribution of energy resources, international organizations engage in various communication platforms to negotiate and promote a balance in energy supply. According to the World Energy Statistics by BP (British Petroleum), the current primary sources of global electricity generation are fossil fuels (61.3%), nuclear power (10.1%), hydroelectric power (16%), and renewable energy (11.7%) [1]. The combustion of fossil fuels such as oil, natural gas, and coal not only generates carbon monoxide (CO), nitrogen oxides (NOx), sulfur oxides (SOx), and particulate matter, but also exacerbates air pollution and global warming. Some countries have transitioned to carbon-reducing and cost-effective nuclear power for electricity generation. However, after the unexpected Fukushima nuclear power plant accident on March 11, 2011, many of these countries have hesitated, leading to increased attention towards renewable energy. In response, several governments have proposed and taken action on net-zero emissions by 2050. The public recognizes the benefits of low environmental impact renewable energy, making the development of self-sufficient energy sources an urgent matter.

In traditional power systems, the centralized generation is primarily used, where electricity generated by large power plants is transmitted through various levels of substations to meet the demand of users. To enhance the supply quality and stability of the power system, the integration of distributed generation (DG) to form the microgrid is necessary [2], [3]. DG is located closer to the load centers compared to centralized generation, which helps avoid losses associated with long-distance power transmission and enables on-site generation in areas where establishing long transmission lines is impractical. However, the intermittent and unstable nature of DG poses challenges, as its increased penetration can impact the stability of the grid. The introduction of energy management systems and energy storage devices can help stabilize voltage and frequency, facilitating the integration of renewable energy into the grid [4]-[6].

Considering the extension of the operating time of microgrids and the reduction of environmental impact, optimal scheduling needs to consider not only the reduction of fuel costs for generators but also maintenance costs and environmental pollution costs. Based on the above considerations, several research directions shall be identified.

- How to minimize energy storage depletion or curtailment of renewable energy production, aiming to increase the lifespan of energy storage systems;

- How to allocate the electricity generated from green energy sources in situations where the grid supply is unavailable, ensuring the functionality and resilience of essential services;

- Integrating economic costs and other parameters into the scheduling process to improve the overall efficiency of the system and utilizing algorithmic optimization methods for real-time economic dispatch of microgrids.

In this paper, the optimal energy management based on particle swarm optimization (PSO) for microgrid by considering the above points is proposed.

II. MODELS AND OPTIMAL ENERGY MANAGEMENT

In order to perform the real-time energy management, the energy resources are necessary to be modeled. In this section, the models in this study is introduced in the section II.A. Then, the commonly used rule-based method and the proposed strategy are illustrated.

A. Models of Energy Resources

For the solar power generation, the equivalent output energy can be represented in (1), where $E_{PV}(t)$ is the available energy of solar power at time t, η_{PV} is the coefficient of solar system, η_{inv} is the operational efficiency of solar power converter, I is the solar irradiation (unit in W/m^2), and A_{PV} is the effective irradiation area. The Long Short-Term Memory (LSTM) neural network is utilized for the prediction of solar power generation in this study [7].

$$E_{PV}(t) = (\eta_{PV}\eta_{inv})(A_{PV}I) \quad (1)$$

As an important component of microgrids, energy storage systems play a crucial role in enhancing the reliability and stability of the power grid. They facilitate the power dispatch between generators, renewable energy sources, transmission and distribution networks, and loads, mitigating the pressure caused by supply-demand imbalances and unexpected events on the grid. Typically, an energy storage system consists of a set of batteries and bidirectional converters. The charging and discharging conversion efficiency usually ranges from 95% to 97%. The energy capacity can be represented by a nonlinear equation, as shown in (2). In (2), $SOC(t)$ is the state of charge, $P_{ch}(t)$ is the charging power, and $P_{dis}(t)$ is the discharging power for storage system at time t, respectively. η_{ch} is the charging efficiency and η_{dis} is the discharging efficiency for the storage system. And Δt is the time duration.

$$SOC(t) = \begin{cases} SOC(t-\Delta t) + P_{ch}(t)\eta_{ch}\Delta t \\ SOC(t-\Delta t) - \dfrac{P_{dis}(t)\Delta(t)}{\eta_{dis}} \end{cases} \quad (2)$$

Equation (2) can be represented in (3), where SOC_0 is the initial state of charge, C_b is the capacity of battery storage system, A_t and B_t are the binary constants to indicate the charging and discharging states, respectively.

$$SOC(t) = SOC_0 + \frac{1}{C_b}\sum_{t=1}^{T}\left[A_t P_{ch}(t)\eta_{ch} - B_t \frac{P_{dis}(t)}{\eta_{dis}} \right] \cdot \Delta t \quad (3)$$

B. Optimal Energy Management

To perform the optimal energy management, it is necessary to set up the cost function for the microgrid system. For this study, the installation cost of solar system is not taken into account. The operational cost of solar power generation can be presented in (4), where C_{PV} is the operational cost of solar power, k_{PV} is the operational and maintenance cost coefficient, $P_{PV}(t)$ is the output power of solar system at time t, and T is the total operational duration.

$$C_{PV} = \sum_{t=1}^{T} k_{PV} P_{PV}(t) \quad (4)$$

The cost of an energy storage system includes operational and maintenance costs. In order to prolong the battery's lifespan, it is necessary to plan for the appropriate range of battery charge/discharge levels, so as to avoid overcharging or overdischarging the battery. The operational cost of battery storage system is listed in Table I referred to [8].

TABLE I. OPERATIONAL COST COEFFICENTS OF STORAGE SYSTEM

Range of SOC	NT$/kWh
Ideal Operational Range (30%-70%)	0.627
Critical Operational Range (10%-30%, 70%-90%)	1.112
Warning Operational Range (0-10%, 90%-100%)	1.792

According to the operational cost coefficients in Table I, the operational cost of energy storage system C_{ESS} would be

$$C_{ESS} = \sum_{t=1}^{T} k_{ESS} P_{ESS}(t) \quad (5)$$

where k_{ESS} is the operational and maintenance cost coefficient and $P_{ESS}(t)$ is the output power of energy storage system at time t.

In this study, the hydrogen generator is applied. The operational cost of hydrogen fuel cell generator C_{FC} can be presented in (6), where k_{FC} is the operational and maintenance cost coefficient and $P_{FC}(t)$ is the output power of hydrogen fuel cell generator at time t.

$$C_{FC} = \sum_{t=1}^{T} k_{FC} P_{FC}(t) \quad (6)$$

Classification of the demand helps in the energy management and formulation of appropriate scheduling plans in microgrids, which impacts the quality of electricity consumption and equipment lifespan. This study assigns different levels of authorization to various types of loads, and when the electricity demand in the microgrid is high, an assessment is conducted through energy management calculations, and if necessary, load shedding decisions are implemented. However, implementing load shedding can affect the user, so the system needs to provide the economic compensation when load shedding is executed. Due to the high cost involved, the energy management strategy usually aims to prevent the occurrence of load shedding. The load-shedding cost of power interruption $C_{\text{int}}(t)$ at time t can be represented by (7).

$$C_{\text{int}}(t) = k_{\text{int}} P_{\text{int}}(t) \quad (7)$$

where k_{int} is the cost coefficient and $P_{\text{int}}(t)$ is the load-shedding power at time t.

As global sustainability becomes a priority, people are increasingly concerned about the environmental impact of energy generation and have proposed the concept of environmental cost (EC). The environmental cost refers to the cost of deteriorating environmental service quality caused by economic activities and is considered as an important indicator in modern microgrids. Some generators rely on fuel sources such as diesel, natural gas, and hydrogen, which result in emissions and air pollution. In this way, the environmental maintenance cost C_{EC} would be

$$C_{EC} = \sum_{i=1}^{m}\sum_{j=1}^{n} C_{ij} P_i(t) \quad (8)$$

where i and j are the numbers of DGs and pollution gases, C_{ij} is the treatment cost for j gas generated from i DG, and $P_i(t)$ is the output power of i DG at time t. In addition, the cost of utility grid C_{grid} can be given in

$$C_{grid}(t) = k_{grid} P_{grid}(t) \quad (9)$$

where k_{grid} is the real-time pricing and $P_{grid}(t)$ is the output power of utility grid at time t.

In this way, the cost function of optimal energy management for the microgrid would be represented in (10).

$$\min f(x) = C_{PV} + C_{FC} + C_{fuel} + C_{ESS} + C_{\text{int}} + C_{EC} + C_{grid} \quad (10)$$

In this paper, the PSO algorithm is applied to solve the optimization problem of (10) [9].

III. CASE STUDIES

To discuss the optimal energy management control strategy for microgrids, certain constraints and considerations of economy, environmental protection, and operability must be taken into account to achieve the lowest operating cost. This paper will use MATLAB simulation software for data analysis and instrument control, and understand the criteria for microgrid control theory and

practical construction as an important basis for evaluating and making decisions on optimized power dispatch. Firstly, this paper uses the actual data of the National Central University (NCU) microgrid as the analysis basis, and filters out the data that does not meet the research direction, such as signals generated by grid connection and discontinuous data. Then, this research would apply the obtained data to design algorithms and simulations, analyze various data such as solar power generation prediction and demand prediction, and calculate the optimal cost ratio of real-time power dispatch through algorithms.

The experimental demo site is depicted in Fig. 1, where the main source of power for the microgrid is 8-kW solar panels installed and a 21-kWh energy storage system to address the intermittent nature of solar energy. Besides, a 5-kW hydrogen generator is also connected to this microgrid for the power backup when the system is in the islanded mode.

Fig. 1. NCU microgrid.

The parameters for the LSTM neural network are listed in Table II. This study utilized the open-source neural network library Keras, written in Python, to construct the LSTMneural network model. The model architecture is a stacked LSTM, with a moving window serving as the input in the input layer. For prediction, only the previous 288 data points are used, resulting in 288 input units. The hidden layer consists of two layers, each with 50 neurons. The LSTM predicts the solar power generation for the next minute, and the output layer has a single unit. In the training parameters of the LSTM neural network, the number of epochs should not be excessively large to avoid issues such as gradient vanishing and overfitting. The loss function used is the Mean Absolute Error (MAE). Figure 2 illustrates the convergence process. The validation dataset used for testing consists of data from May 2022. The model was trained using the past five months of data to make consecutive seven-day predictions. The solar energy prediction for sunny days has an average error rate of 0.28, while the error rate is 0.37 for cloudy days. The lower accuracy in real-time predictions may be due to the short prediction time, leading to higher fluctuations. However, the total daily electricity generation remains very close to the actual values. The error rates fall within a certain acceptable range. Overall, the trend of electricity generation is similar, and this prediction model helps in planning future trends in energy management. The prediction result of solar power generation is depicted in Fig. 3.

TABLE II. PARAMETERS OF LSTM

Layer (type)	Output Shape	Param #
lstm (LSTM)	(None, 288, 50)	10800
lstm_1 (LSTM)	(None, 50)	20200
dense (Dense)	(None, 1)	51
Total params: 31,051, Trainable params: 31,051, Non-trainable params: 0		

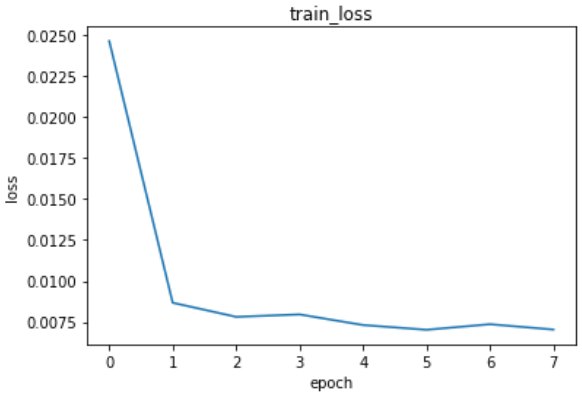

Fig. 2. Convergence process of LSTM for prediction of solar power generation.

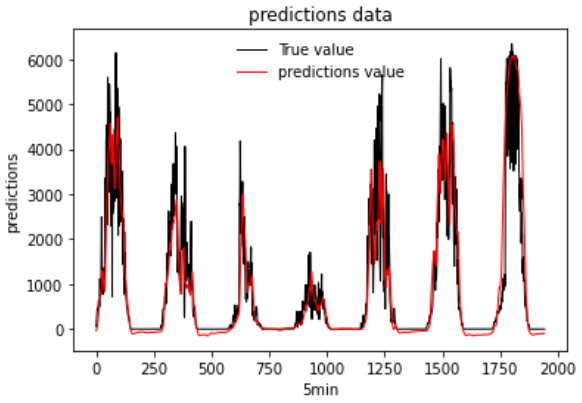

Fig. 3. Prediction result of solar power generation.

To realize the performance of proposed strategy, the commonly used rule-based method is compared [10]. The testing results are displayed in Figs. 4-5. Due to the excessive peak load, the energy storage system was charged to full capacity during off-peak hours as shown in Fig. 5. When the battery was charged according to the rule-based control with average electricity rates, the usage of grid electricity was surprisingly high, with instantaneous power exceeding 6 kW, as shown in Fig. 4(a). The cost of the optimized dispatch was 145 dollars, while the rule-based control cost 291 dollars. Moreover, it can be observed from the above scenario that the energy storage system managed by the optimization algorithm maintained a certain amount of electricity, while the rule-based control did not. The fuel cell and dynamic unloading were not triggered due to the high cost of affecting user experience and the environment.

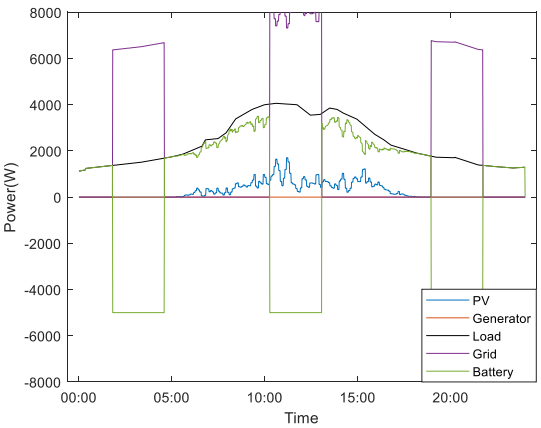

(a)

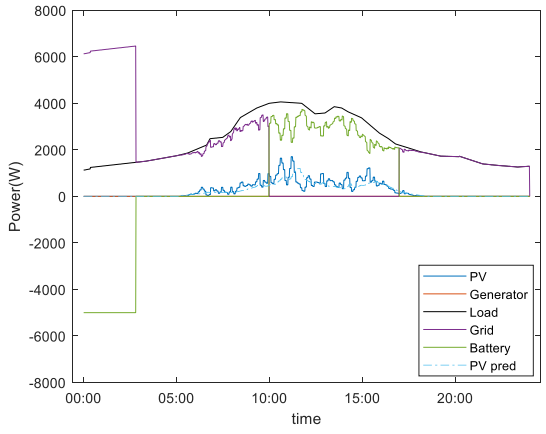

(b)

Fig. 4. Results of energy management with (a) rule-based method and (b) proposed method.

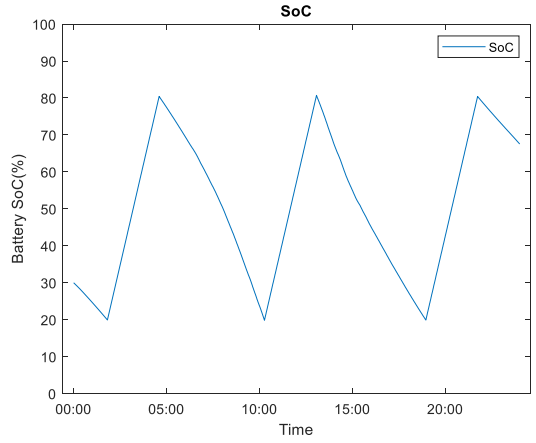

(a)

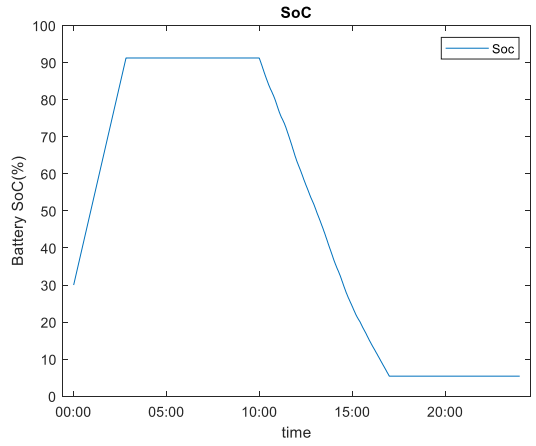

(b)

Fig. 5. State of charge for battery energy storage system with (a) rule-based method and (b) proposed method.

IV. Conclusion

Currently, most existing energy management systems control energy storage systems using rule-based approaches. In this study, to maximize the utilization of all available energy sources, a LSTM neural network is employed for solar energy prediction. This application can also be extended to predict other renewable energy sources, addressing the uncertainty associated with renewable energy and estimating the available energy for subsequent scheduling. A scheduling cost objective function is constructed, and the PSO algorithm is utilized to find the optimal solution as the control strategy for energy storage in microgrids. The objective function considers factors such as system lifespan, environmental considerations, cost optimization, and dynamic load-shedding, aiming to reduce peak power consumption and smooth out power demand, thereby enhancing the overall stability of the system. In addition, the integration and communication with currently available smart appliances in the market are considered to achieve true smart home and smart energy control in this study.

Acknowledgment

The authors would like to acknowledge the financial support from the Institute of Nuclear Energy Research of Taiwan through the Grant 112A015.

References

[1] Whitehouse Associates, “BP Statistical Review of World Energy 2021”, Centre for Energy Economics Research and Policy, Heriot-Watt University, ceerp.hw.ac.uk.

[2] S. M. Rizvi, A. Abu-Siada, N. Das, M. F. Ishraque and S. A. Shezan, "Active Power Sharing Method for Microgrids With Multiple Dispatchable Generation Units Using Modified FFC and IFC Mode Controller," *IEEE Access*, vol. 11, pp. 46229-46239, 2023.

[3] S. T. Cady, A. D. Domínguez-García and C. N. Hadjicostis, "A Distributed Generation Control Architecture for Islanded AC Microgrids," *IEEE Trans. on Control Systems Technology*, vol. 23, no. 5, pp. 1717-1735, Sept. 2015.

[4] A. Abbasi, H. A. Khalid, H. Rehman and A. U. Khan, "A Novel Dynamic Load Scheduling and Peak Shaving Control Scheme in Community Home Energy Management System Based Microgrids," *IEEE Access*, vol. 11, pp. 32508-32522, 2023.

[5] B. Zhang et al., "Event-Triggered Hierarchical Multi-Mode Management Strategy for Source-Load-Storage in Microgrids," *IEEE Trans. on Circuits and Systems I: Regular Papers*, vol. 70, no. 5, pp. 2201-2214, May 2023.

[6] Z. Zhao et al., "Distributed Robust Model Predictive Control-Based Energy Management Strategy for Islanded Multi-Microgrids Considering Uncertainty," *IEEE Trans. on Smart Grid*, vol. 13, no. 3, pp. 2107-2120, May 2022.

[7] M. Golam, R. Akter, J. -M. Lee and D. -S. Kim, "A Long Short-Term Memory-Based Solar Irradiance Prediction Scheme Using Meteorological Data," *IEEE Geoscience and Remote Sensing Letters*, vol. 19, pp. 1-5, 2022.

[8] Z, Liu, Y, Yi, J. Yang, W. Tang, Y. Zhang, X. Xie, T. Ji, “Optimal Planning and Operation of Dispatchable Active Power Resources for Islanded Multi-Microgrids under Decentralized Collaborative Dispatch Framework,” *IET Gener. Transm. Distrib.*, 2020, vol. 14 no. 3, pp. 408-422 .

[9] A. U. Rehman et al., "An Optimal Power Usage Scheduling in Smart Grid Integrated With Renewable Energy Sources for Energy Management," *IEEE Access*, vol. 9, pp. 84619-84638, 2021.

[10] C. Sun et al., "Design and Real-Time Implementation of a Centralized Microgrid Control System With Rule-Based Dispatch and Seamless Transition Function," *IEEE Trans. on Industry Applications*, vol. 56, no. 3, pp. 3168-3177, May-June 2020.

寄件者: IS3C 2023 <is3c2023@ncut.edu.tw>
寄件日期: 2023年5月5日星期五 下午 6:46
主旨: Notification - accept

Dear Prof. C. I Chen,

It is very pleased to inform you that your following paper has been accepted for presentation in IS3C2023.

Paper title:

#1156 Optimal Energy Management System Based on Particle Swarm Optimization for Microgrid

Please make a revision according to reviewers' comments if it is necessary when you submit your Final Paper.
Please also submit your final paper before May 12, 2023.

Presenting authors are required to register and pay fees before May 15, 2023 for early-bird discounts.
(Registration website: https://conference.iis.sinica.edu.tw/surl/eeEEe)

Each accepted paper requires one full registration and at least one author to present the paper in the conference.
Kindly remind you that without registration, your paper could not be submitted and will not be published in the conference proceedings.

Thank you very much for your cooperation and contribution.
We are looking forward to your participation in the upcoming IS3C2023 in Taichung, Taiwan.

Important information:
IS3C2023 web: http://is3c2023.ncuteecs.org/ Conference Date: June 30 - July 3, 2023 Registration Due: June 20, 2023 (Early-bird Discounts: Before May 15, 2023) Final Paper Submission Due: May 12, 2023

Sincerely yours,
IS3C 2023

=========

Click this URL to view comments:
https://conference.iis.sinica.edu.tw/surl/75958